A new high-brightness ion source
the atomic beam laser-cooled ion source

Notermans, R.P.M.J.W.

Award date:
2012

Eindhoven University of Technology
Department of Applied Physics
Coherence and Quantum Technology group (CQT)

A New High-Brightness Ion Source: the Atomic Beam Laser-cooled Ion Source

R.P.M.J.W. Notermans BSc.

Graduation project CQT 2012-03

Supervisor:
assist. prof. dr. ir. E.J.D. Vredenbregt

Abstract

In this report we discuss the properties of a new high-brightness ion source based on transverse cooling and compression of a thermal atomic rubidium beam using magneto-optical forces. The neutral atomic beam effuses from a Knudsen cell and, after cooling and compression, is photo-ionized to create a high brightness ion beam.

This new high-brightness ion source can be used for focused ion beam (FIB) applications where milling, imaging and deposition at the nanoscale needs to be done with increasing demands on control and resolution of the focused ion beam.

An analytical model of the high-brightness ion source is developed and simulations are performed to calculate the effects of transverse laser cooling and compression of the atomic beam. Disorder-induced stochastic heating of the ion beam immediately after ionization is also simulated.

From these simulations we conclude that this new source based on $^{87}Rb^{+}$ can reach a higher reduced brightness ($B_r = 2 \cdot 10^7$ A/m^2 srad eV) than conventional Liquid Metal Ion Sources (LMIS) by a factor of 20, whilst having an energy spread of 0.7 eV that is 6 times lower than the energy spread of the LMIS. The performance of the source is in the same league as the Gas Field Ionization Source (GFIS), but is a better alternative for milling at such high brightnesses as rubidium atoms have a much shorter penetration depth than the helium and neon atoms used in GFIS.

In the second part of this report we investigate the possibilities of stabilizing the frequency of a Titanium:Sapphire ring laser used for the magneto-optical cooling and compression of the atomic beam. Long-term frequency stabilization is achieved using a feedback system based on either modulation transfer (MT) spectroscopy or frequency modulation (FM) spectroscopy. The frequency stability is determined using the Allan variance, from which we find sub-20 kHz fluctuations over averaging times ranging from one second to a few thousand seconds, which is sufficient for future purposes.

We also investigate the possiblity of detuning the stabilized laser frequency using the Zeeman shift of the atomic reference frequencies. We conclude that this method is not accurate enough and propose future stabilization using MT spectroscopy and detuning the laser from the exact resonance frequency using two acousto-optical modulators.

"... en ik kan maar één ding zeggen:
hier voor mij zit de bloem der natie."

Prof. dr. ir. Klaas Kopinga
Addressing the first year students
September 2006

Contents

Chapter 1

Introduction

Since the advent of the microprocessor industry, miniturization has become one of the main goals of the industry to produce faster devices with the capability to perform complex tasks. In the near future, however, a company's adherence to the well-known Moore's law of miniturization will not provide sufficient competition as microprocessors will reach limits in either the realization of the miniturized devices or energy consumption [1]. On a different development track, 3D microprocessors will become a complex but interesting alternative [2]. The production of complex 3D structures or improving the product reliability and custumization of current designs will become more important [2, 3]. To achieve these goals, the industry will require the ability to probe and modify nanostructures with evermore increasing control and spatial resolution.

Conventional (optical) microscopy does not provide the full answer as the resolution is diffraction limited by the wavelength of light used. Using shorter wavelengths (e.g. x-ray microscopy) does improve the resolution, but most materials are transparent for such high photon energies. A next step can be achieved by considering alternatives to optical microscopy. Particles such as electrons and ions have much shorter (De Broglie) wavelengths than photons, and thus have a much lower diffraction limit. As they are charged particles they can easily be manipulated using electric and magnetic lenses, although interparticle Coulomb interactions provide another realm of problems and difficulties to overcome [4].

A scanning electron microscope (SEM) is an important tool to probe microscopic surfaces and objects. A SEM uses a focused electron beam to scan the surface of a sample. By detecting the scattered electrons or the secondary electrons emitted by the surface, topological and information about the chemical composition can be obtained. Although the SEM has excellent probing characteristics, it is difficult to use SEM to sputter a surface in order to obtain information about sub-surface chemical composition of the sample or to purposely modify the structure [5].

Ions, however, have a much higher mass than electrons and are therefore much more suitable for milling[1] as they provide more 'punch' when striking a surface. Due to their size, ions do not penetrate the sample as deeply as electrons or photons. This makes secondary ion mass spectroscopy (SIMS) an excellent method to obtain chemical information of the surface. Further, as ions have a low penetration depth, they can also be used to deposit materials on the surface [6].

[1] Milling is a common phrase which includes the sputtering and redeposition of material on a substrate.

Combining these characteristics (milling, imaging and deposition), ions are an excellent candidate to constitute a main tool in nanodevice industry [7].

1.1 Focused ion beams (FIBs)

In order to use ions as a tool for working with nanostructures, ion beams need to be created which can be focused down to nanometer spotsizes. In order to discuss and compare different ion beam sources, we first discuss two figures of merit used to describe the quality of ion beams.

1.1.1 Figures of merit

There are two common figures of merit used to assess the focusability and current of a charged particle beam. The first figure of merit is the longitudinal energy spread σ_U of the ions in the beam, where σ_U is defined as

$$\sigma_U = \frac{1}{2}m(\langle v^2\rangle - \langle v\rangle^2). \tag{1.1}$$

A large σ_U indicates that the ion beam is sensitive to chromatic aberrations when focusing.

The second figure of merit is the transverse reduced brightness B_r. In units of A / m^2 sr eV, the reduced brightness of a beam with a Gaussian distributed phase-space density is defined as [8]

$$B_r = \frac{2I}{4\pi^2 mc^2 \varepsilon_x \varepsilon_y}, \tag{1.2}$$

where I is the current and ε_x and ε_y the normalised root-mean-square (rms) emittance of the beam in the transverse x and y direction (here, by convention, the beam propagates along the z-axis). The reduced brightness is independent of the beam energy for nonrelativistic beams [8]. The normalised rms emittance along transverse axis i is defined as

$$\varepsilon_i = \frac{1}{mc}\sqrt{\langle i^2\rangle\langle v_i^2\rangle - \langle i v_i\rangle^2}. \tag{1.3}$$

Using this definition of emittance, the reduced brightness can be written as

$$B_r = \frac{I}{4\pi^2 \varepsilon_r}, \tag{1.4}$$

where ε_r is the reduced emittance of the beam defined as

$$\varepsilon_r = \frac{m}{2}\sqrt{\langle x^2\rangle\langle v_x^2\rangle - \langle x v_x\rangle^2}\sqrt{\langle y^2\rangle\langle v_y^2\rangle - \langle y v_y\rangle^2}. \tag{1.5}$$

The notation $\langle . \rangle$ represents an average over a set of particles of the beam. Ion beams do not necessarily have a homogeneous reduced brightness; the central (on-axis) part of the beam usually has a higher reduced brightness than the 'wings' (off-axis part) of the beam. In practice the reduced brightness can be increased by aperturing the beam, but at a cost of a lower current. The maximum reduced brightness attainable by a tightly apertured beam is also called the 'peak brightness', and this is the brightness generally discussed in this report. If any other definition of brightness is used, this will be mentioned explicitly.

The peak brightness can be calculated analytically, but it is difficult to calculate the peak brightness in simulations as the number of particles contributing to the peak brightness is much smaller than the total number of particles used in the simulations. If only a few particles contribute to the peak brightness, the statistical fluctuations of the calculated peak brightness are very large. Therefore we define a 10% reduced peak brightness (also denoted as B_r^p) which includes 10% of the total number of particles that are closest to the propagation axis and thus contribute most to the peak brightness. The validity of this method will be discussed in Section 3.5

Finally, if we obtain an ion beam and a focusing system without any spherical abberations, the final chromatic abberation limited 50% (full width median) spot size σ_s of a focused ion beam with a specified current can be calculated as [9]

$$\sigma_s = \left(\frac{I C_c^2 \sigma_U^2}{B_r V_p^3} \right)^{1/4}, \tag{1.6}$$

where C_c is the chromatic aberration coefficient of the focusing system and V_p the applied electric field used to accelerate the ion beam. Typically $C_c = 20$ mm and $V_p = 30$ kV in FIB columns [10]. Here we are interested in maximizing the reduced brightness of the beam whilst maintaining a high current. A high current increases the spotsize, but is necessary to obtain measurable signals.

1.1.2 Common ion sources

The current state of the art high brightness ion source for FIB applications is the Liquid Metal Ion Source (LMIS). The LMIS is based on a needle tip which is connected to a liquid metal (usually gallium) reservoir [11, 12]. By applying an electric field, the liquid metal forms a small cone-shaped droplet at the tip at which the atoms are extracted from the liquid and ionized due to field ionization. The resulting ion beam can then be used in a typical FIB system, as shown in Figure 1.1. LMIS can provide brightnesses of $B_r = 10^6$ A/m^2 sr eV at a current of 1 pA, with an energy spread of $\sigma_U = 4.5$ eV, and can go to currents on the order of μA [11]. Although the brightness is quite high, the large energy spread of the LMIS limits the attainable spotsize due to chromatic aberrations. Further, there are not many alternative elements to be used than gallium, which has the most favourable combination of high surface tension and low vapor pressure required for efficient extraction of ions [13].

An alternative would be the Gas Field Ionization Source (GFIS) [14]. Contrary to the LMIS, where the liquid metal wets the tip, the GFIS is based on ionization of a gas near the tip. An applied electric field will ionize the gas atoms near the tip due to quantum mechanical electron tunneling, after which the ions are accelerated away from the tip. Current GFIS uses helium or neon, with which brightnesses of $B_r \approx 5 \cdot 10^8$ A/m^2 sr eV with an energy spread of $\sigma_U \approx 0.5$ eV can be obtained [14]. The imaging resolution with such brightness and energy spread is much higher than the LMIS, but the large penetration depth of such light elements as helium and neon makes them useless for milling purposes. To improve the milling capacity of the GFIS, research on argon and xenon based sources is currently being done [15].

The high brightness which can be achieved by both the LMIS and GFIS is based on the fact that the extraction volume, from which the ions are created, is approximately as small as the final

attainable spotsize of the FIB. Although the initial ionization volume is very small, the divergence of the ion beam is huge. Hence an alternative source could be considered which might have a larger ionization volume, but a much lower divergence of the ion beam. This idea is the basis of laser-cooled ion sources.

1.1.3 Laser-cooled ion sources

Laser-cooled ion sources, such as the rubidium Ultra Cold Ion Source (UCIS) at the TU/e, have a huge advantage compared to the LMIS and GFIS: essentially any element which can be laser-cooled, can be used to create an ion beam. The UCIS is based on the magneto-optical cooling and trapping of neutral atoms in a magneto-optical trap (MOT) [16], after which they are ionized using an ionization laser beam. The ions are extracted using an applied electric field. As the ions are created from laser-cooled atoms, the transverse velocities (and therefore the divergence of the beam) are much smaller than for the LMIS or GFIS [17]. The UCIS used at the Coherence and Quantum Technology (CQT) group could produce brightnesses of $B_r = 3 \cdot 10^5$ A/m^2 sr eV at a current of 1 pA [17]. Although this brightness is lower than the brightness achieved by LMIS or GFIS, it is compensated by a extremely low energy spread of the ions (up to 0.02 eV) [17]. However, these numbers are the theoretical capability of the UCIS, as an important limit on the current is the loading rate of the MOT, for which solutions such as the push-beam method should be applied [18]. The brightness and energy spread of the UCIS which have been achieved are given in Table 1.1.

The basic limitation of the UCIS is the fact a MOT is limited by its loading rate; it is impossible to extract more ions from the MOT than there are atoms diffusing into the MOT. Even if one were to increase the density of the MOT to extract higher currents, increased collision rates will deteriorate the brightness of the MOT [18]. Therefore we propose a new ion source, the Atomic Beam Laser-cooled Ion Source (ABLIS), as proposed by Mutsaers *et al* [19]. In stead of a MOT, we use a Knudsen cell to form a neutral atomic beam which we transversally cool and compress using the same magneto-optical forces used in a MOT. As we only apply these forces in the transverse direction, we call this a 2D-MOT or a MOC (magneto-optical compressor). After cooling and compression in the 2D-MOT, we get a neutral atomic beam with a very high phase-space density. The neutral atomic beam is then ionized using an ionization laser beam. We will present an analytical model and simulations on the performance of the ABLIS in this report, and a preliminary comparison between the four ion sources is shown in Table 1.1

Table 1.1: *A comparison of the different types of ion sources used for FIB applications. In order to make this comparison, we use an ion current of 1 pA for all sources, although some sources can produce currents which are orders of magnitude larger. All numbers are derived from experimental results except for the ABLIS, for which currently only simulation results are available.* **The spot size is calculated using Equation. 1.6, using the coefficient values given in the text.* †*These elements are currently being researched [15].*

Source property [unit]	LMIS [11, 12]	GFIS [14]	UCIS [17, 18]	ABLIS
Used element	^{69}Ga	^{4}He	^{85}Rb	^{87}Rb
Alternative elements	Limited	Ne, Xe†, Ar†	Over 20	Over 20
Energy spread [eV]	4.5	< 0.1	0.9	0.7
Reduced Brightness [A / m^2 sr eV]	10^6	$5 \cdot 10^8$	$2 \cdot 10^3$	$2 \cdot 10^7$
Spot diameter* [nm]	3	0.3	9	0.5

1.2 This report

In the first part of this report, we develop an analytical model of the ABLIS. From this analytical model certain experimental parameters, such as the optimal laser detuning, magnetic field gradient and source temperature, can be determined. As the analytical model is limited by considering the atom-laser interactions according to the ideal 2-level atom model, simulations are performed which take the actual rubidium hyperfine magnetic sub-structure and spontaneous emission into account. We will look into the performance limits and optimize the technical parameters of the 2D-MOT required to cool and compress the neutral atomic beam.

In the second part of this report experimental work is discussed on the frequency stabilization of a Titanium:Sapphire ring laser system, as this laser system will be used in the future to create the 2D-MOT. The frequency stabilization is based on saturated absorption techniques such as frequency modulation (FM) spectroscopy and modulation transfer (MT) spectroscopy, using a rubidium gas cell as a reference. Starting with a discussion on the feedback system built in the lab, we characterize the feedback system sensitivities to polarization and magnetic fields. We then explore the possibilities of detuning the locked laser frequency using the Zeeman shift to shift the atomic reference transition frequency. Finally the stability of the laser system is determined in terms of Allan deviation and linewidth by locking the laser frequency to the required rubidium transition and creating a beatnote with a laser from the UCIS setup which is locked to the same transition.

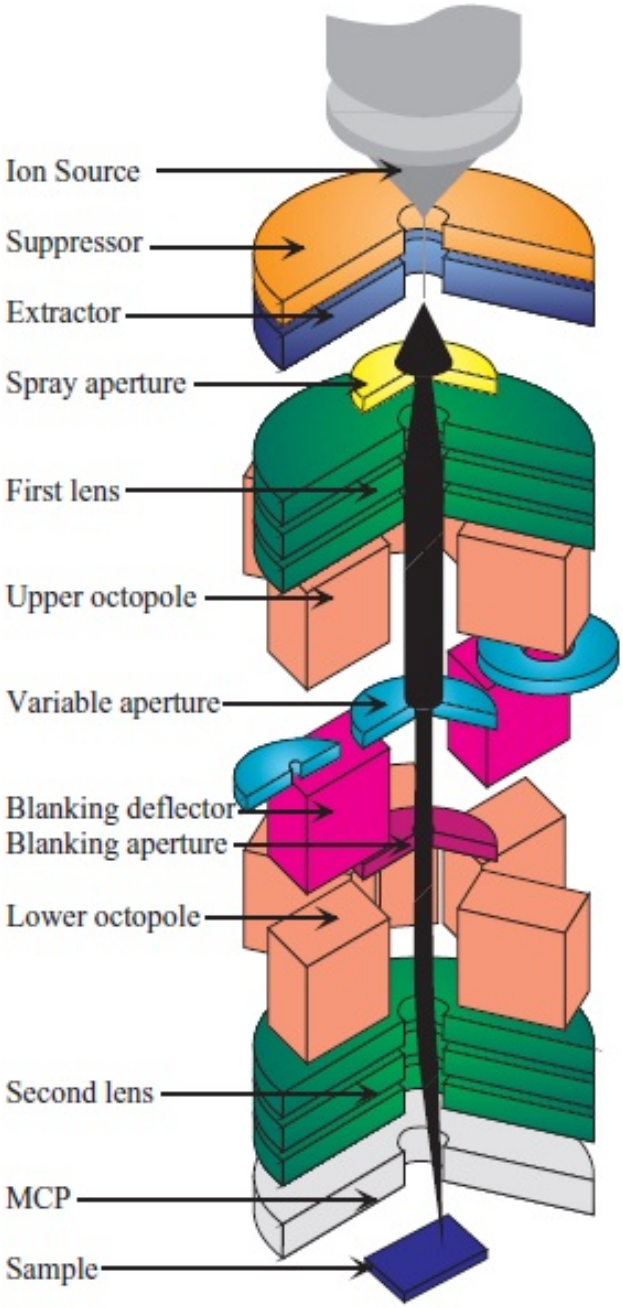

Figure 1.1: *Schematic view of a focused ion beam (FIB) system. Once the ion beam is created, a first lens is used to collimate the beam. Then an octopole lens is used to reduce the spherical aberrations. The variable aperture at the center is used to vary the total current and brightness of the resulting ion beam, to vary between e.g. high resolution SIMS or high current milling. The lower octopole lens is used to steer the ion beam, which is focused by the second lens. Finally, the MCP can detected secondary particles to reconstruct an image of the sample surface. This Figure has been adopted from [7].*

Chapter 2

Atomic Beam Laser-cooled Ion Source

Based on the idea proposed by Freinkman *et al* [20] and extended by Mutsaers *et al* [19], the ABLIS is a thermal atomic beam which is transversally cooled and compressed using magneto-optical forces, after which it is ionized using near-threshold ionization. Additionaly, as a techical requirement the ABLIS should be as compact as possible to make it easy to implement in existing FIB instruments. Further, most optical paths should be in optical fibers, for a more flexible and decoupled optical setup.

The atomic species used in this experiment is rubidium as it is a common element used to produce ultracold gases through laser cooling [16]. Further, rubidium is already being used in the current UCIS setup hence there is quite some practical knowledge available in the research group. An advantage of using rubidium is the low melting point at 312.5 K, which is only slightly above room temperature [21]. As considerable vapour pressures create considerable particle fluxes which are required to produce large ion beam currents, these can be achieved using rubidium without having to heat it to extreme temperatures. All other relevant data on the rubidium atom is given in Table 2.1.

The atomic beam will be produced using a Knudsen cell. A Knudsen cell is essentially a container with a thin-walled orifice [24]. As the diameter of the orifice is much smaller than the mean free path Λ of the particles, the particles do not collide with each other and the expanding gaseous beam outside the Knudsen cell can be considered to be in the same thermal equilibrium as the gas inside the Knudsen cell. The effusion of particles through the orifice, effusion rate, angular distribution and velocity distribution can be calculated using the kinetic gas theory applicable to the gas inside the Knudsen cell.

The basic setup of the ABLIS is shown in Figure 2.1. The atomic beam effusing from the Knudsen cell enters a light field consisting of counterpropagating laser beams (with σ^+ and σ^- polarization, respectively) perpendicular to the propagation direction of the atomic beam. Figure 2.1 only shows the setup in the $x-z$ plane, where the beam propagates along the $z-$axis and x is the transverse coordinate. It should be noted that there is another set of counterpropagating

Table 2.1: *Atomic constants of rubidium used in the calculations and simulations. Unless stated otherwise, the data is from [21]. The values of p_0 and T_0 used to calculate the vapour pressure in the Knudsen cell are valid for source temperatures ranging from 312 K (rubidium melting point) to 550 K [21]. †The cooling transitions are $5^2S_{1/2}$ $(F = 3) \rightarrow 5^2P_{3/2}$ $(F = 4)$ for ^{85}Rb and $5^2S_{1/2}$ $(F = 2) \rightarrow 5^2P_{3/2}$ $(F = 3)$ for ^{87}Rb [16]. *The cooling transition wavelengths are calculated from [22, 23]. The frequency difference between the cooling transitions of the two rubidium isotopes is* 1204.6 *MHz.*

Parameter [unit]	Symbol	^{85}Rb	^{87}Rb
Mass [amu]	m	84.91	86.91
Natural abundance [%]	-	72.2	27.8
Pressure constant [Pa]	p_0	$2.08 \cdot 10^9$	$2.08 \cdot 10^9$
Temperature constant [K]	T_0	$9.30 \cdot 10^3$	$9.30 \cdot 10^3$
Cooling transition wavelength†* [nm] [16]	λ	780.2437	780.2462
Natural linewidth [rad/s] [16]	γ	$2\pi \cdot 5.98$ MHz	$2\pi \cdot 5.98$ MHz
Saturation intensity [W/m^2] [16]	I_s	16.4	16.4
Doppler limit ($s_0 \rightarrow 0$) [μK]	T_D	143.41	143.41
Ionization wavelength of the $5^2P_{3/2}$ state [nm] [16]	λ_I	480	480
Nuclear spin [quantum number]	I	5/2	3/2

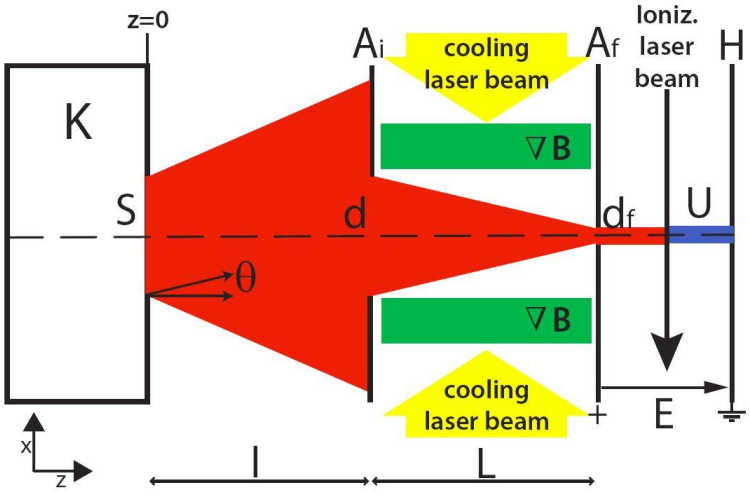

Figure 2.1: *Schematic view of the ion source. An effusive Knudsen cell K with orifice surface S produces a particle flux which is apertured by an aperture with radius d at a distance l from the cell. An applied magnetic field gradient ∇B and a light field (two counter-propagating laser beams with σ^+ and σ^- polarization, respectively) cool and compress the particle beam. There are two pairs of laser beams, in the $x - z$ and in the $y - z$ plane. The cooled and compressed atomic beam is apertured by an aperture with radius d_f after a distance L from the first aperture. Then the beam is ionized and accelerated in the electric field E for FIB purposes.*

laser beams in the $y-z$ plane, where y is the transverse coordinate orthogonal to x. In this way the beam experiences magneto-optical cooling and compression forces along both transverse coordinates. The origin of these magneto-optical forces will be explained in the next Section. Additionaly we require a magnetic field gradient in order to create a magneto-optical compression force. In our analytical model, which will be presented later, we assume this magnetic field gradient is radially symmetric, i.e., we apply radial compression. However, such magnetic fields have $\nabla \cdot \vec{B} \neq 0$ and can therefore not be realized[1]. The best alternative is a quadrupole magnetic field, which enables us to compress the beam along both the $x-$ and $y-$axes.

The beam is apertured before it enters the light field, as the capture range of the magneto-optical compressor is limited: the part of the beam which is too divergent (i.e. is too far from the $z-$axis or has too large transverse velocities) will not be cooled and compressed effectively within the finite length L. After the magneto-optical cooling and compression, the beam is apertured again. This second aperture is used to only select the central part of the beam, which will give the highest (peak) brightness. In the third section, after the second aperture, a laser ionizes the atomic beam while an applied electric field accelerates the resulting ion beam. The resulting ion beam can be focused to a small spotsize using ion optics used in FIB systems.

In this Chapter we first introduce magneto-optical forces: where they originate from and how they can be used to cool and compress an atomic beam. After having discussed these forces, we present an analytical model of the ABLIS in order to calculate the performance and to calculate for which experimental parameters this performance can be optimized.

2.1 Interactions between atoms and radiation

Before we can discuss the performance of the ABLIS, we need to introduce the magneto-optical forces which are used in the ABLIS to cool and compress the atomic beam. First we briefly discuss the electron level structure of atoms, after which the relevant magneto-optical forces are discussed.

2.1.1 Electron level structure in atoms

The interaction between atoms and radiation usually takes place when the frequency of the radiation is near the frequency corresponding to an electronic transition in the atom. In the calculations presented in this project we will use a simplified version of the atom: a 2-level atom which only has a single electronic transition with a single frequency. However, in reality the possible energy levels of an atom are much more complicated. In the standard spectroscopic notation, each energy level can be written as $n^{2S+1}L_J\ F$. We will discuss all the different parameters present in this notation. Here a brief overview is given, a more extensive explanation can be found in [25, 26].

The principal quantum number n represents the semiclassical 'orbit' of an electron around the nucleus. The lowest possible value of n is 1. With n there are a finite possible number of angular momentum states associated with the electrons in the state n. These angular momentum states

[1] An example would be the field $\vec{B}(r) = \alpha r\vec{e}_r$, with $B(r) = |\vec{B}(r)| = \alpha r$ and α the gradient. But $\nabla \cdot \vec{B} = 2\alpha \neq 0$. An alternative would be the quadrupole magnetic field $\vec{B}(x,y) = \alpha(x\vec{e}_x - y\vec{e}_y)$, for which $B(x,y) = |\vec{B}(x,y)| = \alpha\sqrt{x^2+y^2} = B(r)$, $\nabla B = \alpha\vec{e}_r$ and $\nabla \cdot \vec{B} = 0$.

are labeled with the quantum number L. The value of L can range from $-n+1$ to $n-1$ in integer values. Additionally the atomic state is also labeled with the quantum number S, which represents the total spin of the electrons.

In the LS-coupling scheme, where the angular momentum of the electrons combines with the spin, the resulting total electronic angular momentum state is labeled with quantum number J. The possible combinations of L and S which form J ranges from $|L-S|$ to $|L+S|$ in integer values. In the spectroscopic notation, the $2S+1$ term represents the number of possible values of J a single combination of L and S can generate. These states constitute the fine structure of the atom.

In the LS-coupling scheme the interactions of the electrons with the nuclear spin I of the atom are ignored. If we include the interaction between the total electronic angular momentum and the nuclear spin (with quantum number I) in the IJ-coupling scheme, a total angular momentum quantum number F can be constructed from J and I and the possible values of F ranges from $|I-J|$ to $|I+J|$. This is called the hyperfine structure.

The combination of all these quantum numbers leads to the spectroscopic state description $n^{2S+1}L_J\ F$. Knowledge of the nuclear spin I then makes it possible to describe the state using only the quantum numbers I, J, F and the projection of F along a quantization axis M_F. The quantization number M_F is also called the magnetic quantum number, as it is coupled to the total magnetic moment of the atom.

In this work we will discuss transitions from the $5^2S_{1/2}\ F$ states to the $5^2P_{3/2}\ F'$ states for ^{85}Rb and ^{87}Rb. Figure 2.2 shows these two states and their hyperfine structure for ^{85}Rb, which has a nuclear spin quantum number of $I = 5/2$ (see Table 2.1). A more detailed level scheme for both isotopes is shown in Appendix B as Figures B.1 and B.2.

It is clear that this is not a simple level structure to work with. In order to be able to perform calculations in the analytical model, we make certain simplifications as discussed in Section 2.1.3.

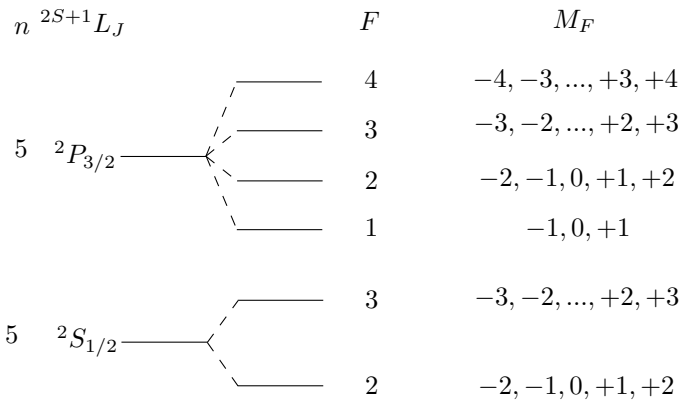

Figure 2.2: *Schematic hyperfine levels for the $5^2S_{1/2}$ and $5^2P_{3/2}$ states of ^{85}Rb. As this rubidium isotope has a nuclear spin of $I = 5/2$, the electronic angular momentum J couples to the nuclear spin I to form the total angular momentum state F. Finally, the allowed magnetic substates M_F per F state are shown.*

Transition rules

Electronic transitions between different states can only occur for certain properties of the initial and final state. These restrictions are caused by quantummechanical constraints, such as the requirement that electric dipole transitions cannot change the electron spin hence the term S cannot change during a transition: $\Delta S = 0$. Further, a photon carries an angular momentum quantum number of 1. Due to conservation of angular momentum, the total angular momentum of an atom after absorbing a photon cannot change by more than 1. Therefore another transition rule is $\Delta F = 0, \pm 1$. However, the transition $F = 0 \rightarrow F' = 0$ is not allowed as this would violate conservation of angular momentum. From the conservation of angular momentum one can also derive identical transition rules for L and J.

We also mentioned the magnetic quantum numbers M_F associated with the hyperfine state F. There are additional transition rules for M_F based on the polarization of light. For linearly polarized light, only $M_F \rightarrow M_{F'}$ can occur for which $\Delta M_F = 0$. However, for circularly polarized light only $\Delta M_F = +1$ or $\Delta M_F = -1$ transitions can occur for σ^+ or σ^- polarizations, respectively.

Zeeman shift

The atom has a magnetic moment depending on the electronic state and the nuclear spin. In an applied field $\vec{B}$, the projection of the total angular momentum along $\vec{B}$ leads to an additional magnetic energy

$$\Delta E = g_F \mu_B B M_F, \tag{2.1}$$

where g_F is the Landé factor of the state[2], μ_B is the Bohr magneton and M_F is the quantum number related to the projection of the total angular momentum on $\vec{B}$. Hence depending on the M_F state, an electronic state can experience a shift in energy due to an applied magnetic field. This shift is called the Zeeman shift. A change in the energy of an electronic state can be measured as the frequency of a transition from or to this state also changes. We will use this effect later to apply a force on the atoms.

2.1.2 Magneto-optical forces

The interaction of atoms with radiation is described extensively in literature, and for a full treatment of these interactions we refer to [16, 25, 26]. One of the results of describing these interactions is the quantification of forces acting on atoms. The origin of this force is based on the scattering of photons by an atom. An atom in an excited state can decay to the ground state by emitting a photon in a random direction. Although photons have a momentum $\hbar k$, where $k = 2\pi/\lambda$ is the wavenumber of the photon and $\hbar$ Planck's constant divided by 2π, the absorption and emission of photons in random directions does not produce a net force. However, if an atom absorbs photons from a specific direction but still emits the photons in random directions, there will be a net force acting on the atom. As this force is based on the scattering of photons, it is called the scattering force.

[2]The Landé factors relevant for our work are shown in Table B.1 in Appendix B.

For an atom for which we only consider a ground and an excited state, also called an ideal 2-level atom, the scattering rate can be calculated using the optical Bloch equations [25]. The scattering force F_{scatt} is then the scattering rate R_{scatt} (the number of photons emitted per second) multiplied by the momentum kick $\hbar k$ per scattered photon [25]

$$R_{scatt} = \frac{\gamma}{2}\frac{s_0}{1 + s_0 + (2\delta/\gamma)^2}, \tag{2.2}$$

$$F_{scatt}(\delta) = \hbar k\frac{\gamma}{2}\frac{s_0}{1 + s_0 + (2\delta/\gamma)^2}, \tag{2.3}$$

where γ is the linewidth of the transition, $\delta = \omega_L - \omega_0$ the detuning of the laser frequency ω_L to the transition frequency ω_0 and $s_0 = I/I_s$ is the saturation parameter which is the ratio of the light intensity I and the saturation intensity I_s of the transition. An excited state of the atom always has a finite lifetime $\tau = 1/\gamma$, so the energy of the excited state has a finite width which is expressed as a width in the frequency distribution of the photons that are absorbed. This frequency distribution is Lorentzian, and the full width at half the maximum (FWHM) of the frequency distribution is defined as the linewidth γ of the transition. The linewidth and saturation intensity are given in Table 2.1.

Optical molasses

In our definition of the scattering force, we have implicitly assumed that the atom is not moving. However, if the atom does move, the frequency of the photons as observed by the atom shift due to the Doppler effect given by $-\vec{k}\cdot\vec{v}$ [16]. The frequency becomes velocity-dependent

$$F_{scatt}(\delta - kv) = \hbar k\frac{\gamma}{2}\frac{s_0}{1 + s_0 + (2(\delta - kv)/\gamma)^2}, \tag{2.4}$$

where we have assumed that the atom moves collinear with the laser beam and $-\vec{k}\cdot\vec{v} = -kv$.

Now consider two counterpropagating laser beams. The Doppler shift of the atom with respect to either laser beam is $\pm\vec{k}\cdot\vec{v}$. The net force acting of both beams acting on the atom is

$$F_{tot} = F_{scatt}(\delta - kv) - F_{scatt}(\delta + kv), \tag{2.5}$$

$$F_{tot}(v) = \hbar k\frac{\gamma}{2}\frac{s_0}{1 + s_0 + (2(\delta - kv)/\gamma)^2} - \hbar k\frac{\gamma}{2}\frac{s_0}{1 + s_0 + (2(\delta + kv)/\gamma)^2}. \tag{2.6}$$

The total force is shown in Figure 2.3. The maxima of the force occur near the capture velocity $\pm v_c$, which is defined as $v_c = |\delta/k|$. The force within this velocity range is proportional to v and can be considered as a damping force, acting like a viscous fluid. For small velocities,

$$F_{tot}(v) \approx -2kv\frac{\partial F_{scatt}}{\partial\omega_L}, \tag{2.7}$$

$$F_{tot}(v) \approx -\alpha v = 8\hbar k^2\frac{s_0(\delta/\gamma)}{\left(1 + s_0 + (2\delta/\gamma)^2\right)^2}v. \tag{2.8}$$

As $\alpha > 0$ for damping, we find that $\delta < 0$, i.e. the laser frequency should always be detuned below the transition frequency for damping.

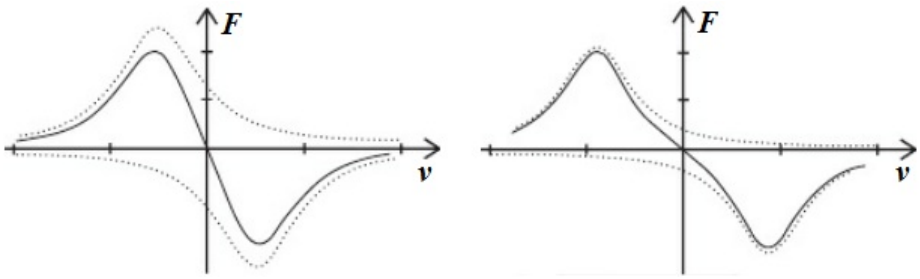

Figure 2.3: *One dimensional optical scattering force for two counterpropating beams. The full line is the total force, the dotted lines are the individual contributions.* ***Left*** *The laser frequency is detuned $\delta = -\gamma/2$ from the transition frequency.* ***Right*** *The laser frequency is detuned $\delta = -\gamma$ from the transition frequency. For small velocities v the total force is proportional to v.*

Cooling limit

Now we have a damping force, we can investigate the limit to which the atoms can be cooled. The temperature of the atoms is defined as

$$k_B T = \frac{1}{2} m(\langle v_i^2 \rangle - \langle v_i \rangle^2), \tag{2.9}$$

where m is the atomic mass, $i = x, y, z$ and k_B is Boltzmann's constant. Here we see that the width of the velocity distribution of the atoms defines the temperature. Hence cooling an ensemble of atoms actually means that the width of the velocity distribution is reduced. However, in this simple picture atoms can be cooled to 0 K because we have neglected any possible heating processes when scattering photons. In the velocity phase-space of a single atom, the scattering of photons changes the velocity of the atom in steps of $v_r = \hbar k/m$ (the recoil velocity, which represents the change in velocity from a single photon 'kick'). As the direction in which the photon is emitted is random, so is the velocity change. As an atom scatters $t \cdot R_{scatt}$ photons during time t, the mean square of the velocity increases as [25]

$$\langle v_i^2 \rangle_{spontaneous} = \eta v_r^2 R_{scatt} t, \tag{2.10}$$

where the factor $\eta = 1/3$ represents the angular average for isotropic emission. However, the atom does not exactly scatter $R_{scatt}t$ photons during an interval t. Assuming the scattering follows Poissonian statistics, the root mean square of the velocity increases as [25]

$$\langle v_i^2 \rangle_{absorption} = v_r^2 R_{scatt} t. \tag{2.11}$$

Here the isotropic emission does not play a role as we consider the absorption of photons from a single direction.

Combining these two heating mechanism with the cooling mechanism, the average kinetic energy of the atoms changes as

$$\frac{1}{2} m \frac{d\langle v_i^2 \rangle}{dt} = (1 + 2\eta) E_r (2R_{scatt}) - \alpha \langle v_i^2 \rangle, \tag{2.12}$$

where $E_r = (1/2)mv_r^2$ is the recoil energy. We use $2R_{scatt}$ as there two laser beams and therefore the scattering rate doubles. The factor 2η takes into account that cooling in two dimensions

(two pairs of counterpropagating laser beams, such as in our 2D-MOT) increases the number of spontaneous emissions[3]. The minimum root mean square velocity is determined by setting $d\langle v_i^2\rangle/dt = 0$. Filling in $\eta = 1/3$ and α from Equation 2.8 and using our definition of temperature as stated before we find a transverse temperature for two-dimensional cooling

$$k_B T^{2D} = -\frac{5}{6}\frac{\hbar}{4}\Big(\frac{\gamma^2}{2\delta}(1+s_0)+2\delta\Big). \tag{2.13}$$

For three-dimensional cooling, where there are three counterpropagating beams, is [25]

$$k_B T^{3D} = -\frac{\hbar}{4}\Big(\frac{\gamma^2}{2\delta}(1+s_0)+2\delta\Big). \tag{2.14}$$

Hence we see that the final temperature achievable with two-dimensional cooling is 5/6 ($\approx 83\%$) of the final temperature achievable with three-dimensional cooling.

Both final temperatures are minimized for $\delta = -\gamma/2\sqrt{1+s_0}$. This minimal achievable temperature is called the Doppler temperature T_D and is usually given for cooling in three dimensions as

$$k_B T_D = \frac{\hbar\gamma}{2}\sqrt{1+s_0}. \tag{2.15}$$

For the two-dimensional cooling, this result should be multiplied by 5/6. This limit is called the Doppler limit as it is achieved using a cooling technique based on the Doppler shift.

2.1.3 Compression forces

We have seen how the scattering force can be used to reduce the velocity of atoms due to a velocity-dependent effect (the Doppler effect). One way to produce a space-dependent force is by using the Zeeman effect (see Section 2.1.1). If we apply a linearly varying magnetic field B with gradient ∇B, the magnitude can be written as $B(x) = \nabla B x$. The energy shift as function of position is

$$\Delta E(x) = g_F \mu_B \Big(\nabla B\Big) M_F x. \tag{2.16}$$

However, this sign of the shift depends on the sign of M_F. For an excited $F = 1$ state, the possible values for M_F are $M_F = -1, 0, +1$. This means that the states $M_F = -1$ and $M_F = +1$ experience opposite energy shifts depending on their position in the magnetic field; the $M_F = 0$ state will not experience any shift. This example is also shown in Figure 2.4. This model with a $F = 0$, which has only $M_F = 0$, ground state and a $F = 1$ excited state is the ideal 2-level model that will be used during the calculation of the analytical model.

A laser beam with frequency ω_L, which is slightly detuned by an amount δ from the actual transition frequency, propagates from both the left and right hand side. However, both beams have opposing circular polarizations. The $M_F = -1$ state shifts to lower energies as the atoms are more to the right. At some position the energy shift is large enough to have detuned the transition frequency to be in resonance with the laser frequency. However, as the excited state is in the $M_F = -1$ state, a transition from the ground $M_F = 0$ state can only be induced by σ^-

[3]The substitution 3η is made when calculating the heating for a 3D-MOT [25].

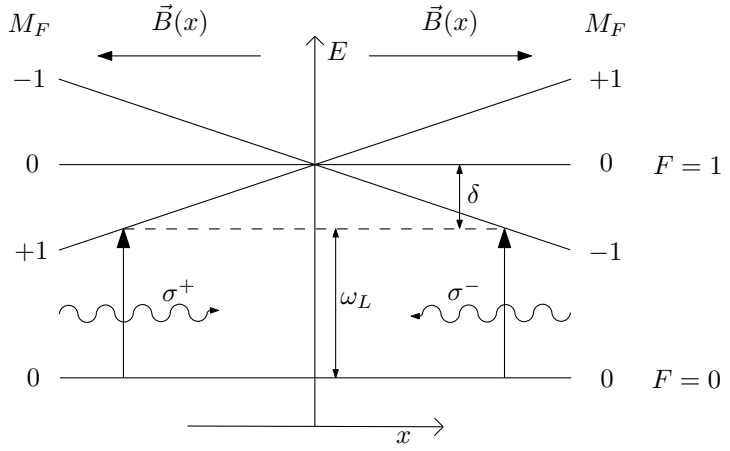

Figure 2.4: *Schematic view of a 1D MOT and a $F = 0 \rightarrow F = 1$ transition. A magnetic gradient along the x-axis creates a position dependent Zeeman shift of the $M_F = -1$ and $M_F = +1$ states. The two counterpropagating laser beams have an angular frequency ω_l and are detuned δ from the actual resonance. As an example, the $M_F = -1$ state shifts closer to resonance with the σ^- polarized beam for $x > 0$ than the $M_F = +1$ states. The atom therefore scatters more photons from the σ^- polarized beam than the σ^+ polarized beam and experiences a net force towards $x = 0$. This Figure is taken from [16].*

polarized light. Therefore the atom will only absorb photons coming from the right laser beam, which is σ^- polarized. The opposite happens for the $M_F = +1$ states on the left side of the graph; they will only absorb photons from the σ^+ polarized beam coming from the left. In this way the atoms only absorb photons coming from the off-axis direction they are at. This causes a net scattering force directed towards the minimum of the magnetic field (as that is also the minimum of the energy shift of the electronic levels). If the minimum of the magnetic field is created at the centre of an atomic beam and counterpropagating laser beams are perpendicular to the propagation direction of the beam, the beam can be compressed to a smaller radius.

The formalism for describing the scattering force caused by the Zeeman shift is similar to the scattering force due to the Doppler shift. Instead of the velocity dependent detuning $\pm kv$, the scattering force is modified by an added detuning $\pm g_F \mu_B \nabla B x/\hbar$. The position-dependent force is written as

$$F_{tot}(x) = \hbar k \frac{\gamma}{2} \frac{s_0}{1 + s_0 + (2(\delta - g_F \mu_B \nabla B x/\hbar)/\gamma)^2} - \hbar k \frac{\gamma}{2} \frac{s_0}{1 + s_0 + (2(\delta + g_F \mu_B \nabla B x/\hbar)/\gamma)^2}. \tag{2.17}$$

The spatial dependence of the total force is graphically identical to Figure 2.3, but the $v-$axis should be replaced by a $x-$axis. Similar to the Doppler cooling force, we can identify a linear regime for the compression force for small deviations from the central position $x = 0$, which in the ABLIS would be the z-axis (axis of propagation of the atomic beam). As a force with linear dependence on position always can be described using a spring constant κ, the same can be done for the magneto-optical force. This will be done during the derivation of the analytical model.

2.2 Analytical model

The new source concept can be fully described using the basic equations of magneto-optical cooling which we have discussed in the previous Section. We also mentioned the actual hyperfine level structure of the rubidium atoms. In order to estimate the performance of the ABLIS, we have to make a simplification in the level structure in order to be able to abtain an analytical result. We assume an ideal 2-level rubidium atom for which only $F = 0 \rightarrow F = 1$ transitions occur from the $5^2S_{1/2}$ state to the $5^2P_{3/2}$ state (see Figure 2.4 for the simplified level scheme).

Another simplification is our definition of the reduced brightness of the resulting ion beam. It is very difficult to obtain an accurate analytical result for the ionization of the neutral atomic beam [4]. Therefore we will calculate an equivalent reduced brightness, which is the reduced brightness we would achieve if we fully ionize the cooled and compressed beam neutral atomic beam. This will unevitably lead to an overestimation of the actual achievable reduced brightness, but still can be used as a good indicator of the performance of our source.

After we have discussed the analytical model, we investigate the discrepancy between both simplifications of the level structure and the reduced brightness by performing simulations which do include the magnetic substates of the hyperfine structure and include a more realistic ionization of the atomic beam. But first we calculate an analytical model.

One of the major assumptions we make to simplify the geometry of our setup is the paraxial approximation. This means that the opening angle θ, as shown in Figure 2.1, is much smaller than 1. The effusive flux Φ of the Knudsen cell going through the first aperture is [24, 27]

$$\Phi = \frac{1}{4} n_0 S \langle v \rangle \theta^2, \tag{2.18}$$

where $n_0 = p/k_B T_s$ is the particle density at the source, S the area of the orifice and $\langle v \rangle = \sqrt{8 k_b T_s / \pi m}$ the average velocity for a gas in thermal equilibrium in the Knudsen cell. The source temperature is T_s, k_B is Boltzmann's constant and m is the atomic mass. The source pressure p is given as $p = p_0 \exp[-T_0/T_s]$ [21], where p_0 and T_0 are atomic constants which are given in Table 2.1. For later purposes, we have calculated a fully analytical model of the flux going through the first aperture. The calculations are shown in Appendix A and give the same result as Equation 2.18 when applying the paraxial approximation. The angular spread of the effusing beam is given (in the paraxial approximation) by $\theta = d/l$, where d is the radius or half-width of the orifice. In the following analysis the orifice and apertures are assumed to be circular. In the simulations later on we use square apertures as they simplify the calculations. Therefore we interchange d often during this work for either the radius or the half-width of the orifice and apertures. This is not a problem, as our analysis in Appendix A shows that the difference between these two approaches is neglible and can be calculated explicitly if necessary. The length l is the distance between the source and the aperture. The initial reduced brightness B_i of the atomic beam at the aperture can be defined as [8]

$$B_i = \frac{eJ}{\pi k_B T} = \frac{eJ}{\pi k_B T_s \theta^2} = \frac{e^2 \Phi / S}{\pi k_B T_s \theta^2}, \tag{2.19}$$

where e is the elementary charge and $T_s\theta^2$ represents the effective transverse temperature of the atoms in the apertured beam. Here we have made the equivalent reduced brightness approximation

by simply multiplying the particle flux by the elementary charge, creating a current density $J = e\Phi$. The extra factor of e converts the brightness unit of Joules (J) to electron Volts (eV). If the beam is transversally cooled by the 2D-MOT to its minimum temperature, which is the Doppler temperature T_D, the brightness increases proportional to the ratio of the initial and final temperatures. That is, the brightness B_c after cooling is

$$B_c = B_i \frac{\theta^2 T_s}{T_D} = \frac{e\Phi/S}{\pi k_B T_D}. \tag{2.20}$$

From this Equation we learn that the ratio of the brightness after cooling and the brightness before cooling is

$$\frac{B_c}{B_i} = \theta^2 \frac{T_s}{T_D} \approx 240, \tag{2.21}$$

where we have assumed $\theta \approx 10$ mrad, $T_s \approx 350$ K and $T_D = 144$ μK (from Table 2.1). The choice of these numbers will be motivated later on, but here they are used to give an indication of the gain we can achieve.

The brightness can be further increased by compressing the beam. Using the formalism for Doppler cooling and magneto-optical compression using the Zeeman effect as described in Section 2.1.2, the total scattering force exerted by two counterpropagation laser beams with σ^+ and σ^- polarization on an ideal 2-level atom perpendicular to the propagation axis of the atomic beam, is [16, 25]

$$F_{tot}(x, v_x) = \hbar k s_0 \frac{\gamma}{2} \left[\frac{1}{1 + s_0 + \frac{4}{\gamma^2}(\delta - k v_x - \mu_B \nabla B x/\hbar)^2} - \frac{1}{1 + s_0 + \frac{4}{\gamma^2}(\delta + k v_x + \mu_B \nabla B x/\hbar)^2} \right]. \tag{2.22}$$

Here $k = 2\pi/\lambda$ is the wavenumber of the laser, γ the transition linewidth, $s_0 = I/I_s$ the saturation parameter of the laser, δ the detuning of the laser, v_x the transverse velocity of the particle, μ_B the Bohr magneton, ∇B the magnetic field gradient and x the transverse position of the particle. The Landé factors are assumed to be 1, the highest possible values for a $F = 0 \rightarrow F = 1$ transition.

The maximum acceleration of a particle is defined as

$$a_{max} = \lim_{v_x \rightarrow v_c, x \rightarrow 0} \frac{F_{tot}}{m}, \tag{2.23}$$

$$a_{max} = \frac{\hbar k}{m} \frac{\gamma}{2} s_0 \left[\frac{1}{1 + s_0 + \frac{4}{\gamma^2}(\delta - k v_c)^2} - \frac{1}{1 + s_0 + \frac{4}{\gamma^2}(\delta + k v_c)^2} \right], \tag{2.24}$$

where $v_c = |\delta/k|$ is the so-called capture velocity as introduced in Section 2.1.2. Using this definition of the capture velocity, we find

$$a_{max} = 8 F_0 \frac{-s_0 \delta_n}{(1 + s_0)(1 + s_0 + 16\delta_n^2)}, \tag{2.25}$$

where we define the maximum force as

$$F_0 = \frac{\hbar k \gamma}{m}, \tag{2.26}$$

and we have introduced the normalized detuning $\delta_n = -\delta/\gamma$ to simplify the equation.

The particles spend a time $\tau = L/\langle v \rangle$ in the 2D-MOT. As this timespan is finite, particles can only be compressed from a certain maximum radial position r_i from the central axis. The maximum range r_i of particles which can be compressed to the propagation axis of the beam is [25]

$$r_i = \frac{1}{4} a_{max} \tau^2, \tag{2.27}$$

where we have a counterintuitive extra factor 1/2. This factor is added to use an effective acceleration $a_{eff} = a_{max}/2$ to make sure that all atoms are cooled and compressed [25]. Equation 2.27 shows that all particles within an area $A_i = \pi r_i^2$ can be compressed. Ideally the first aperture size d should then be equal to r_i. If we set $d = r_i$, we can find τ and calculate L for a given source temperature T_s (as $\langle v \rangle$ depends on T_s). However, the definition of the maximum acceleration is dependent on the detuning, hence the size of the initial aperture is also dependent on the detuning. In order to reduce the number of variables, we would like to set a fixed size aperture size. A common detuning for laser cooling is $\delta = -\gamma/2$, where the Doppler temperature is minimized (as discussed in Section 2.1.2). This detuning will be chosen to define the maximum allowed transverse velocity to go through the first aperture, i.e. $v_{max} = v_c|_{(\delta=-\gamma/2)} = \gamma/2k$. In this way the opening angle θ is defined as

$$\theta = \frac{v_{max}}{\langle v \rangle} = \frac{\gamma}{2k} \sqrt{\frac{\pi m}{8 k_B T_s}}. \tag{2.28}$$

This definition of the opening angle ensures that the transverse velocities of the atoms stay well within the effective capture range of the 2D-MOT we are calculating. After finishing the analytical model we will also do simulations, where some attention will be given to the variation of the opening angle, but the predominant optimization will concern the parameters defining the 2D-MOT. By defining $r_i = d$ and using this fixed angle θ, the expansion stage length l can be calculated as $l = d/\theta$.

The final radius r_f of the beam can be calculated using equipartition of the potential energy of the compression force and the thermal energy of the beam. In Section 2.1.2 we show that the compression force is linear for small transverse positions x and a corresponding spring constant κ can be defined as

$$\kappa = \lim_{v_x \to 0, x \to 0} \Big[- \frac{\partial F_{tot}}{\partial x} \Big], \tag{2.29}$$

$$\kappa = -8 \mu_B \nabla B s_0 k \frac{\delta_n}{(1 + s_0 + 4\delta_n^2)^2}. \tag{2.30}$$

The equipartition of the potential energy and the thermal energy gives

$$\kappa r_f^2 = k_B T_D, \tag{2.31}$$

$$r_f = \sqrt{\frac{k_B T_D}{\kappa}} \tag{2.32}$$

Hence we can write the final beam area $A_f = \pi r_f^2$. Combining the brightness increase due to compression with the brightness increase due to cooling, we obtain

$$B_r = B_c \frac{A_i}{A_f} = \frac{e^2 \Phi / S}{\pi k_B T_D} \frac{A_i}{A_f}. \tag{2.33}$$

Similar to the gains in brightness due to cooling, the gains in brightness due to the compression of the beam is

$$\frac{B_r}{B_c} = \frac{A_i}{A_f} = \frac{d^2}{r_f^2} \approx 900, \tag{2.34}$$

where we use $d \approx 300$ μm and $r_f \approx 10$ μm. Both values will be justified later on. The combined increase in brightness due to cooling and compression then is

$$\frac{B_r}{B_i} = \frac{B_c}{B_i} \frac{B_r}{B_c} \approx 2 \cdot 10^5, \tag{2.35}$$

an increase of over five orders of magnitude!

Filling in the flux (Equation 2.18) and final beam size (Equation 2.32) in Equation 2.33, we find

$$B_r = \frac{8 e^2 \mu_B}{\sqrt{2\pi^5}} \frac{k}{\sqrt{m k_B^5}} \frac{p_0 \exp[-T_0/T_s]}{T_D^2 \sqrt{T_s}} \frac{\delta_n \nabla B s_0 S \theta^2}{(1 + s_0 + (2\delta_n)^2)^2}, \tag{2.36}$$

where we have used that $S = A_i$ in our model, i.e., the orifice of the Knudsen cell has an equal area as the first aperture. The choice of this specific geometry creates a good balance between a high flux and a reduced transverse velocity distribution.

However, we would like to investigate for what set of parameters this brightness increase is optimal. Combining the relevant equations for T_D and θ as described in this Section, we obtain the total analytical result for the final reduced brightness as

$$B_r^{ana} = \left[\frac{e^2 \mu_B \pi^{3/2}}{\sqrt{2} k_b^{7/2}} \right] \left[k p_0 \gamma^2 \sqrt{m} \right] \left[\frac{\nabla B L^4 s_0^3 \delta_n^7 \exp(-T_0/T_s)}{T_s^{7/2} (1 + s_0)^2 (1 + s_0 + 4\delta_n^2)^4 (1 + s_0 + 16\delta_n^2)^2} \right]. \tag{2.37}$$

We have grouped the different parameters in three sections: the natural constants (left), the atomic constants (center) and the experimental parameters which can be varied (right). This analytical result gives the maximum attainable brightness for any set of parameters[4].

Now we have developed a full analytical expression for the final equivalent reduced brightness of the beam, we can investigate for what practical experimental parameters we can optimize the brightness.

2.3 Analytical model parameters

In order to obtain sensible results from the analytical model, we use some common values for the different parameters and see what kind of performance the analytical model predicts. From flux calculations based on the models described in Appendix A, we select a typical value for the source

[4]The only constraint we have used in this model is, see Equation 2.28, the opening angle θ of the system.

temperature T_s to be 350 K in order to have a high enough flux without having a too short mean free path Λ, where Λ is defined as [27]

$$\Lambda = \frac{k_B T_s}{\sqrt{2}\pi p (2r_{vdW})^2}, \tag{2.38}$$

where $r_{vdW} = 0.3$ nm is the Van de Waals radius for rubidium [28]. The mean free path $\Lambda = 0.5$ m at $T_s = 350$ K, which is long enough for our purposes. Should we increase the source temperature to 400 K to increase the flux, the mean free path decreases to 21 mm, which is still acceptable.

The opening angle $\theta = d/l$ is given by Equation 2.28. For $T_s = 350$ K, this angle is $\theta \approx 8$ mrad. Also, the average velocity of the atoms in the beam is $\langle v \rangle \approx 300$ m/s. Filling in some typical laser cooling parameters of $s_0 \approx 1$ and $\delta \approx -\gamma/2$ (this choice of parameters minimizes the Doppler temperature), we find a damping time of the transverse temperature as [25] $\tau_{temp} = m/2\alpha \approx 20$ μs, with α taken from Equation 2.8. We also find an oscillation time $\tau_{comp} = 2\pi\sqrt{m/\kappa} \approx 380$ μs, which is the harmonic oscillation time of the atom's position due to the magneto-optical compression. In order to minimize the cooling and compression length, we choose $L = 5$ cm, corresponding to a transit time of $\tau = L/\langle v \rangle \approx 170$ μs. Compared to the damping time and the oscillation period, this should provide the atoms enough time to be cooled and compressed. At a later stage we will discuss whether this length can be optimized as well.

Using $L = 5$ cm, $T_s = 350$ K, $s_0 = 1$ and $\delta = -\gamma/2$, we can use Equations 2.25 and 2.27 to calculate a_{max} and estimate the aperture size to be $d \approx 300$ μm.

In order to have the apertured beam fully compressed, the magnetic compression capture range r_c can be defined in the same way as the capture velocity v_c for cooling. From Equation 2.22 and using a detuning $\delta = -\gamma/2$, which minimizes the Doppler temperatures, we find

$$\delta = \frac{\mu_B \nabla B r_c}{h}, \tag{2.39}$$

$$\nabla B = \frac{h\gamma}{2\mu_B r_c} \approx 0.7\ T/m. \tag{2.40}$$

Here we have set the capture range r_c equal to the size d of the initial aperture. In order to have efficient magneto-optical compression, we choose a magnetic gradient of $\nabla B = 1$ T/m.

Using these simple estimates, we can calculate the reduced brightness for the saturation parameter s_0 and the detuning δ using the analytical model. The result is shown in Figure 2.5. From this model, we find a maximum attainable brightness of $B_r = 2.1 \cdot 10^7$ A / m^2 sr eV for a detuning of $\delta = -0.8\gamma$ and a saturation parameter $s_0 = 2$. This is a few orders of magnitude larger than the reduced brightness UCIS, and one order of magnitude larger than the reduced brightness of the conventional LMIS source (see Table 1.1).

A summary of all parameters used in the analytical model is given in Table 2.2. These will be used as a starting point for the simulations, which will be discussed next.

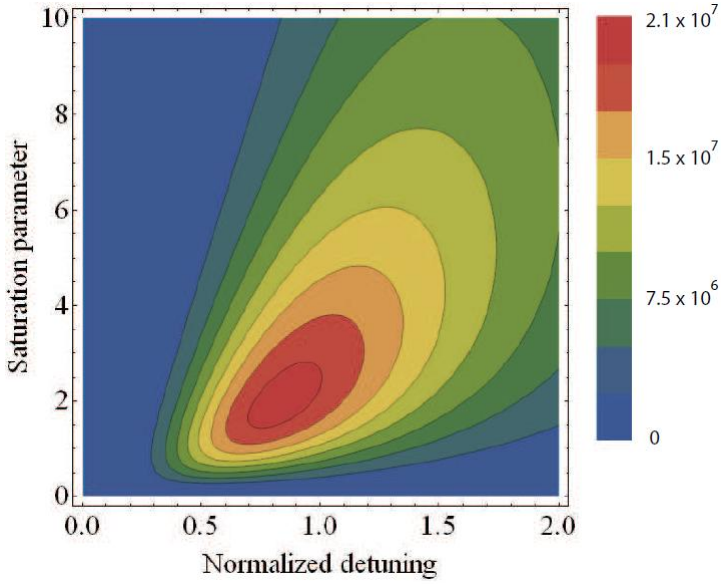

Figure 2.5: *Parameter space of the analytical reduced brightness B_r^{ana}, in units of A / m^2 sr eV for the saturation parameter s_0 and the normalized detuning $\delta_n = -\delta/\gamma$. The maximum reduced brightness is $B_r = 2.1 \cdot 10^7$ A / m^2 sr eV at $s_0 = 2$ and $\delta = -0.8\gamma$ ($\delta_n = 0.8$). The analytical model is based on an ideal 2-level ^{85}Rb atom and other parameters given in Table 2.2.*

Table 2.2: *Parameters given by analytical model.*

Parameter [unit]	Symbol	Analytical model
Opening angle [rad]	$\Delta\theta$	$8 \cdot 10^{-3}$
Expansion length [m]	l	$3.9 \cdot 10^{-2}$
First aperture size [m]	d	$3.1 \cdot 10^{-4}$
Cooling and compression stage length [m]	L	0.05
Source temperature [K]	T_s	350
Saturation parameter [-]	s_0	2
Detuning [γ]	δ	-0.8
Magnetic gradient [T/m]	∇B	1

Chapter 3

Simulation model

The developed analytical model shows some very promising results. However, we have made several assumptions in order to be able to calculate the analtyical model. First, the acceleration a_{max} experienced by the atoms is kept constant. In reality the atoms experience a continuously changing acceleration as function of their velocity. Further, this acceleration is calculated using a simplified 2-level atom with only a $F = 0$ ground state and a $F = 1$ excited state. In reality the rubidium isotopes have a $F = 3 \rightarrow F = 4$ and $F = 2 \rightarrow F = 3$ transition for ^{85}Rb and ^{87}Rb, respectively. This means that each hyperfine level exists out of $2F + 1$ magnetic substates M_F. Therefore the magneto-optical compression cannot be seen as a force caused by a single transition, but of multiple transitions. As a_{max} is lower and the compressing force is different due to the magnetic substate structure of the transitions, we expect that in reality the required cooling and compression stage length L should be longer than the length used in the analytical model.

Further, our analytical model assumes that all particles within our capture range r_c can be compressed to a beam with radius r_f within the cooling and compression stage length L. This is not true as the compressed beam will have developed an approximately radial symmetric density profile, from which only the central part will be cooled and compressed enough to contribute to the peak brightness of the beam. This is another reason why we calculate a 10% brightness of the beam (B_r^p, also mentioned in the Introduction), which is the brightness calculated from 10% of the particles of the beam which are closest to the propagation axis of the beam. This turns out to be an appropriate choice of our peak brightness and will be discussed and verified in Section 3.5.

Finally, we assume full radial cooling and compression in the analytical model. A more feasible approach would be cooling and compression along two orthogonal (x and y) directions transverse to the propagation of the beam as this is a more probable setup for the laser beams and the magnetic field, as in the latter geometry a quadrupole magnetic field can be used to create the Zeeman shift along the two transverse axes to compress the beam.

The previous remarks only concern the cooling and compression stage. However, another major assumption of the analytical model is our definition of the equivalent reduced brightness, where we calculate the brightness of the resulting ion beam by assuming that the neutral atomic beam is instantaneously ionized. We have not discussed the effects of ionization yet, but a common problem with ionizing high density neutral atomic beams is the Coulomb force the ions experience

immediately after ionization due to the short interatomic distances. Due to these Coulomb forces the ions will obtain increased longitudinal and transversal velocity distributions. As this process is disordered, these increased velocity distributions can also be interpreted as a form of heating. This effect is therefore also called stochastic heating [4].

After optimizing the experimental parameters of the cooling and compression stage for more realistic rubidium atoms, we will investigate the effect of stochastic heating for our best case cooling and compression scenario in order to show the possible performance of the ABLIS.

3.1 General approach

The total setup as shown in Figure 2.1 can be split in three parts, which are defined along the z (propagation axis) as: the initial expansion stage ($0 < z < l$), the laser cooling and compression (2D-MOT) part ($l < z < l + L$) and the ionization stage ($z > l + L$).

The analytical model as presented in the previous Chapter is based on a circular orifice and aperture geometry. As shown in Appendix A, there is only a slight difference between the choice of geometry (circles or squares). In the simulation model we choose square apertures for two reasons. First the calculations of the distribution functions becomes much easier, as the x and y coordinates and velocities of the particles can be considered to be independent[1]. This assumption can not necessarily be used here as in reality the x and y components are dependent as a photon absorbed from a laser beam in the x direction can emitted along the y direction due to stimulated emission from a laser beam along the y direction. Another effect is saturation of the transition due to absorption from the laser beam in the y direction, which results in a reduced scattering rate for the laser beam in the x direction. For a saturation parameter on the order of 1 and a detuning of $\delta \approx -\gamma/2$, the scattering rate is $R_{scatt} \approx 10^6$ s^{-1} (see Equation 2.2), whereas the lifetime τ_{exc} of the excited state is $\tau_{exc} \approx 27$ ns [16]. In this regime the atoms can thus be considered to be in the ground state and the effects of saturation and stimulated emission are neglible. For large transverse positions and velocities this calculation does not hold as the transitions are shifted into resonance due to the Zeeman and/or Doppler shift, but near the central axis this approximation is valid.

The simulation software COOL which is used to perform the laser cooling and compression calculations, only gives the result in 2D (one longitudinal and one transverse coordinate) [29]. Assuming the independent x and y position and velocity components of the atoms, the simulation of 2D cooling and compression can be performed for N atoms. Making sure that each pair of simulated atoms has the same longitudinal velocity v_z, which is being taken care of in the simulation code, we take the transverse position $x_{i,j}$ and velocity $v_{i,j}$ of two atoms i and j, and reconstruct a 3D final position $\vec{r}$ and velocity $\vec{v}$ of a single atom at the end of the cooling and compression stage (at $z = l + L$) as

$$\vec{r}(x_i, x_j) = x_i\vec{e}_x + x_j\vec{e}_y + (l + L)\vec{e}_z, \tag{3.1}$$

[1] In a radial geometry the x and y coordinates are coupled through the radial coordinate $r = \sqrt{x^2 + y^2}$, which makes calculation of the distribution functions much more complicated. An example of these extra complications can be seen in the flux calculations in Appendix A.

$$\vec{v}(v_i, v_j) = v_i\vec{e}_x + v_j\vec{e}_y + v_z\vec{e}_z. \tag{3.2}$$

In this way we simulate N particles in a 1D-MOT system and reconstruct $N/2$ particles in a 2D-MOT system.

In our simulations we will only vary one or two parameters in order to investigate its effects on the resulting brightness. However, in all cases we will use the other parameters as calculated in the analytical model given in Table 2.2.

3.2 Initial expansion stage

In the analytical model, Sec. 2.2, the flux Φ through the first aperture is given as

$$\Phi = \frac{1}{4} n_0 \langle v \rangle S \theta^2. \tag{3.3}$$

This equation is calculated in the paraxial approximation, and is based on a fully analytical flux calculation described in Appendix A. As θ is on the order of 10 mrad, the effective flux coming from the Knudsen cell and going through the aperture is only 0.01% of the flux emitted by the Knudsen cell. There will be further losses in the cooling and compression stage simulations and finally we will look at only 10% of the particles remaining in the end (in order to calculate the peak brightness B_r^p). In order to have a sufficient amount of particles at the end in order to suppress statistical fluctuations in the results, at least a million times more particles should be used initially! This results in severe computational demands which we are not able and willing to comply.

An alternative method is to calculate the flux at the first aperture and calculate the individual flux contribution of the particles at the aperture accordingly. In this way we can initialize the simulation at the first aperture and still calculate the final attained flux at the second aperture. Second we need to initialize the particles with the correct boundary conditions so the particle velocity and angular distributions correspond to a real apertured beam. This will be discussed next.

3.2.1 Particle velocity distribution

Because we use a Knudsen cell in thermal equilibrium, and the mean free parth is larger than the orifice size, the longitudinal velocity distribution of our beam at the first aperture can be described using the Maxwell-Boltzmann distribution

$$f_{vel}(v_z) = C_0 \frac{v_z^2}{v_\sigma^3} \exp\left[-\frac{1}{2}\left(\frac{v_z}{v_\sigma}\right)^2 \right], \tag{3.4}$$

where $v_\sigma = \sqrt{k_B T_s / m}$ is the thermal velocity of the atoms and C_0 a normalization constant. Here we have made the approximation that we deal with an effusing beam, and thus $v \approx v_z$. For $T_s = 400$ K, the thermal velocity is $v_\sigma \approx 195$ m/s for rubidium atoms. The particles are initialized using a Monte Carlo algorithm based on Equation 3.4, which gives a velocity distribution as shown in Figure 3.1.

Because the beam is apertured, the transverse velocity distribution will be more complicated. In order to calculate the transverse velocity distribution, we also have to consider the angular velocity distribution.

3.2.2 Spatial distribution

In Appendix A we calculate the asymmetry of the particle density at the first aperture. The asymmetry ϵ is defined using the particle density at the center n_c and the particle density at the border of the aperture n_b as

$$\epsilon = \frac{n_c - n_b}{n_c + n_b}. \tag{3.5}$$

For our geometric parameters $\epsilon \ll 10^{-4}$, which motivates our assumption that the spatial density distribution over the aperture is homogeneous. Assuming a homogeneous density distribution at the aperture will simplify the following calculations of the distribution functions enormously.

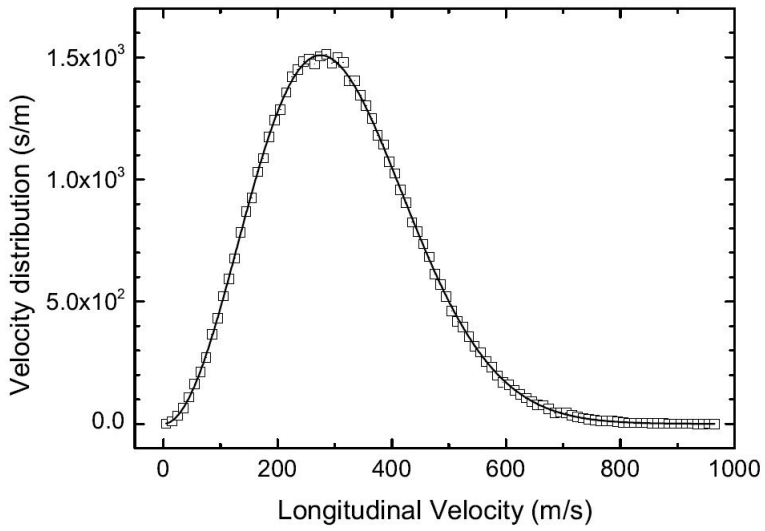

Figure 3.1: *Particle distribution of $N = 5 \cdot 10^5$ ^{87}Rb atoms at a temperature of $T_s = 400$ K as initialized using our Monte Carlo algorithm in the simulations. The distribution is normalized to N. The solid line is a fit of the normalized velocity distribution of Equation 3.4 and yields a thermal velocity of (194.7 ± 0.2) m/s, which is in good agreement with the calculated value $v_\sigma = 195$ m/s.*

3.2.3 Angular distribution

As the beam is apertured, the angular distribution will depend on the geometry of the setup. We have introduced to opening angle $\theta = d/l$, but now we want to calculate the angular distribution function. For this we use the variable angle α, for which $-\theta \leq \alpha \leq \theta$. In 1D, along the $x-$axis, the allowed range of angles α for a single particle passing through the aperture is

$$-\arctan\left(\frac{d-x_0}{l}\right) \leq \alpha \leq \arctan\left(\frac{d+x_0}{l}\right), \tag{3.6}$$

where x_0 is the initial position of the particle at the orifice ($-d < x_0 < d$), d is the half width of the orifice and the first aperture and l is the distance between the orifice and the aperture. Although the angular distribution goes as $f_{ang}(\alpha)d\alpha \sim \cos(\alpha)$ [24], this reduces to a homogeneous distribution $f_{ang}(\alpha)d\alpha = 1$ in the paraxial approximation ($\alpha \ll 1$). We initialize the angles by using a Monte Carlo algorithm to pick an angle α within the aforementioned limits (which are particle-dependent).

To test this algorithm, we would like to compare this to an analytically derived distribution function. From simple geometrical considerations the angular distribution function can be calculated as follows. Consider a 1D orifice and aperture as shown in Figure 3.2. For a specific angle $\alpha = (2d - x)/l$, where $x = 2d - l\tan(\alpha)$, only particles moving through the part $l_s = x$ of the orifice are able to move through the aperture. As we can assume that the particle density is homogeneous at the surfaces, the number of particles in a small interval $d\alpha$ is

$$f_{ang}(\alpha)d\alpha = C_1(2d - l\tan(\alpha))d\alpha; \quad -\arctan(2d/l) \leq \alpha \leq \arctan(2d/l), \tag{3.7}$$

where C_1 is a normalization constant and we have extended α to include the negative angles as well. As we have the paraxial approximation $d/l \ll 1$, we can linearize this distribution function as

$$f_{ang}(\alpha)d\alpha \approx C_1(2d - l\alpha) \tag{3.8}$$

If we use a total number of N particles in our simulation, the angular distribution can be normalized as

$$N = 2\int_0^{2d/l} f_{ang}(\alpha)d\alpha \approx 4C_1\frac{d^2}{l}. \tag{3.9}$$

Using $N = 5 \cdot 10^5$ particles and the geometrical parameters from Table 2.2, we expect a normalization constant of $C_1 = 5.12 \cdot 10^7$ rad m^{-1}. An example of the angular distribution after initialization using our Monte Carlo method is shown in Figure 3.3. Fitting the histogram using Equation 3.8, we find a value of $C_1 = (5.11 \pm 0.06) \cdot 10^7$ rad m^{-1}, in excellent agreement with our calculation.

Since we now have initialized the particle positions, longitudinal velocities and the angles, we could start simulating. For completeness we verify whether we obtain the expected transverse velocity distribution.

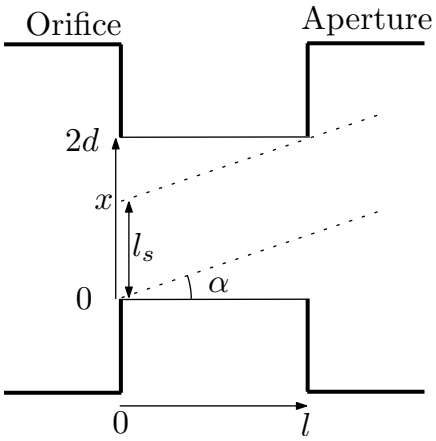

Figure 3.2: *Schematic 1D view of the orifice and aperture. For a specific angle* $\alpha \approx (2d - x)/l$*, particles emitted from the part* l_s *of the orifice can move through the aperture.*

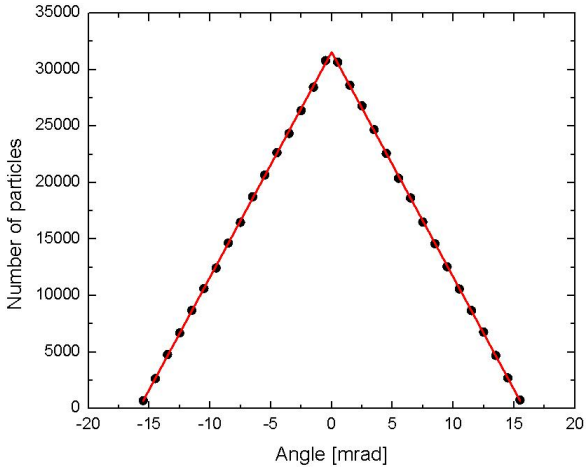

Figure 3.3: *Angular distribution histogram acquired after an initialization Monte Carlo routine for* $N = 5 \cdot 10^5$ *particles as described in the text. The bin size is* 10^{-3} *radians. The geometrical parameters are given in Table 2.2. The angular distribution is fitted using Equation 3.8 and yields a normalization constant* $C_1 = (5.11 \pm 0.06) \cdot 10^7$ *rad* m^{-1}*, which is in excellent agreement with our calculated result.*

3.2.4 Transverse velocity distribution

Using the angular and longitudinal velocity distribution, the transverse velocity distribution can be calculated. The number of particles with a transverse velocity v_x and a longitudinal velocity v can be discribed using the following distribution function

$$f(v_x, v)dv_x dv = f_{ang}(\alpha) f_{vel}(v_z) d\alpha dv_z. \tag{3.10}$$

We cannot state *a priori* that the left hand distribution function is a product of two independent distribution functions (of v_x and v_z), as both velocities are correlated through the paraxial relation $v_x \approx \alpha v_z$. Using this relation to substitute α and making the approximation $v \approx v_z$, we effectively make a coordinate transformation with the corresponding Jacobian

$$J(v_x, v) \approx J(v_x, v_z) = \Big| \frac{\partial(v_x, v_z)}{\partial(\alpha, v_z)} \Big| = v_z. \tag{3.11}$$

This allows us to rewrite Equation 3.10 as

$$f(v_x, v_z)dv_x dv_z = f_{ang}(v_x/v_z) f_{vel}(v_z) \frac{dv_x dv_z}{v_z}. \tag{3.12}$$

The transverse velocity distribution of the particles can now be obtained by integrating this equation over v_z. However, for each transverse velocity v_x there must be a lower cutoff in the longitudinal velocities that contribute to this transverse velocity. This is due to the fact that the maximum angle of a particle in this geometry is approximately $2d/l$ and for a transverse velocity v_x the lowest longitudinal velocity $v_{z,min}$ that leads to such transverse velocity at its largest angle, is

$$v_{z,min} = \frac{l}{2d} v_z. \tag{3.13}$$

The transverse velocity distribution

$$f_{trans}(v_x) = \int_{v_{z,min}}^{\infty} f(v_x, v_z)dv_z = \int_{v_{z,min}}^{\infty} f_{ang}(v_x/v_z) f_{vel}(v_z) \frac{dv_z}{v_z}, \tag{3.14}$$

$$f_{trans}(v_x) = \int_{v_{z,min}}^{\infty} C_2 \Big(2d - l\frac{v_x}{v_z}\Big) \frac{v_z^2}{v_\sigma^3} \exp\left[-\frac{1}{2}\Big(\frac{v_z}{v_\sigma}\Big)^2 \right] \frac{dv_z}{v_z}, \tag{3.15}$$

$$f_{trans}(v_x)dv_x = C_2 \frac{2d}{v_\sigma} \exp\left[-\Big(\frac{l}{d}\frac{v_x}{2\sqrt{2}v_\sigma}\Big)^2 \right] dv_x - C_2 l \sqrt{\frac{\pi}{2}} \frac{v_x}{v_\sigma^2} \left(1 - erf\Big[\frac{l}{d}\frac{v_x}{2\sqrt{2}v_\sigma}\Big] \right) dv_x. \tag{3.16}$$

Here $erf(z)$ is the error function defined as $erf(z) = (2/\sqrt{\pi}) \int_0^z \exp[-t^2]dt$. Similar to the angular distribution function, we can normalize the transverse velocity distribution to the total number of particles N used in the simulations:

$$N = 2 \int_0^{\infty} f(v_x)_{trans} dv_x, \tag{3.17}$$

where the factor 2 arises from the fact that Equation 3.16 is only valid for $v_x \geq 0$ but also works for $v_x \leq 0$ by using the substitution $v_x \to -v_x$. The integral can only be evaluated numerically. Using

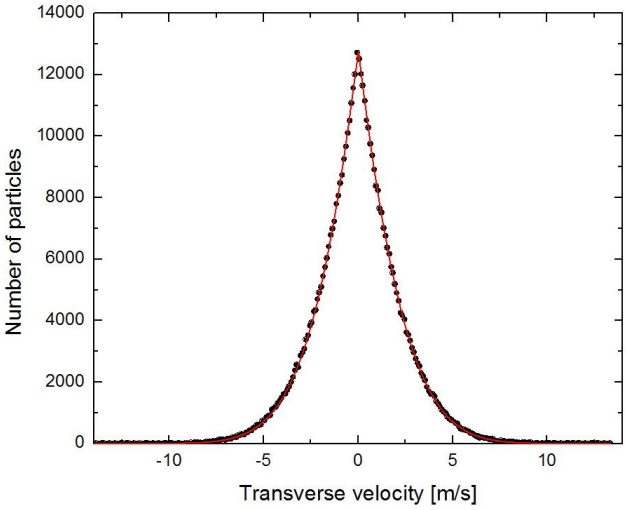

Figure 3.4: *Transverse velocity distribution histogram acquired after an initialization Monte Carlo routine for $N = 5 \cdot 10^5$ particles as described in the text. The bin size is 0.1 m/s. The geometrical parameters are given in Table 2.2. The transverse velocity distribution is fitted using Equation 3.16 and yields a normalization constant $C_2 = (4.055 \pm 0.003) \cdot 10^9$ m^{-1}, which is in adequate agreement with our calculated result.*

the parameters $N = 5 \cdot 10^5$, a thermal velocity of $v_\sigma = 195$ m/s and the geometric parameters as given in Table 2.2, we find a normalization constant of $C_2 = 4.074 \cdot 10^9$ m^{-1}. An example of a histogram of the transverse velocities (which is a result of our Monte Carlo initialization of the angles and the longitudinal velocities) is shown in Figure 3.4. The distribution is fitted using Equation 3.16 and gives a normalization constant $C_2 = (4.055 \pm 0.003) \cdot 10^9$ m^{-1}, which is within 0.5% of our calculation.

3.2.5 Defining the flux at the first aperture

It is numerically difficult to calculate the flux going through the first aperture as each particle has a different contribution to the total flux in our simulations. Hence we designed a normalization method which enables us to calculate the flux at the end of the cooling and compression stage.

Our method is quite straightforward. From our analytical calculation shown in Appendix A, we can exactly calculate the flux Φ_i at the first aperture. As the particle density at the aperture can be considered to be homogeneous, it is easy to initialize the particles using a Monte Carlo algorithm for the particle position, longitudinal velocity and the angle of emission, according to the methods described above. Once the longitudinal velocities have been initialized, we can calculate the initial flux $\Phi_i = (1/4) n_0 S \langle v \rangle \theta^2$. We define a weighting constant C_{flux} as

$$C_{flux} = \frac{\Phi_i}{\sum_{j=1}^{N} v_z^j}, \tag{3.18}$$

where the sum is defined over all N particles at the first aperture and v_z^j is each particle's longitudinal velocity. At the second aperture we can choose a different aperture size d_f to aperture the

beam. The resulting number of particles N_f going through the final aperture is a function of d_f. The final flux Φ_f can thus be calculated as

$$\Phi_f = C_{flux} \sum_{j=1}^{N_f(d_f)} v_z^j, \tag{3.19}$$

which enables us to accurately calculate the final flux and thus the current of the resulting ion beam.

3.2.6 Concluding remarks on the expansion stage

We have shown how we can effectively initialize the simulation at the first aperture with a flux and transverse and longitudinal velocity distributions corresponding to an atomic beam effusing from a Knudsen cell. In this way we save a lot of computer time when performing the simulations. Contrary to the analytical model, we use a square aperture geometry to simplify the calculations. This is no problem, as the full flux calculations in Appendix A show that the difference between a circular and square geometry is neglible, and can be exactly corrected for.

The final check we can do is calculate the emittance of the atomic beam after it passes the first aperture using the distribution functions and obtaining the emittance from the initialization in the COOL program. In 1D we use the x-axis similar to the previous calculations and the angular and position distribution function of the particles is

$$f(\alpha, x)d\alpha dx = C_3 \left[H(x + l \arctan\left(\frac{d-x}{l}\right)) - H(x - l \arctan\left(\frac{d+x}{l}\right)) \right], \tag{3.20}$$

where $H(z)$ is the Heaviside step function

$$H(z) = \begin{cases} 1 & z \geq 0, \\ 0 & z < 0. \end{cases} \tag{3.21}$$

The distribution function is normalized to unity which gives a normalization constant $C_3 = l/4d^2$. Using the normalized distribution function, we can calculate the relevant moments of the distribution:

$$\langle x\alpha \rangle = \frac{1}{3}\frac{d^2}{l}, \tag{3.22}$$

$$\langle \alpha^2 \rangle = \frac{2}{3}\frac{d^2}{l^2}, \tag{3.23}$$

$$\langle x^2 \rangle = \frac{1}{3}d^2. \tag{3.24}$$

From this we can calculate the geometric emittance in the $x-$direction as

$$\varepsilon_x = \sqrt{\langle x^2 \rangle \langle \alpha^2 \rangle - \langle x\alpha \rangle^2} = \frac{1}{3}\frac{d^2}{l}. \tag{3.25}$$

We check this result with the COOL software. Using the geometric parameters from Table 2.2 emittance calculated in the program is $\varepsilon_x = 1.0338 \cdot 10^{-6}$ m rad, within 0.07% of the theoretical value of $\varepsilon_x = 1.0345 \cdot 10^{-6}$ m rad.

Now that we have checked the validity of the initialization, we discuss the laser cooling and compression stage as simulated by the COOL software.

3.3 Laser cooling and compression stage

The laser cooling and compression stage is simulated using the COOL software [29]. Essentially the program calculates all velocity changes of particles due to absorption and emission of photons during each timestep and propagates the particles with the new velocities. As discussed in Section 2.1.1, the rubidium hyperfine levels actually exist out of multiple magnetic substates. This is taken into account using a Monte Carlo algorithm based on the photon absorption rate of each possible magnetic substate transition.

Further Monte Carlo algorithms determine the angle of emission of the photon. The random angle of emission leads to the diffusive heating mechanism as discussed in Section 2.1.2. In this way the atoms can only be cooled down to the Doppler temperature.

After emission of a photon the final magnetic substate of the atom is picked by a Monte Carlo algorithm using the appropriate Clebsch-Gordan coefficients to weigh the transition probabilities. The program accepts any set of particles with transverse and longitudinal velocities, such as the particles we initialize using the procedures described in Section 3.2. The program allows any laser beam orientation and polarization. As mentioned in the introduction to the simulations, the 2D-MOT is actually simulated as a 1D-MOT in the COOL software. We define two counterpropagating laser beams with σ^+ and σ^- polarization and the appropriate cooling transition wavelength and detuning. We also define a magnetic field which has a gradient ∇B along the transverse direction.

As we can define the hyperfine (and magnetic substate) structure ourselves, we can first simulate an ideal 2-level ^{85}Rb atom (with only $F = 0 \rightarrow F = 1$ transitions) to see if the simulation results converge to the analytical model. After the verification, we introduce the ^{85}Rb and ^{87}Rb hyperfine and magnetic substate structures as discussed in Section 2.1.1 to make the simulations more realistic.

The software has some limitations. The COOL software only calculates the atom trajectories along one transverse axis and one longitudinal axis and we are thus limited to simulate a 1D-MOT. Assuming that the two transverse coordinates for a 2D-MOT are independent, we can still use this software to reconstruct 3D motion of the particles. The validity of this assumption and the method used to reconstruct the 3D motion are discussed in Section 3.1.

A common problem with laser cooling with rubidium[2] is the unwanted transition $F = 3 \rightarrow F = 3$ which is only 120 MHz below the transition frequency of the cooling transition [22]. It can therefore be significantly excited due to the linewidth of the laser and power broadening of the transition. This is shown in Figure 3.5. As a fraction of the atoms are actually excited to the excited $F = 3$ state, atoms can decay either to the ground $F = 2$ or $F = 3$ state. The latter state does not provide a problem as the atom can be excited to the $F = 4$ state again. However, if the atom decays to the $F = 2$ ground state, it becomes transparent for the laser frequency as the $F = 2$ ground state lies 3 GHz below the $F = 3$ ground state [22]. A common solution, as used in the UCIS setup [17, 18], is to have a second laser which pumps the atoms from the ground state $F = 2$ to the $F = 3$ excited state, from which they can decay to the usable $F = 3$ ground state or back to the unusable $F = 2$ ground state, at which point they are being pumped to $F = 3$ again. This process is called repumping.

[2]This example is based on the hyperfine structure of ^{85}Rb, but is also present with ^{87}Rb.

Although the magnetic substate structure of the atom is taken into account, only the $F = 3 \rightarrow F = 4$ cooling transition is used in the simulations. Hence atoms can never decay to any other hyperfine state, such as the $F = 2$ ground state. This simplification in the simulations is identical to the assumption that there are ideal repumping laser present which make sure that all atoms can only be in the $F = 3$ ground state at all times.

A further limitation is the fact that the software does not take the actual intensity profile or wavefront of the laser beams into account. Hence the laser beams used in the simulations are ideal plane-waves and have 'top-hat' intensity profiles. Further, the software does not take particle collisions into account which probably start playing a role as the beam is compressed and the density increases. Increased absorption due to the increased optical thickness of the cooled and compressed beam is also ignored.

Although the software has limitations, it is a useful tool to investigate some effects of a real 2D-MOT. But we should first check whether the simulation results make sense, which means that we have to check whether the simulations results are similar to the analyical model results.

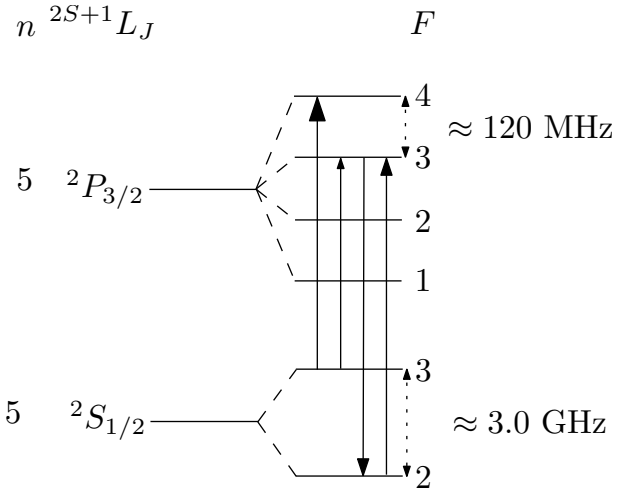

Figure 3.5: ^{85}Rb *level scheme. The left arrow is the* $F = 3 \rightarrow F = 4$ *transition, also known as the cooling transition. When pumping this transition, the* $F = 3 \rightarrow F = 3$ *transition (second arrow from the left) is also excited. From the excited* $F = 3$ *state atoms can decay to the ground* $F = 2$ *state (third arrow from the left) from which they are transparent to the laser. A second laser, which drives the* $F = 2 \rightarrow F = 3$ *transition (fourth arrow from the left), is used to pump the atoms into the excited* $F = 3$ *state from which they decay either to the ground* $F = 3$ *state and can be used again, or they decay to the* $F = 2$ *ground state, from which they are being pumped again. This process is called repumping.*

3.4 Comparison between the simulation results and the analytical model

Now that we are acquainted with the basic principles of the COOL software, we have to check whether this software actually produces similar results as predicted by the analytical model. In order to do this check we perform simulations based on the atomic data from Table 2.1 and the experimental parameters from the analytical model given by Table 2.2. As the analytical model is based on an ideal 2-level atom, we also use an ideal 2-level ^{85}Rb atom in our simulations. Some of the parameters will be changed in order to investigate the parameter-space of the simulations and to check whether they correspond to the predictions of the analytical model using the brightness as defined in Equation 2.36. Also, the peak brightnesses given in this Chapter will be equivalent peak brightnesses i.e. peak brightness obtained if the full beam is ionized without experiencing any stochastic heating effects, which are briefly mentioned at the beginning of this Chapter. This definition is identical to the equivalent brightness definition used for the analytical model.

The basic idea of these checks has been mentioned at the beginning of this Chapter: as the acceleration which the atoms experience is not constantly equal to a_{max}, it takes a more time and interaction length in the 2D-MOT to effectively cool and compress the beam. If we want to compare the simulation model to the analytical model, we therefore have to look at the final peak brightness as function of the length L of the 2D-MOT. We also look at the peak brightness as function of several other parameters to investigate whether the general behaviour of the peak brightness corresponds to the behaviour predicted by the analytical model.

The parameters used in the simulations are given in Table 2.2. In the simulations where we vary a single parameter, all other parameters are given by this Table.

In the first simulations we vary the source temperature T_s and 2D-MOT length L. The results are shown in Figure 3.6. First we note that the peak brightness increases as the source temperature increases. This is caused by the increased flux and therefore increased current of the ion beam. We also see that the peak brightness increases as L is increased and tend to converge to a single line, which is the brightness as calculated by the analytical model. We can conclude that the simulation results become very similar to the analytical model when the interaction length L becomes very large (20 times larger than the analytical model length). Additionaly we see that the peak brightness increases by approximately a factor of 10 when the interaction length is increased by a factor of 2. We will use this information when optimizing the system.

Next we vary the detuning δ, and the result is shown in Figure 3.7. We see that for detunings around $\delta \approx -\gamma/2$, the attainable peak brightness is maximal. It decreases for larger detunings as the laser frequency is too off-resonant and does not create a large enough scattering force to cool and compress the beam. Again we see that the simulation results become similar to the analytical model as long as the interaction length in the simulations is much longer than in the analytical model. For equal interaction lengths in the analytical model and the simulations ($L = 5$ cm), the peak brightness shows different behaviour. By increasing the detuning beyond $\delta = -\gamma/2$ the velocity capture range of the Doppler cooling force is increased, but this does not contribute much as the opening angle θ is fixed using the aformentioned detuning (see Sec. 2.2) and therefore

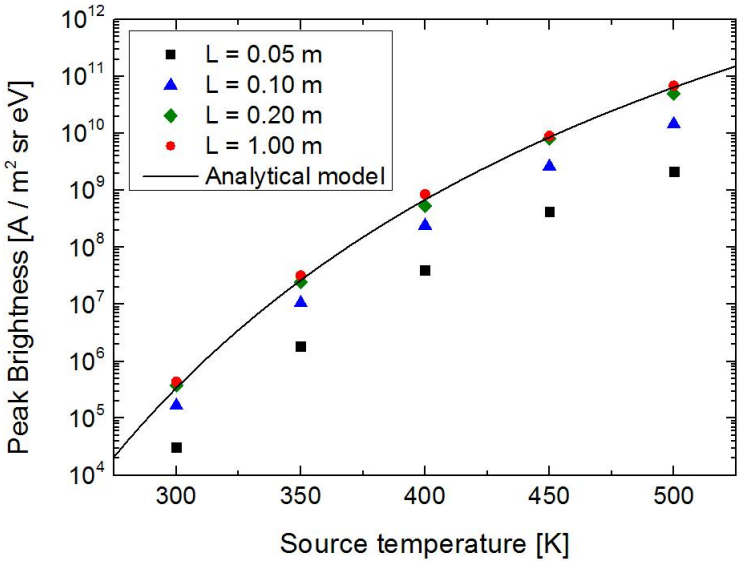

Figure 3.6: *Peak brightness B_r^p as function of the source temperature T_s for different 2D-MOT lengths L. We can draw two conclusions. First the simulation results converge to the analytical model when the interaction length becomes much (20 times) larger than the interaction length of the analytical model (which is 5 cm). Second, the peak brightness increases by approximately an order of magnitude by doubling L to 10 cm.*

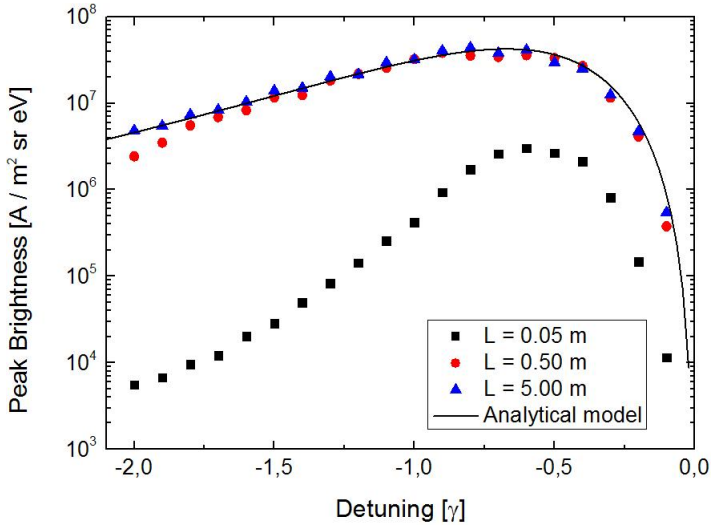

Figure 3.7: *Peak brightness B_r^p as function of the detuning δ for different 2D-MOT lengths L. Again we see that the simulation results converge to the analytical model as long as the interaction length is* much *longer than used in the analytical model. We also see that the simulations show different behaviour compared to the analytical model for the same interaction length $L = 5$ cm.*

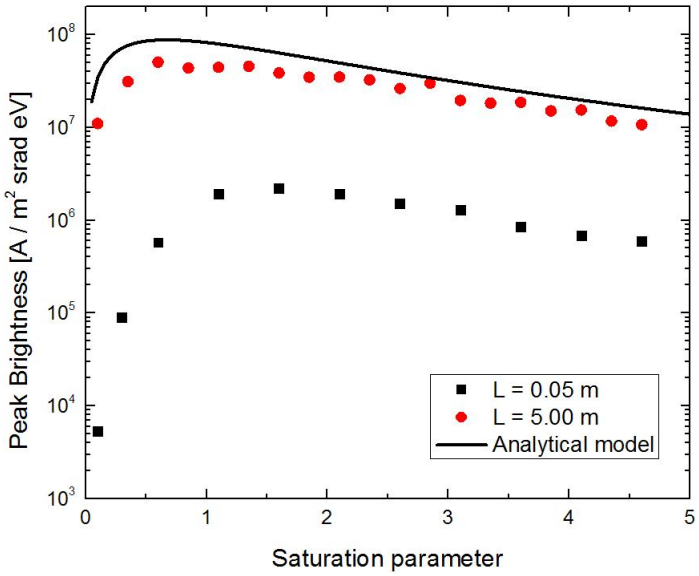

Figure 3.8: *Peak brightness B_r^p as function of the saturation parameter s_0 for different 2D-MOT lengths L. Again we see that the simulation results converge to the analytical model as long as the interaction length is* much *longer than used in the analytical model.*

extending the velocity capture range only results in less effective cooling. To understand this we have to consider the maximum acceleration a_{max} and the spring constant κ from Equations 2.25 and 2.30; both will decrease if δ increases and thus the atomic beam is cooled and compressed less efficiently. This explains the faster decay in peak brightness in the simulations than in the analytical model.

We finally do a third set of simulations, where we vary the saturation parameter s_0, as shown in Figure 3.8. Again we see that the simulation results and the analytical model agree for large interaction lengths, but usually the simulation results are much lower than the analytical model. Similar to the results discussed when varying the detuning, the low saturation parameter decreases both a_{max} and κ and therefore results in less efficient cooling and compression. Therefore the maximum of the peak brightness is at a higher saturation parameter in the simulations than for the analytical model.

3.4.1 Concluding remarks on the laser cooling and compression stage

We can conclude that the COOL software does provide results which agree with the analytical model if the simulation geometry is given enough interaction length to fully cool and compress the beam.

There is one additional remark to be made. We have shown that the brightness Equation 2.36 as function of the source temperature, detuning and saturation parameter does agree with the behaviour as observed in the simulation results, but we have to make one adjustment. The Doppler temperature T_D as calculated in Section 2.1.2 and used in the analytical model, assumes that all particles are in equilibrium between the Doppler cooling and the diffusive heating mechanism as

discussed in Section 2.1.2. However, as the beam is not fully cooled and compressed in the 2D-MOT, the particles actually have a different transverse temperature than expected. Therefore we calculate the temperature $k_B T_{sim} = m(\langle v^2 \rangle - \langle v \rangle^2)/2$ of the transverse velocities of the particles in the simulation and then calculate . Substituting this value for the Doppler temperature in Equation 2.36, we find the agreement between the analytical model and the simulation results as discussed above. We should note that we calculate the peak brightness of the beam using only 10% of the particles closest to the central axis. These particles are colder than particles which are further away from the beam, as they have not been cooled and compressed much yet due to their large transverse velocities and/or positions. Therefore the temperature T_{sim} obtained from the simulation is usually below the transverse temperature of the total beam.

3.5 Validity of the peak brightness definition

In the Introduction we discuss the peak brightness B_r^p which is the equivalent reduced brightness of 10% of the particles which are closest to the axis of propagation of the beam at the end of the 2D-MOT. We use this definition throughout all our COOL simulations as there is no numerical method to determine the maximum brightness of the beam in the limit $d_f \to 0$, where d_f is the half-width of the second aperture, which is the aperture behind the 2D-MOT. A brief discussion about the validity should be in order.

Here we present one comparison based on optimized simulation which will be discussed later in this Chapter. The simulation parameters are given in Table 3.1, but here we use the results just to show the validity of our definition. Figure 3.9 shows the equivalent reduced brightness B_r of an optimized ^{87}Rb beam, which is calculated by including all particles that move through the final aperture with half-width d_f. We also show the peak brightness B_r^p for comparison, which is calculated using only 10% of the particles of the beam which are closest to the central axis. We see that B_r stays constant and equal to B_r^p for aperture sizes up to $d_f \approx 7$ μm. For larger aperture sizes the less cooled and compressed (and thus more divergent) part of the beam goes through the aperture, which effectively decreases the reduced brightness. Simultaneously we see that in the same aperture size range $d_f < 7$ μm, the current of the resulting beam increases proportional to the surface of the aperture ($I \sim d_f^2$), indicating that the particle density is almost homogeneous near the central axis of the beam.

We can conclude that our definition of the peak brightness is in good agreement with the reduced brightness for small aperture sizes. We also see that there is a simple relationship between the aperture size and the current in the $1 - 1000$ pA range, and we will discuss this in Section 3.6.4.

3.6 Simulation results using 'real' rubidium

In the previous Section we have established that the COOL software accurately simulates the laser cooling and compression of the atomic beam. However, to verify the simulation results with the analytical model presented in Section 2.2 we used ideal 2-level ^{85}Rb atoms in which only

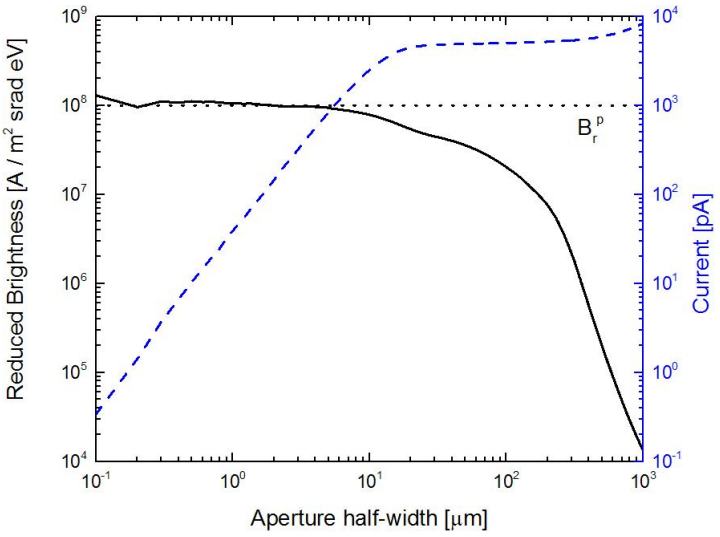

Figure 3.9: *Equivalent reduced brightness B_r of the beam at the end of the 2D-MOT as function of the final aperture half-width d_f. The solid line is B_r calculated using all particles which pass through the aperture. The dotted line is the calculated peak brightness B_r^p by taking 10% of the particles which are closest to the axis of propagation into account. The blue dashed line is the ion beam current corresponding to the different aperture sizes. There is no data for aperture sizes below 0.1 μm, as the calculated brightness becomes unreliable due to poor particle statistics. The data is from the optimized ^{87}Rb beam simulation with the simulation parameters given by Table 3.1.*

$F = 0 \rightarrow F = 1$ transitions occur. At the beginning of this Chapter, we have also discussed the motivation to include a more complicated level structure of the atoms. The following simulations will all be performed with 'real' rubidium atoms, which is either the ^{85}Rb $F = 3 \rightarrow F = 4$ transition with its magnetic substates or the ^{87}Rb $F = 2 \rightarrow F = 3$ transition with its magnetic substates. The cooling transition for ^{87}Rb has lower total angular momentum terms as its nuclear spin quantum number is $I = 3/2$ instead of $I = 5/2$ for ^{85}Rb [21]. As the total angular momentum terms are lower for ^{87}Rb than for ^{85}Rb, there are less magnetic substates M_F, as the degeneracy of the magnetic substates is $2F + 1$. As a result, ^{87}Rb has less possible transitions than ^{85}Rb. As will see later in this Section, this will have an effect on the performance of the ABLIS for either isotope.

As the simulations will be performed seperately for each isotope, the results are valid when assuming that a purified source is used. In this way we learn the most about the different isotopes, but in practice the usage of purified sources is much more expensive than using a natural mixture of the isotopes. We will address this in the conclusion of the simulation results when discussing the maximum achievable brightness in our simulations.

First we will look at the effects of the experimental parameters on the performance of the 2D-MOT. Then we will show some results which indicate that there are possibilities to improve the final peak brightness even beyond the results we will discuss here.

The geometric parameters d and l of the initial expansion stage will not be changed; here we

fully rely on the numbers given by the analytical model, which incorporates the capture velocity and the capture range of the 2D-MOT. Although any exploration of this parameter-space might be an interesting exercise, it does not lead to much more insight in the laser cooling and compression physics than the other parameters $s_0,\ \delta,\ \nabla B,\ L$ and T_s. But first we will take a look at the actual output of the COOL simulations.

3.6.1 Optimization the ABLIS using 'real' rubidium

There are five parameters which can be optimized in our source: the saturation parameter s_0, the detuning δ, the magnetic gradient ∇B, the cooling and compression stage length L and the source temperature T_s. Each of these parameters has a different effect on the atomic beam. An increased saturation parameter s_0 will cool and compress the beam faster, but the final attainable temperature which can be achieved by the beam will be increased due to an increase photon scattering rate (also see the Doppler temperature as discussed in Section 2.1.2). This leads to a decreased peak brightness. The detuning δ is coupled to the saturation parameter s_0 through the Doppler temperature as $\delta = (\gamma/2)\sqrt{1+s_0}$, which follows from minimizing the final temperature of the beam (also discussed in Section 2.1.2). An increased magnetic gradient ∇B decreases the capture range and the efficiency of the compression, and it is also technically more challenging to achieve large gradients. The compression stage length L can be varied to change the efficiency of the cooling and compression stage as essentially the length determines the net amount of photons each atom can scatter. As we have seen in e.g. Figure 3.6 an increased length improves the peak brightness, but as part of our optimization we are only interested in small variations of the length. Finally, the source temperature T_s can be varied to increase the total flux, hence the brightness of the final beam. As the temperature also determines the transverse velocity spread, there is a nontrivial relation between the source temperature and the length of the cooling and compression stage in order to obtain the highest peak brightness.

Optimizing the saturation parameter and the detuning

The simulation results for different values of s_0 and δ are shown in Figure 3.10 for ^{85}Rb. The peak brightness is optimal for a detuning $\delta \approx -\gamma/2$, which makes sense when comparing to the analytical model. Further, the peak brightness increases rapidly for $s_0 < 1.5$ but saturates for $s_0 > 1.5$. Therefore we can conclude that a detuning of $\delta = -\gamma/2$ and $s_0 = 1.5$ are the minimum requirements to produce the peak brightness. Similar results are obtained when performing the simulation using ^{87}Rb, but the peak brightness is alway approximately a factor of 2 higher than the ^{85}Rb results. We will explain this difference in after we discuss the results when considering the influence of the magnetic field gradient.

Optimizing the magnetic field gradient

Next we look at the magnetic field gradient ∇B. Figure 3.11 shows the peak brightness for two sets of simulations using either one of the rubidium isotopes. The ^{87}Rb beam obtains high peak brightness for $\nabla B \approx 2.5$ T/m, whereas the ^{85}Rb beam requires a higher gradient $\nabla B \approx 3$ T/m,

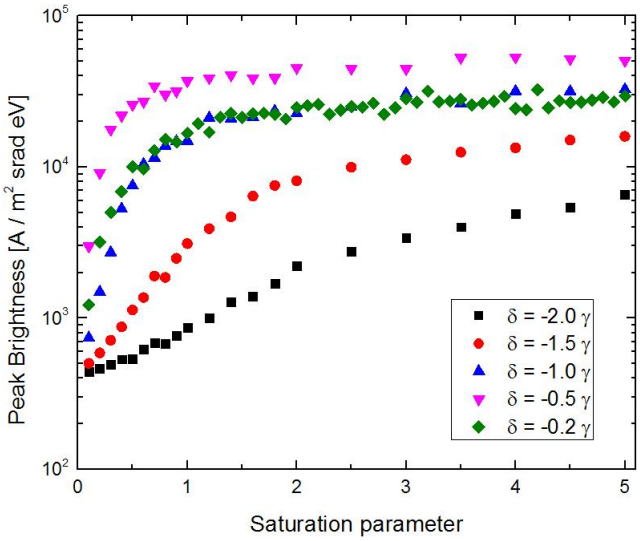

Figure 3.10: *Peak brightness B_r^p of a ^{85}Rb beam as function of the saturation parameter s_0 for different detunings δ. The other simulation parameters are given in Table 2.2.*

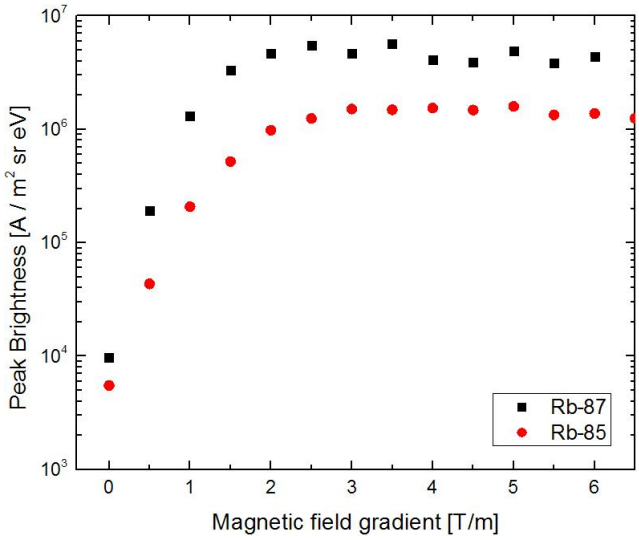

Figure 3.11: *Peak brightness B_r^p of a ^{85}Rb and a ^{87}Rb beam as function of the magnetic field gradient ∇B. The other simulation parameters are given in Table 2.2.*

although the exact gradient is quite arbitrary to choose.

The different behaviour can be explained by considering the relative transition strengths of the different isotopes, which for circular polarized light (as this polarization is used in the 2D-MOT) are shown in Figures B.3 and B.4 in Appendix B. The average Zeeman shift weighted by the magnetic substate transition strengths is 75% of the maximum Zeeman shift for ^{85}Rb and 83% of the maximum Zeeman shift for ^{87}Rb (the calculation is shown in Appendix B). As the maximum Zeeman shifts of both isotopes is equal, the difference in average Zeeman shift explains why ^{87}Rb is compressed more efficiently than ^{85}Rb.

Optimizing the cooling and compression stage length

As discussed earlier, the cooling and compression stage length L determines the amount of time the atoms spend in the 2D-MOT and thus the peak brightness of the beam. Figure 3.12 shows the peak brightness of both rubidium isotopes as function of the length. It is obvious that we are far from saturation of the peak brightness, i.e., the length is too short to cool and compress the beam to a minimum width and temperature as calculated in the analytical model. However, we see that increasing the length by a factor of 2 from $L = 5$ cm to $L = 10$ cm increases the peak brightness by a factor of approximately 3 for a ^{85}Rb beam and a factor of 10 for a ^{87}Rb beam! Because of this large increase in brightness at a relative low cost of increase in length, we decide to increase the 2D-MOT length to $L = 10$ cm.

Optimizing the source temperature

The final parameter is the source temperature T_s. Increasing the source temperature will increase the width of the velocity distribution. As a result also the transverse velocity distribution will be broadened, making it more difficult to cool and compress the beam. However, an increased source temperature will increase the flux and therefore the final current of the ion beam. Hence there is a trade-off between an increased flux and decreased cooling and compression efficiency. Additionally, the mean free path Λ (see Equation 2.38 in Section 2.3) of the atoms decreases as the source temperature increases. If the mean free path becomes shorter than the size of the orifice of the Knudsen cell, collisions within the orifice's walls will start to play a role and affect the velocity distribution of the particles. This effect is not included in the simulations but should be taken into account when optimizing the source temperature.

Figure 3.13 shows the peak brightness for 2-level ^{85}Rb compared to the peak brightnessess of the realistic ^{85}Rb and ^{87}Rb atoms. In these simulations we have used the optimized parameter values, which are given in Table 3.1, in order to get an indication of the actual performance of the ABLIS. First, Figure 3.13 shows no obvious optimum in the temperature range $320 - 420$ K. It is not relevant to increase the source temperature beyond 420 K as the mean free path of the atoms, given in Equation 2.38, will be too short. Second, we see that the performance of the ideal 2-level atom is always better than the realistic atoms and that the ^{87}Rb isotope performs approximately 5 times better than the ^{85}Rb isotope. In order to have an acceptable mean free path and the maximum peak brightness, we use a source temperature of $T_s = 400$ K (for which $\Lambda \approx 21$ mm $> d \approx 309$ μm). We see that we can obtain a peak brightness of 10^8 A / m^2 srad eV with the ^{87}Rb isotope!

3.6.2 Concluding remarks on the parameter optimization

We have implemented both rubidium isotopes with their magnetic substate structures in the COOL software in order to optimize the parameters of the ABLIS. We observe significant differences between the analytical 2-level atom model and the real isotopes, first due to the fact that the atoms experience a different force than assumed in the analytical model and second due to the different Zeeman shifts for the magnetic substate transitions than the simplified $F = 0 \rightarrow F = 1$

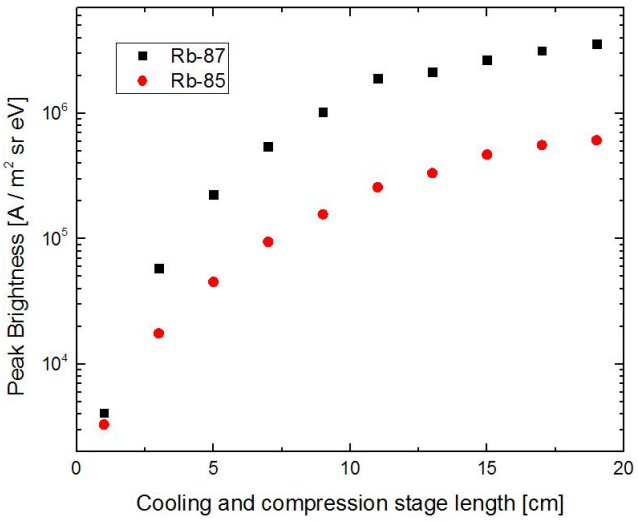

Figure 3.12: *Peak brightness B_r^p of a ^{85}Rb and a ^{87}Rb beam as function of the cooling and compression stage length L. The other simulation parameters are given in Table 2.2.*

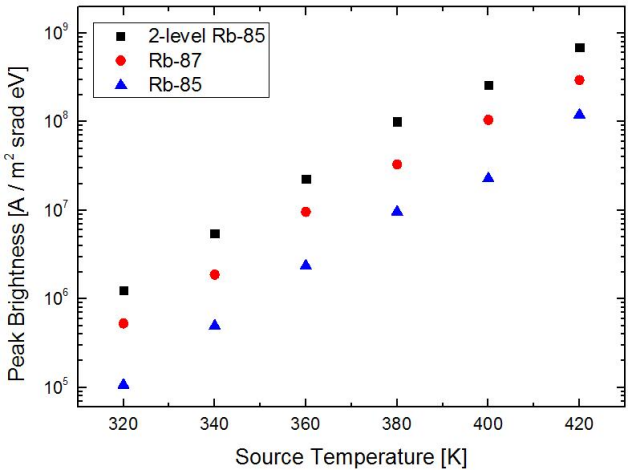

Figure 3.13: *Peak brightness B_r^p of a ^{85}Rb and a ^{87}Rb beam and an ideal 2-level ^{85}Rb beam as function of the source temperature T_s. Here we have used all parameter values as given in Table 3.1.*

Table 3.1: *Final parameters for both rubidium isotopes compared to the parameter values given by the analytical model.*

Parameter [unit]	Symbol	Analytical model	^{85}Rb	^{87}Rb
Opening angle [rad]	$\Delta\theta$	$8 \cdot 10^{-3}$		
Expansion length [m]	l	$3.9 \cdot 10^{-2}$		
First aperture size [m]	d	$3.1 \cdot 10^{-4}$		
Cooling and compression stage length [m]	L	0.05	0.10	
Source temperature [K]	T_s	350	400	
Saturation parameter [-]	s_0	2	1.5	
Detuning [γ]	δ	-0.8	-0.5	
Magnetic gradient [T/m]	∇B	1	3	2.5

transitions.

Further, the difference in magnetic substate structure between the two isotopes is expressed in all simulation results as a different attainable peak brightness for both isotopes. Nonetheless we find peak brightnessess of $10^7 - 10^8$ A / m^2 srad eV, depending on the isotope. However, this assumes that a purified, single isotope, source is used. In order to calculate the peak brightness of an atomic beam with a natural mixture of both isotopes, and assuming there is only one laser to cool and compress a single isotope, the peak brightness has to be weighted using the natural abundance of the relevant isotope. From Figure 3.13, one can then find a peak brightness of $0.722 \times 2 \cdot 10^7 \approx 1.4 \cdot 10^7$ A / m^2 srad eV for ^{85}Rb and $0.278 \times 10^8 \approx 2.3 \cdot 10^7$ A / m^2 srad eV for ^{87}Rb. This is an impressive result compared to the LMIS and the UCIS discussed in the Introduction.

There are still two issues to be considered. First, we have discussed the longitudinal energy spread in Section 3.7 but we have not done any calculations or simulations regarding the longitidunal energy spread after the ionization of the atomic beam. Second, we do not know what the stochastic heating effects due to ionization of the atomic beam are. These issues will be discussed in Section 3.8.

3.6.3 Is this the limit?

A relevant question at this point should be whether the calculated peak brightnesses of $10^7 - 10^8$ A / m^2 srad eV are the absolute limit of the ABLIS performance. As we have seen, the source temperature (see Figure 3.13) leaves some room for improvement, but this also depends on the geometry of the expansion stage.

As discussed before, the expansion stage has two parameters: the expansion stage length l and the Knudsen cell orifice half-width (or radius) d. We have kept these two parameters constant during the simulations using 'real' rubidium in order to reduce the number of parameters. However, for future use it might be interesting to vary these geometric parameters as well.

The same simulation parameters are used as for the simulations in the previous Section, and they are given in Table 2.2. We use the ideal 2-level rubidium atom in order to exclude any of the

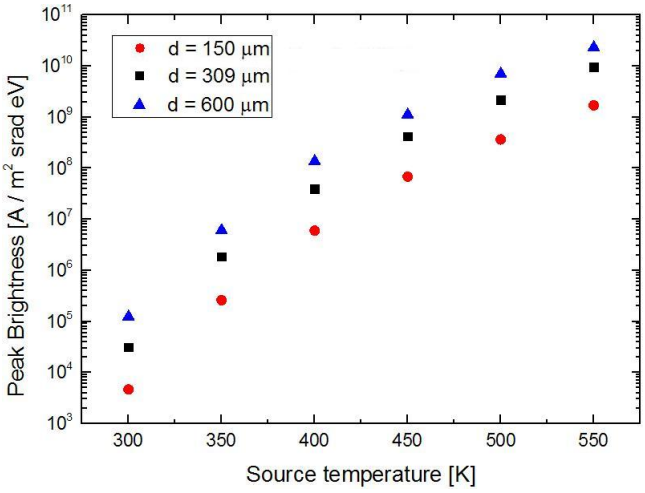

Figure 3.14: *Peak brightness B_r^p as function of the source temperature T_s for different orifice and aperture half-widths d. An ideal 2-level rubidium atom is used to exclude isotope effects. The other simulation parameters are given in Table 2.2.*

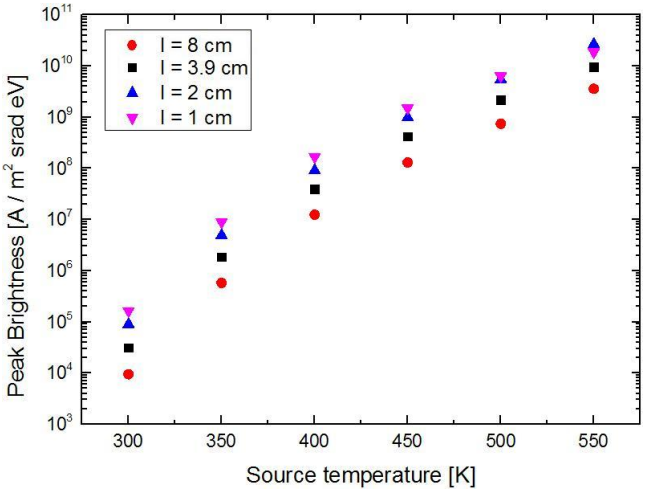

Figure 3.15: *Peak brightness B_r^p as function of the source temperature T_s for different expansion stage lengths l. An ideal 2-level rubidium atom is used to exclude isotope effects. The other simulation parameters are given in Table 2.2.*

isotope effects, as we are only interested in the effect of the geometry. The source temperature is varied in order to give an idea whether the two geometric parameters can be optimized. The results are given in Figures 3.14 and 3.15. The attainable peak brightness scales roughly quadratically with the geometric parameters as the compression and cooling efficiency of the 2D-MOT does not change significantly. For high temperatures $T_s > 500$ K, the peak brightness increases differently as the increased source temperature also leads to an increase in the width of the transverse velocity distribution. In this regime the cooling and compression stage becomes less efficient. This could be solved by increasing the length of the cooling and compression stage or the gradient of the magnetic field, but this increases the technical demands on the resulting apparatus.

Hence we conclude that the geometry of the expansion stage can be further optimized. As mentioned earlier, we will keep this information for future use and continue the current simulations using the standard values as given in Table 2.2.

3.6.4 Atomic beam real-space and phase-space distribution

The real-space and phase-space distribution shown in this Section as an example output of the COOL software, is the actual distribution of the atomic beam used in the ionization simulations in Section 3.8. The phase-space distribution of the particles is shown in Figure 3.16. Only the $(x - v_x)$ distribution is shown as it is similar to the $(y - v_y)$ distribution due to the symmetry of our setup. It is clear that the majority of the particles are cooled and compressed, but there are still many particles (see the inset in Figure 3.16) which are not cooled or compressed at all. This is due to the finite length of the cooling and compression stage.

The spatial distribution of the particles is shown in Figure 3.17. We see that the beam has four 'arms' along the x- and y-axes as the pairs of laser beams are perpendicular and therefore do not provide radially symmetric compression. If we calculate the rms width of the whole ensemble, we find $\sigma_x^{rms} \approx \sigma_y^{rms} = 285$ μm. If we only take the particles which are within a square aperture with half-width $d_f = 30$ μm (which is the black square in Figure 3.17), we find $\sigma_x^{rms} \approx \sigma_y^{rms} = 2.9$ μm, which is much closer to the expected width of the beam from the analytical model. It is therefore necessary to aperture the beam before ionization in order to obtain the peak brightness.

As aperturing the beam will change the number of ions, the size of the aperture is linked to the total current of the beam. The half-width d_f of the aperture for different currents of the resulting ion beam for this specific case is shown in Figure 3.18. A linear fit $y = ax + b$ of this log-log plot in the range of 1-1000 pA gives $a = (0.507 \pm 0.003)$ log(μm)/log(pA) and $b = (-0.779 \pm 0.006)$ log(μm) resulting in the approximate relation

$$d_f \approx 10^{-0.78}\sqrt{I} \approx 0.17\sqrt{I}, \tag{3.26}$$

where d_f is in μm and I in pA. This relation is only valid for this specific beam, and should be recalculated when using different parameters in the cooling and compression simulations.

In Section 3.8 the brightness will be shown as a function of the ion beam current. Using this equation one can always find the corresponding aperture size.

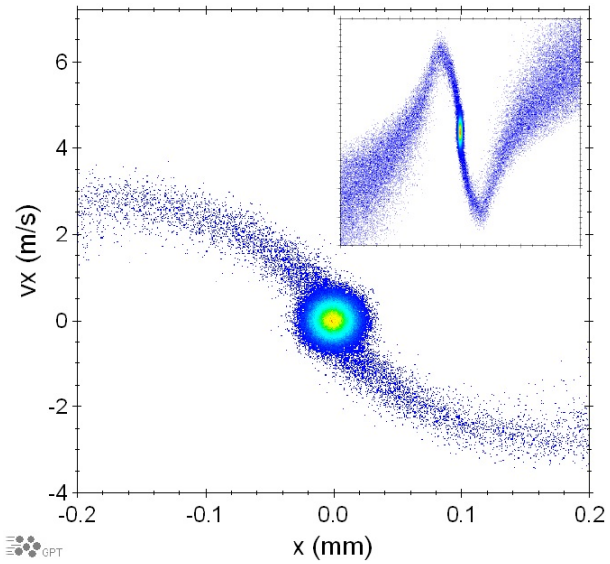

Figure 3.16: *Particle $(x-v_x)$ phase-space distribution at the end of the 2D-MOT for $N = 1.4{\cdot}10^5$ particles. Due to the symmetry along both x- and y-axes, we only have to consider the x-axis distribution. The plot is binned and the color code represents the areal particle density, ranging from blue (low density) to yellow (high density). The inset has a larger x scale, ranging from -1 mm to 1 mm. The data is from the optimized ^{87}Rb beam simulation with the simulation parameters given by Table 3.1.*

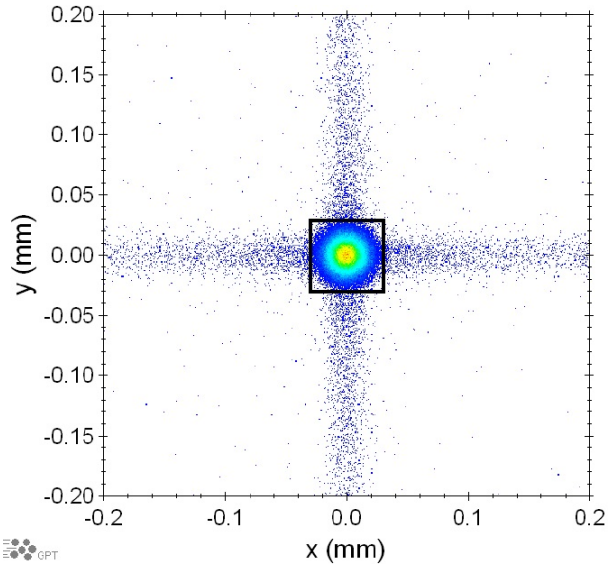

Figure 3.17: *Spatial distribution of the atoms at the end of the 2D-MOT as they are loaded into GPT. The plot is constructed by binning the atoms and the color code represents the areal particle density ranging from blue (low density) to yellow (high density). The beam exists of $N = 1.4 \cdot 10^5$ particles, and 95% of the particles are contained within the square box with half-width $d_f = 30$ μm. The data is from the optimized ^{87}Rb beam simulation with the simulation parameters given by Table 3.1.*

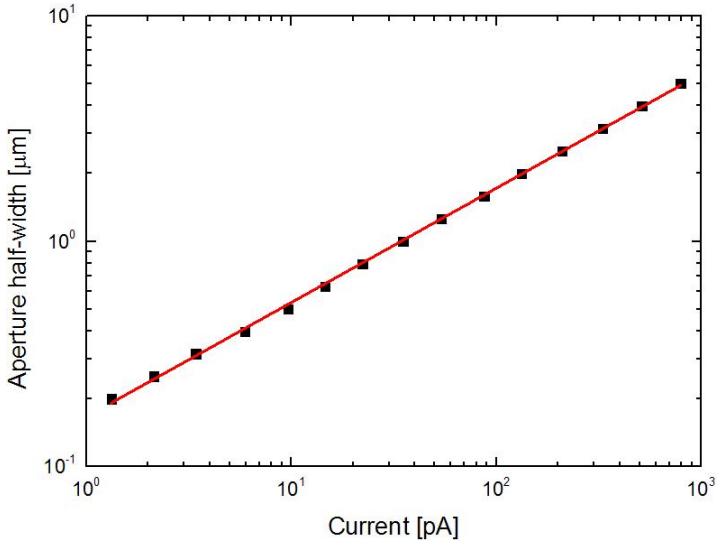

Figure 3.18: *Aperture half-width d_f for different currents of the resulting ion beam. The straight line is a fit with the parameters given in the text. The data is from the optimized ^{87}Rb beam simulation with the simulation parameters given by Table 3.1.*

3.7 Creating an ion beam

In the Introduction of this report we discuss two figures of merit which define an ion beam: the brightness and the longitudinal energy spread. We have optimized the brightness of the beam using magneto-optical cooling and compression techniques, but we have not discussed the longitudinal energy spread. An increased longitudinal energy spread leads to larger chromatic abberations, which limits the final spotsize when focusing the ion beam. Therefore we now discuss the ionization process of the cooled and compressed ion beam.

In the introduction of this Chapter we briefly mentioned stochastic heating effects. As we create a cooled and compressed neutral atomic beam, the atoms will be quite close to each other and, after ionization, experience large Coulomb forces from their neighbouring ions [4]. Due to these forces the ions will be accelerated outward in the transverse and longitudinal directions. The acceleration in the transverse directions means that the transverse velocity distribution will become broader, and the same goes for the longitudinal velocity distribution. As the disordered increase of the width of the velocity distribution is associated with heating, this process is also called stochastic heating [4]. Here the phrase 'stochastic' refers to the fact that this is a disordered many-body effect and is difficult, if not impossible, to calculate for each particle analytically. Although some analytical results can be presented, as in [4], we choose to simulate the ionization of the neutral atomic beam and observe the stochastic heating effects in the simulations results.

One method to reduce the stochastic heating effects is to reduce the time the ions spend in each others' neighbourhood. This can be achieved by applying an electric field $\vec{E}$ in the ionization stage. However, as the atoms are ionized in a finite ionization laser beam size, the spatial spread of the ionization process itself increases the energy spread. Assuming an rms laser spotsize σ_L,

the energy spread due to ionization in an electric field E is [17]

$$\sigma_U = e\sigma_L E. \tag{3.27}$$

For an atomic beam with a longitudinal temperature of 400 K, the longitudinal energy spread σ_U of the beam is can be calculated using Equation 1.1 and gives $\sigma_U \approx 8$ meV. In order to minimize the stochastic heating effects, one has to maximize the electric field to the order of $E \approx 1$ MV/m, which is a realistically attainable field. However, to be a competitive alternative to the other technologies discussed in the Introduction, the energy spread should be less than 1 eV. This means that the laser spotsize should be around $\sigma_L \approx 1$ μm. This a quite a small spotsize, but there are commercial focusing objectives available which are able to provide sub-micron spotsizes in the correct wavelength range[3]. Therefore we use a 1 μm rms spotsize ionization laser beam in our simulations.

In the simulations of the ionization process we will only use the best results we have from the laser cooling and compression simulations, in order to show the best possible performance as a 'proof of principle' of the ABLIS. This is the result using the simulation parameters given by Table 3.1 using a ^{87}Rb source, i.e. a purified single isotope source.

3.7.1 Ionization stage

Once the beam is cooled and compressed using the COOL simulations, we save all transverse positions and velocities (both transverse and longitudinal) of the particles. Using the flux weighting coefficient C_{flux} as discussed in Section 3.2, we can calculate the flux at the second aperture. The data is then loaded in the General Particle Tracer (GPT) program [30]. The flux is converted into a particle rate through the aperture to implement a longitudinal spatial spread of the particles to create a realistic particle beam. In order to investigate the effects of ionization as function of beam size and current, we apply an aperture half-width d_f and the program omits all particles which are not within the aperture. As the aperture size determines the number of atoms that will be ionized, simulating the resulting brightness as function of d_f is identical to simulating the resulting brightness as function of current. The exact relation between current and d_f will be discussed later.

Immediately after the aperture plane, GPT propagates the particles along the z-axis through a 1 μm rms beam radius of a two-stage ionization laser beam. The two-stage ionization process is not implemented in the code; the GPT code only ionizes the atom. In the region of overlap between the laser beam and the atomic beam the ionization fraction is set to one, which is realistic for a high power CW laser beam, and the atoms are ionized along z-axis with a quasi-Gaussian probability distribution, which is a model for the fact that not each atom is ionized the instant it enters the laser beam.

The ionization takes place in a constant electric field $\vec{E}$ which accelerates the ions along the beam's axis of propagation away from the ionization laser beam. In this way the Coulomb interaction time between the ions near the ionization site is reduced. The ions are accelerated to a

[3]For instance the LMH-20X-532 High-Power Nd:YAG MicroSpot Focusing Objectives provided by Thorlabs, which is able to provide a 0.8 μm diffraction limited spot size.

plane 10 cm behind the ionization site, where the resulting phase-space density distribution of the particles is calculted to determine the reduced brightness of the beam.

In order to observe the stochastic heating effect, we first benchmark the GPT simulations by turning off the pairwise Coulomb interactions and calculate the resulting brightness. Having this benchmark, we turn the pairwise Coulomb interactions on and calculate the resulting brightness for different aperture sizes and electric fields.

3.8 Stochastic heating

As discussed in Section 3.7, the magnitude of the electric field determines the longitudinal energy spread of the ion beam. However, a large electric field reduces the amount of time the ions spend close to each other and thereby reduces the stochastic heating effects [4]. Therefore we create the ion beam in two different electric fields: a field of 0.5 MV/m for which the longitudinal energy spread stays below 1 eV, which is better than the LMIS, and a field of 2.5 MV/m for which we expect a larger longitudinal energy spread but less stochastic heating effects as the ions are accelerated faster away from the ionization laser beam.

The results are given in Figure 3.19 and show three cases. The first case is a benchmark where the atoms are ionized but the space charge forces are not taken into account. This shows that the reduced brightness of the beam stays approximately equal. The other two cases are the ionized beams with either one of the discussed electric fields, and we observe several effects.

First it is obvious that the reduced brightness of the ion beam decreases at some point as the current becomes too large and stochastic heating effects dominate. This is caused by the fact that although the ion density stays the same independent of current, a larger current requires a larger beam size and ions 'see' much more neighbours in the transverse direction. This reduces the reduced brightness as there are now much more Coulomb forces in the transverse direction causing stochastic heating.

Second, the ion beam extracted in the electric field of 2.5 MV/m has an overall higher reduced brightness than the ion beam extracted in the 0.5 MV/m electric field as the ions spend less time close to each other. However, the ion beam extracted in the higher electric field also has a 50% energy spread of $\sigma_U = 3.3$ eV, which is 4.7 times larger than the energy spread of the lower electric field case (which is $\sigma_U = 0.7$ eV). However, in both cases we see that the reduced brightness stays approximately $2 \cdot 10^7 - 4 \cdot 10^7$ A / m^2 srad eV for currents up to 10's of pA! This is caused by the low ion density in the beam: as the ions have more neighbours along the axial direction in stead of the radial direction, they experience Coulomb forces predominantly in the longitudinal direction. Therefore the ionization only affects the longitudinal energy spread of the ion beam, and not the reduced brightness. This is called the pencil beam regime and enables us to increase the current of the ion beam without having to pay the price by getting a smaller reduced brightness [9, 31]. Evidently the current can only be increased up to the point that the number of neighbouring atoms (in the transverse direction) becomes too large and the ions experience dominating Coulomb forces in the radial direction.

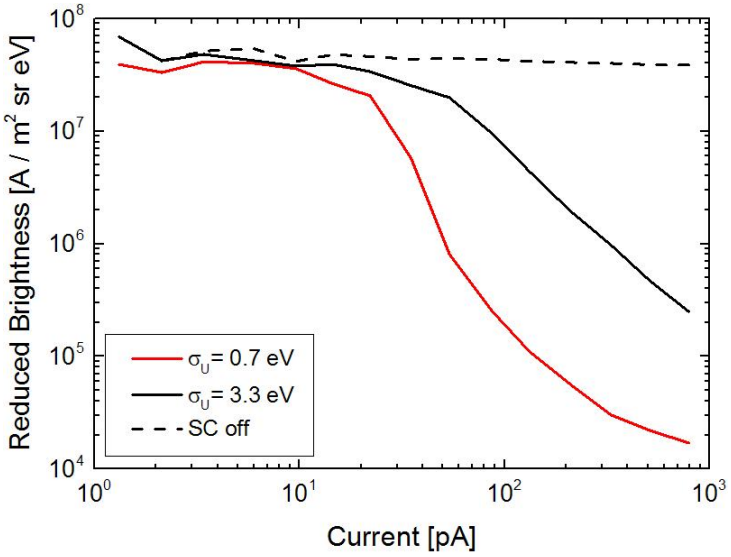

Figure 3.19: *Reduced brightness B_r plotted versus the ion beam current. The curves are calculated with GPT by considering all particles in the ion beam. The dashed line ('SC off') is our benchmark, as no space charge forces are taken into account and all fluctuations are due to fluctuations in the particle distributions of the beam. The solid lines are in presence of space charge forces. The black solid line is for an extraction field of 2.5 MV/m. The red solid line is for an extraction field of 0.5 MV/m. σ_U represents the 50% energy spread of the resulting ion beam.*

3.9 Conclusion on the ABLIS simulations

In this Chapter we have established a new concept for an ion beam source, the Atomic Beam Laser-cooled Ion Source (ABLIS). An analytical model has been developed to establish the initial parameters of the model, such as the source temperature and the length of the cooling and compression stage. From this analytical model we move to simulations with the COOL software, which incorporate the hyperfine structure of the atoms and the finite interaction time of the setup. Convergence of the simulations to the analytical model is tested and confirmed by increasing the interaction length. The simulations are then used to optimize the experimental parameters. We find that both rubidium isotopes have different performances, primarily due to their different hyperfine structures. After optimization of the experimental parameters, we use the GPT software to investigate the stochastic heating effects when ionizing the atomic beam. We observe stochastic heating of the ion beam, but the ion beam is in the pencil beam regime which enables us to keep the maximum reduced brightness whilst having ion beam currents of 10's of pA. Our best result is obtained with a pure $^{87}Rb^+$ beam, where we obtain a reduced brightness of $B_r = 2 \cdot 10^7$ A / m^2 srad eV with a current of 22 pA and a longitudinal energy spread of 0.7 eV using the simulation parameters of the cooling and compression stage given in Table 3.1. These simulations are performed for a specific case, but work as a proof of principle of the ABLIS. The reduced brightness is 10 times larger than the reduced brightness of the LMIS with a 10 times smaller energy spread, showing that the ABLIS is a good alternative to current technologies.

Chapter 4

Experimental setup

One of the main components of the ABLIS is the cooling and compression stage which we call the 2D-MOT or MOC. The 2D-MOT exists of two main components which create the magneto-optical cooling and compression forces: the light field created by the laser beams and the magnetic gradient field created by a quadrupole magnet. Both components need yet to be established in an experimental environment. Here we focus on the laser system.

As discussed in Section 3.6.1 and shown in Table 3.1, there is a specific detuning of the laser frequency from the rubidium cooling transition for which the final brightness of the beam is optimized. Further, as shown in Figure 3.10, the final brightness is quite sensitive to the actual detuning of the laser. Typically the detuning should be accurate within 10%. Here the accuracy both refers to the absolute frequency and the average frequency fluctuations of the laser. The optimal detuning is about half of the linewidth of the transition, which is approximately 3 MHz below the transition frequency of the ^{85}Rb cooling transition. This means we would like to stabilize the laser frequency to 3 MHz below the cooling transition frequency with an accuracy of 300 kHz and fluctuations of at most 300 kHz.

In this Chapter we discuss our laser system and the methods with which we want to stabilize our laser frequency. We will also discuss the active components used in our stabilization system. In the next Chapter we will discuss our experimental results.

4.1 Laser system

The laser system used in the lab is a Titanium:Sapphire[1] (Ti:Al_2O_3) ring laser pumped by a Verdi laser[2]. The Titanium:Sapphire (Ti:Al_2O_3) crystal based laser system has a very broad gain bandwidth ranging from approximately 650 to 1000 nm [32, 33], hence the major advantage of this system is its tunability. Additional optical components in the laser cavity ensure single mode emission of light.

The first optical element used to tune the laser frequency is a birefringent filter, which can be used approach the desired laser frequency [33]. For a higher accuracy, two etalons are used.

[1] Coherent 899-21 Ring Laser by Coherent Inc.
[2] Verdi 18 by Coherent Inc.

Generally, the bandwidth of an etalon $\delta\nu_{etalon}$ is given by [34]

$$\delta\nu_{etalon} = \frac{c}{2L}\frac{1}{F}, \tag{4.1}$$

where L is the length of the etalon, c the speed of light and F the finesse of the etalon. The Titanium:Sapphire ring laser contains two low finesse etalons with two different lengths L and are therefore identified as a 'thin' and a 'thick' etalon that allow selectivity of the laser frequency within 10 MHz [33]. A 'tweeter' mirror and a galvo are used to finetune the cavity to the desired frequency.

In a ring laser system, running wave laser modes exist that propagate in both directions. This can lead to standing wave patterns in the gain medium which either lead to multimode lasing or deterioration of the laser beam profile. In order to achieve a laser mode running in a single direction, an optical diode is used. The optical diode acts as a Faraday rotator, and combined with a half-wave plate it leads to unidirectional transmission of the laser beam [33].

Single mode operation is achieved when the transmission maxima of all optical components, the mirrors, birefringent filter and both etalons overlap. In that case only a single mode will be amplified above the lasing threshold. A schematic view of these transmissions and the lasing threshold is shown in Figure 4.1.

The laser frequency needs to be locked to a specific frequency. To achieve this, the laser system has two active feedback systems. The first is a 'tweeter' mirror which compensates for fast cavity length variations, whereas a galvo provides long term stabilization [33]. Using an internal reference cavity and the two aformentioned active feedback components, the frequency fluctuations of the laser are below 500 kHz [33]. However, this does not provide an absolute frequency stability.

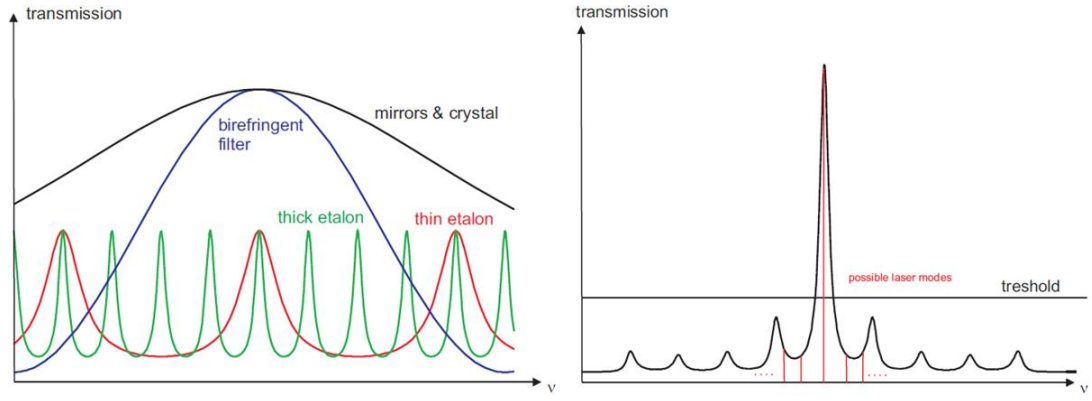

Figure 4.1: ***Left*** *A schematic view of the transmission versus frequency ν of all the different elements in the Titanium:Sapphire laser system. The mirrors, crystal and the birefringent filter all have broad transmissions to achieve large tunability of the laser frequency, but the 'thin' and 'thick' etalon are used for finetuning the laser frequency.* ***Right*** *If all the transmission peaks overlap, only a single laser mode will have enough power above the lasing threshold and the laser will achieve single mode lasing. This Figure has been adopted from [35].*

4.2 Frequency stabilization

Generally speaking, frequency stabilization of a laser occurs on short and long timescales. The short timescales roughly correspond to frequencies over 100 Hz and are associated with mechanical, acoustic and electronical noise, e.g., vibrations and noise due to vacuum pumps. On long timescales fluctuations in the environment of the laser, especially the temperature, play a role [36].

Although the laser system is specified to stabilize itself through an internal feedback system within 500 kHz, it does not provide an absolute reference to the desired frequency [33]. It is much more convenient to use an independent system to reference the laser frequency to.

In the introduction of this Chapter, we mentioned that the laser frequency should be stabilized a few MHz below the cooling transition. Therefore a logical step would be to reference the laser frequency to the actual transition itself using spectroscopy. However, we need to be slightly below this transition frequency. There are two possible methods to achieve the desired detuning of the laser. One method would be to lock the laser frequency to the actual transition frequency of the atomic reference and use two acousto-optical modulators (AOMs) to detune the laser frequency by 3 MHz before sending the laser beam to the 2D-MOT. Another option would be to use a magnetic field to induce a Zeeman shift of the transition frequency in our reference system and lock the laser to this frequency. In this work we will investigate the applicability of the latter method.

The implementation of this method will be explained in more detail in this Chapter, and we will discuss the different methods we use to perform spectroscopy on our atomic reference. But first we discuss how to design our electronic feedback system, which takes care of the actual stabilization of the laser frequency.

4.2.1 Feedback system

In order to create a feedback system to stabilize the laser frequency, an error signal is required [37, 38]. The error signal as function of the actual laser frequency ν, $\varepsilon(\nu)$, is zero exactly at the transition frequency and should be an odd function around the transition frequency ν_0 i.e. $\varepsilon(\nu_0) = 0$ and $\varepsilon(\nu_0 - \nu) = -\varepsilon(\nu_0 + \nu)$. Such an error signal, also called dispersion signal, is used as input for a PI controller. Using the error signal, the output V_{out} of a PI controller is [38]

$$V_{out} = P\Big[\varepsilon + I \int \varepsilon dt\Big], \tag{4.2}$$

where P is a proportionality constant and I the integrating constant. Values for these settings depend on the amplitude of and the slope of the signal. Essentially the PI controller tries to reduce the error signal to zero by sending a feedback signal to the laser. The feedback signal at the laser then drives the 'tweeter' mirror and the galvo in order to optimize the cavity transmission to the transition frequency. As the laser frequency gets closer to the transition frequency, the error signal approaches zero. A schematic view of a generic feedback system is shown in Figure 4.2.

The response of the feedback system depends on the specific shape of the error signal (i.e. peak-to-peak voltage and the slope of the signal at $\varepsilon(\nu_0)$) and the settings of the PI controller.

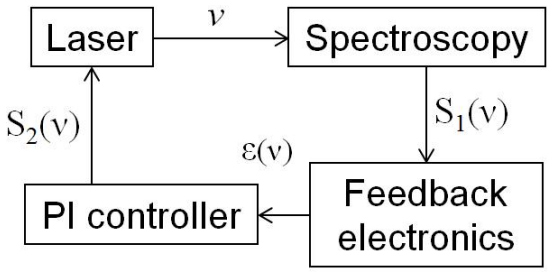

Figure 4.2: *Schematic view of a feedback system. From the spectroscopy setup, a signal S_1 is generated by a photodiode which is fed to the feedback electronics (e.g. modulation/demodulation electronics and noise filters). The electronics generate an error signal ε which, due to the spectroscopy, depends on the laser frequency ν. A PI controller then tries to converge the error signal to zero by sending a feedback signal S_2 to the laser system, where the frequency of the laser is adjusted.*

4.2.2 Spectroscopy methods

One of the most basic forms of spectroscopy is absorption spectroscopy [39]. A laser beam (also called the 'probe beam') propagates through a vapor cell containing the atomic species of interest and is then detected by a photodetector. As the laser frequency is scanned over an atomic transition frequency, the probe beam will experience different absorption during the scan. The photodetector will observe this absorption as a decrease in total intensity of the beam. This method is not very accurate as the observed absorption will appear much broader than the actual transition due to different broadening mechanisms, of which Doppler broadening (apparent broadening of the absorption due to the Maxwell-Boltzmann velocity distribution of the atoms) is the largest effect in common vapour cells [39]. As an example, the Doppler broadened width $\Delta\nu$ of the $5^2S_{1/2} \rightarrow 5^2P_{3/2}$ transitions of rubidium at room temperature can be calculated as $\Delta\nu = \nu_0\sqrt{8k_BT\ln(2)/mc^2} \approx 0.5$ GHz for the rubidium transitions considered in this report [25, 39]. As will be shown in Section 5, the rubidium transitions of both isotopes form four clusters in the frequency spectrum in which the transitions are within 0.5 GHz of each other. Therefore absorption spectroscopy cannot be used to isolate a single atomic transition frequency.

An extension of absorption spectroscopy is saturated absorption spectroscopy [25, 39]. In this case one uses two counterpropagating beams with unequal powers. The high power beam is called the pump beam and the low power beam is called the probe beam. As the beams counterpropagate, the frequencies are shifted for the atoms due to the Doppler shift $\Delta\omega = -\vec{k}\cdot\vec{v}$. At most atomic velocities, both laser beams will thus be detuned differently and will be absorbed at different rates. However, for atoms with $\vec{k}\cdot\vec{v} = 0$, both laser beams can be in resonance with the atomic transition simultaneously. In that case the strong pump beam depletes most of the ground state atoms and the weak probe beam will experience less absorption as it encounters less atoms in the ground state. This can be observed as a slight bump in the absorption spectrum, which occurs exactly at the resonance frequency [25, 39]. As the resonance frequency is situated exactly at the maximum of the peak, one would like to lock the laser frequency to the saturated absorption peak. As we mentioned earlier, for a good feedback signal one needs an asymmetric signal. The saturated

absorption peak is symmetric and other methods should be used to obtain an asymmetric signal from the saturated absorption peak. These methods are usually based on frequency modulation of the pump or probe beam [39].

There is another possible process involved with saturated absorption spectroscopy which will be relevant for our measurements. For a certain velocity v of an atom along both beams' axis of propagation, the Doppler shift in both beams can tune either beam in resonance with a transition to a different excited state. Hence the atom is able to absorb photons from either beam, but for different frequencies. We can write both resonance conditions as $\omega - kv = \omega_1$ and $\omega + kv = \omega_2$, where ω_1 and ω_2 are the transition frequencies to two different excited states. Both resonance conditions are satisfied when $v = (\omega_2 - \omega_1)/2k$, which gives $\omega = (\omega_1 + \omega_2)/2$. This transition falls exactly midway between to transitions and is therefore called the cross-over transition. The cross-over transition is a common feature when using saturated absorption spectroscopy [25, 39]. We will encounter this later as well.

Many spectroscopy methods used for frequency locking of lasers are based on modulation of the laser frequency to obtain a dispersive error signal [39]. This can either be done by modulating the laser cavity or by using an external modulator to modulate the frequency of the laser beam, such as an electro-optical modulator (EOM). Although EOMs can be expensive, they can modulate the laser frequency without modulating the cavity, making the laser more stabile. For this reason we have chosen to use an EOM to modulate the frequency of the laser beam.

Electro-optical modulation

There are two kinds of electro-optical modulators (EOMs): those which modulate the amplitude and those which modulate the phase of the electric field. We use the latter type. Essentially an EOM contains a crystal with an applied RF voltage which modulates the extraordinary index of refraction [40]. This modulation of the index of refraction causes a net modulation of the phase of the light. Considering a linear polarized electric field E oscillating at angular frequency ω_L (the angular frequency of the laser beam) and a harmonic phase modulation at an angular frequency ω_{FM} caused by the EOM, we have for an electric field after propagating through the crystal

$$E(t) = E_0 \sin\big(\omega_L t + \beta \sin(\omega_{FM} t)\big), \tag{4.3}$$

where β is the modulation index and is a measure of the strength of the interaction of the EOM with the laser beam. A harmonic modulation of the phase of a harmonic fuction can also be written as an infinite series of Bessel functions of the first kind $J_i(x)$ multiplied by each harmonic frequency of the phase modulation [41]

$$E(t) = E_0 J_0(\beta)\sin(\omega_L t) + E_0\Bigg[\sum_{n=1}^{\infty} J_n(\beta)\sin\big(\omega_L t + n\omega_{FM} t\big)... \\ + \sum_{n=1}^{\infty}(-1)^n J_n(\beta)\sin\big(\omega_L t - n\omega_{FM} t\big)\Bigg]. \tag{4.4}$$

In the frequency domain, we can understand this series as follows. The laser beam with central, or carrier, frequency ω_L is modulated by the EOM to obtain nth order sidebands at frequencies $\omega_{\pm n} = \omega_L \pm n\omega_{FM}$, where the amplitudes of the sidebands are determined by the order n and the modulation index β according to the Bessel function $J_n(\beta)$. The Bessel functions up to third order for small modulation index are shown in Table 4.1.

The modulation index β can be estimated by looking at the ratio of the intensities of the carrier frequency and the first sideband. In order to calculate the intensities of the sidebands, we use the fact that the intensity I is related to the electric field E as $I \propto \langle |E|^2 \rangle$. Using Table 4.1 and calculating the ratio of the first sideband intensity I_1 and the carrier intensity I_0, we have

$$\frac{I_1}{I_0} = \frac{\langle |E_1|^2 \rangle}{\langle |E_0'|^2 \rangle} = \left[\frac{J_1(\beta)}{J_0(\beta)}\right]^2 \approx \left[\frac{\frac{\beta}{2} - \frac{\beta^3}{16}}{1 - \frac{\beta^2}{4}}\right]^2 \approx \frac{\beta^2}{4} + O(\beta^4), \tag{4.5}$$

where we have defined $E_0' = J_0(\beta)E_0$ and $E_n = J_n(\beta)E_0$ for $n = 1, 2, 3, ...$ From this expansion we learn that the modulation index can be approximated as $\beta \approx 2\sqrt{I_1/I_0}$. We will use this approximation later to check the performance of the EOM.

Table 4.1: *The first four Bessel functions expanded for a modulation index* $\beta \ll 1$.

Order n	$J_n(\beta)$
0	$1 - \frac{\beta^2}{4} + O(\beta^4)$
1	$\frac{\beta}{2} - \frac{\beta^3}{16} + O(\beta^5)$
2	$\frac{\beta^2}{8} - \frac{\beta^4}{96} + O(\beta^6)$
3	$\frac{\beta^3}{48} - \frac{\beta^5}{768} + O(\beta^7)$

4.2.3 Using sidebands in spectroscopy

Using an EOM, we can create a laser beam existing of its carrier (laser) frequency and sideband frequencies. We can use this beam to perform spectroscopy at multiple frequencies simultaneously. In our setup we will use two methods: frequency modulation (FM) spectroscopy [42] and modulation transfer (MT) spectroscopy [41].

Frequency modulation spectroscopy

If a laser beam containing sidebands propagates through an atomic vapor for which it is close to an atomic transition frequency, the frequency components will each experience different absorption rates as they are at different frequencies with respect to the transition frequency. We will call the absorption coefficient $F(\omega) = |F(\omega)| \exp(i\phi(\omega))$, reflecting the fact that absorption can also alter the phase of the light through dispersion [37, 43]. For convenience we will describe the electric field using the complex notation

$$E = E_0 \left[J_0(\beta) e^{i\omega_L t} + J_1(\beta) e^{i(\omega_L + \omega_{FM})t} - J_1(\beta) e^{i(\omega_L - \omega_{FM})t} \right] \tag{4.6}$$

We have omitted any higher order sidebands for simplicity. The electric field of the partially absorbed beam can be described as

$$E_{abs} = E_0 \Bigg[J_0(\beta)|F(\omega_L)|e^{i\omega_L t + i\phi(\omega_L)} + J_1(\beta)|F(\omega_L+\omega_{FM})|e^{i(\omega_L+\omega_{FM})t+i\phi(\omega_L+\omega_{FM})} ... \\ -J_1(\beta)|F(\omega_L-\omega_{FM})|e^{i(\omega_L-\omega_{FM})t+i\phi(\omega_L-\omega_{FM})} \Bigg]. \quad (4.7)$$

But we can only detect the intensity of this beam with a photodetector, therefore we have to consider the square of the electric field $|E_{abs}|^2$. For simplicity and brevity, we will only consider the carrier frequency and the first sidebands in this calculation. As it is a straightforward calculation [37, 43], we will skip most of the steps and give the final result

$$I_{abs} \propto E_{abs}E_{abs}^{\star} = |E_{abs}|^2 \approx |E_0|^2 \Bigg[J_0^2(\beta)|F_0|^2 + J_1^2(\beta)\Big(|F_1|^2 + |F_{-1}|^2\Big) + ... \\ J_0(\beta)J_1(\beta)\Big(|F_0||F_1|\cos(\phi_1-\phi_0) - |F_0||F_{-1}|\cos(\phi_{-1}-\phi_0)\Big)\cos(\omega_{FM}t) + ... \\ J_0(\beta)J_1(\beta)\Big(|F_0||F_1|\sin(\phi_1-\phi_0) - |F_0||F_{-1}|\sin(\phi_{-1}-\phi_0)\Big)\sin(\omega_{FM}t)\Bigg]. \quad (4.8)$$

Here the superscript * denotes the complex conjugate and we have defined $F_n = F(\omega_L + n\omega_{FM})$ and $\phi_n = \phi(\omega_L + n\omega_{FM})$. Further we have omitted the explicit calculation of all terms oscillation at frequencies above ω_{FM} as we are currently not interested in them and we can filter these using appropriate electronics. This is a reasonable assumption as $\omega_L/2\pi \approx 100$ THz whereas $\omega_{FM}/2\pi \approx 10$ MHz in our experiments.

Assuming the difference in phase shifts is small, i.e. $|\phi_1 - \phi_0| \ll 1$ and $|\phi_{-1} - \phi_0| \ll 1$, and we are near resonance so $F_1 \approx F_{-1}$, we can rewrite Equation 4.8 as

$$I_{abs} \propto |E_0|^2 \Bigg[J_0^2(\beta)|F_0|^2 + J_1^2(\beta)\Big(|F_1|^2 + |F_{-1}|^2\Big) + J_0(\beta)J_1(\beta)|F_0|\Big(|F_1| - |F_{-1}|\Big)\cos(\omega_{FM}t) + ... \\ J_0(\beta)J_1(\beta)|F_0||F_1|\Big(\phi_1 - \phi_{-1} - 2\phi_0\Big)\sin(\omega_{FM}t)\Bigg]. \quad (4.9)$$

This shows us that the amplitude of the in-phase term $\cos(\omega_{FM}t)$ is proportional to the difference in absorption of the sidebands. The amplitude of the out-of-phase (or quadrature) term $\sin(\omega_{FM}t)$ is proportional to the difference in the acquired phases of the different frequency components and therefore is related to the dispersion of the different frequency components.

The in-phase amplitude is schematically shown in Figure 4.3. In this Figure we show a mock absorption line and the different absorption of the sidebands. Taking the amplitude of the in-phase (cosine) term of Equation 4.8, we effectively take the difference between both sideband intensities once they are being partially absorbed. This leads to a lineshape which is similar to the first derivative of the absorption line and provides an excellent error signal for the PI controller.

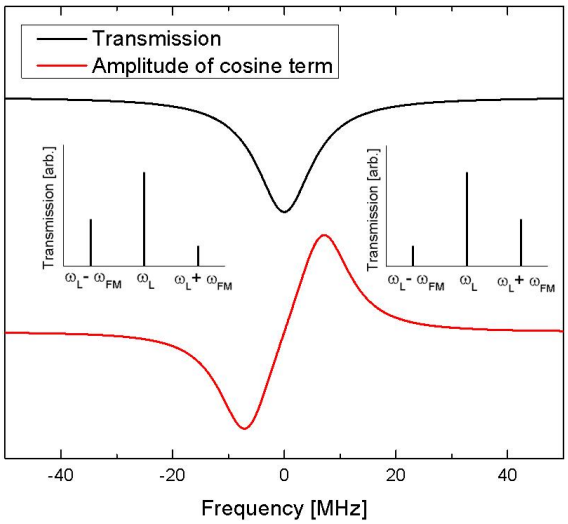

Figure 4.3: *Schematic interpretation of FM spectroscopy. Here we have a Lorentzian lineshape absorption dip with a linewidth of 6 MHz, which is the linewidth of our rubidium transition. The modulation frequency $\omega_{FM} = 6.8$ MHz, similar as used in our experiments. The amplitude of the in-phase (cosine) oscillations at the modulation frequency ω_{FM} of the intensity of the laser beam is proportional to the difference in absorption of the sidebands. The two insets schematically show the transmission of the two sidebands above and below the transition frequency. The zero crossing of this curve is at the actual transition frequency and can be used as an error signal for the PI controller.*

From this we intuitively learn something about the properties of FM spectroscopy. First, if the sideband separation is much larger than the linewidth of the transition (i.e., the linewidth of the absorption in Figure 4.3), one will find only absorption of either sideband and no dispersion signal as shown in Figure 4.3 [44]. Second, even if the sidebands are close enough, the observed dispersion signal is similar to the derivative of the absorption line but actually is a convolution of both sideband intensities with the absorption line. The actual linewidth of the absorption can only be determined by deconvoluting the dispersion signal with the spectrum of the laser beam.

It should be mentioned that a serious disadvantage of this method is its sensitivity to AC and DC Stark shifts of the electronic levels, as well as for Zeeman shifts [25, 39]. Hence it has limited use to lock at the absolute transition frequency. Therefore we also consider a second spectroscopy method: modulation transfer spectroscopy.

Modulation transfer spectroscopy

Modulation transfer (MT) spectroscopy is based on the same concept as FM spectroscopy: using an EOM to create sidebands in the laser beam to perform spectroscopy. The spectroscopy is performed using a saturated absorption setup i.e., a pump beam modulated by an EOM and an unmodulated probe beam counterpropagate collinearly through a vapour cell containing atomic rubidium [41, 45]. The physical processes involved, however, are quite different compared to FM spectroscopy. Through a nonlinear third order interaction, a fraction of the intensity of the

sidebands of the modulated pump beam is transferred to the probe beam and the initially single frequency probe beam acquires two sidebands [46, 47, 48]. This process is schematically shown in Figure 4.4. Two photons from the pump beam at frequencies ω_L and $\omega_L + \omega_{FM}$ (the sideband) combine in an atomic transition with a photon from the probe beam at frequency ω_L to form a sideband photon at frequency $\omega_L \pm \omega_{FM}$ which copropagates with the probe beam. Because four different photons (or similarly, waves) are involved, this process is also called four-wave mixing [47, 48].

As this process takes place for both sidebands, the probe beam also obtains both sidebands, but with much smaller intensities than the pump beam. Detecting the intensity of the probe beam with a photodetector then leads to a similar time-dependent behaviour as in the FM example in Equation 4.8 [41]. By looking at the amplitude of either the in-phase (cosine) or out-of-phase (sine) signals beating with frequency ω_{FM}, again a similar dispersion lineshape can be detected as for FM spectroscopy [41].

However, there are some significant differences between FM and MT spectroscopy. First, as MT spectroscopy is based on a nonlinear process, the four-wave mixing only takes place very close to or at the atomic resonance and therefore has a much smaller background signal than for FM spectroscopy. FM spectroscopy is based on saturated absorption and therefore still experiences the Doppler broadened background, as discussed in Section 4.2.2. Second, MT spectroscopy produces the largest signals for closed transitions [41] which makes it easier to lock the laser to the cooling transition (which, by definition, is a closed transition). Closed transitions are the hyperfine transitions $F \to F' = F + 1$, where F' is the largest hyperfine level of the spectroscopic state. As an example, for the ^{85}Rb $5^2S_{1/2}$ $F \to 5^2P_{3/2}$ F' transitions (as discussed in Section 2.1.1), this is the $F = 3 \to F' = 4$ transition.

In FM spectroscopy all transitions have approximately the same amplitude. Cross-over transitions (discussed in Section 4.2.2), which are severely suppressed in MT spectroscopy, also dominate the FM spectrum [41]. Finally, McCarron *et al.* claim that the zero crossing of the dispersion signal obtained using MT spectroscopy does not shift due to a magnetic field (i.e. the Zeeman shift) [41]. In our measurements, which we will discuss later, we do see a change in the lineshape due to an applied magnetic field, but no clear frequency shift can be observed. We conclude that

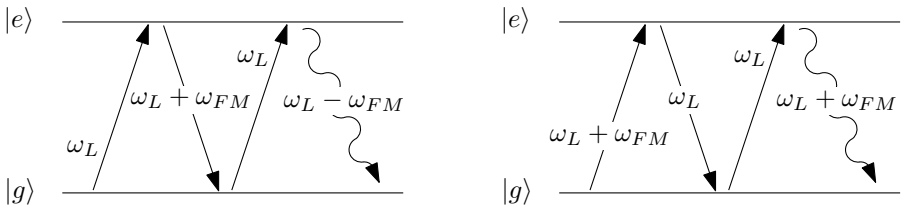

Figure 4.4: *Schematic representation of four-wave mixing [47, 48] in a two-level atom with ground state $|g\rangle$ and excited state $|e\rangle$. Through a resonant interaction between a sideband photon $\omega_L + \omega_{FM}$ of the pump beam, a pump carrier photon ω_L and a probe carrier photon ω_L, either sideband photon $\omega_L \pm \omega_{FM}$ can be generated in the probe beam. This process is identical for the other sideband of the pump beam [47].*

MT spectroscopy is less sensitive to magnetic perturbations (such as the Earth's magnetic field) than FM spectroscopy and therefore a more suitable reference to the absolute atomic transition frequency. In order to investigate the possibility of detuning the laser frequency using the Zeeman shift, we will have to use FM spectroscopy later in this report.

4.3 Proposed design for frequency stabilization

Now that we have shown the different methodsto stabilize the laser frequency, we discuss the design of the actual setup in the laboratory. We want to be able to employ both FM and MT spectroscopy in order to be able to lock the laser to the absolute transition frequency (with MT) or lock the laser to a Zeeman-shifted transition (with FM). This means that we require a spectroscopy setup where both methods are applicable.

Another aspect of this project, which has been briefly mentioned in Chapter 2, is to try to construct the setup in such a way that most of the optical paths actually go through optical fibers. This makes it easier to design a more flexible and compact future design, and it creates a more modular (independent) design of the whole setup. In this way we would like to prevent alignment problems and reduce beam pointing instabilities due to e.g. different vibrations in the optical setup and the 2D-MOT. For this purpose we use several different fiber components to e.g. couple the light in the fiber, distribute the light over different beams and collimate the beam outside of the fiber. Fiber optics offers a lot of possibilities and there is a broad spectrum of available components[3]. However, most components are designed for the optical telecommunication industry and are therefore only available for wavelengths of 1300-1500 nm, almost twice as long as the wavelength we are working with. There are also many components available which are designed for 780 nm light, but at a higher cost. Therefore we currently use fibers only to transport and distribute the light in our setup, and construct the spectroscopy setup using conventional 'free space' optics.

Figure 4.5 is a schematic display of our final setup, and Figure 4.6 shows the spectroscopy part in more detail. This setup is a combination of a FM spectroscopy setup based on [42] and an MT spectroscopy setup based on [17, 41]. The laser beam first goes through an optical isolator to prevent any destabilizing feedback through reflections. A half-wave plate and a polarizing beam splitter (PBS) are used to control the total power which goes into the fiber. Coupling the light into the fiber is done using four components: two mirrors to steer the laser beam, a 3D translation stage on which we can optimize the position of the fiber and the microscope objective[4] which is used to focus the light into the fiber. We use a 2x2 fiber coupler[5] to take 10% of the light to the spectroscopy setup and keep the other 90% for other purposes (which in the end should go to the experiment).

The spectroscopy setup is based on a typical ring setup common for saturated absorption spectroscopy as for instance described in [39], and more directly on the setups described in [17, 41]. The distribution of the intensity over both pump and probe beams is controlled by a half-wave

[3]See, for instance, the Thorlabs catalog from which we have ordered most products.
[4]Thorlabs RMS20X Plan Achromat microscope objective.
[5]Thorlabs FC780-90B-APC 2x2 Single Mode Coupler with a 90:10 split ratio.

plate and a PBS. A rubidium vapour cell[6] contained in a copper wire coil (to apply an external magnetic field if desired) is placed in one arm, and the EOM[7] is placed in the other arm. The EOM is driven by a frequency generator[8] and an LC ciruit. In order to optimize the spectroscopy signal, a large beam diameter is chosen of approximately 4 mm using a fiber collimator[9]. As the entrance and exit of the EOM are only 1 mm in diameter, two plano-convex lenses with $f = 200$ mm are used to focus the light into the EOM and collimate the beam after the exit. For a beam radius of 2 mm and a lens with a focal length of 200 mm, the far field divergence is approximately $\theta \approx 2/200 = 10$ mrad. Using the fact that $\theta \approx \lambda/\pi w_0$ [34] and $\lambda \approx 780$ nm, we find a beam waist of $w_0 \approx 25$ μm. This limits the maximum power we can put through the EOM (which has a damage threshold of 3 W/mm^2 [40]) to approximately 6 mW. We use two non-polarizing beam splitters to either observe the FM or MT spectroscopy signal with two photodetectors[10]. Finally we have the possibility of inserting two quarter-wave plates immediately in front and behind the rubidium vapour cell in order to create circularly polarized light, which is required when Zeeman-shifting the transitions.

4.4 Feedback electronics

In our discussion of the different spectroscopy methods, we have not yet mentioned how the signals as detected by the photodiodes are actually processed to generate the dispersion signal (also known as the aforementioned error signal). In order to determine the amplitude of the in-phase or out-of-phase signals of the intensity oscillations, we electronically multiply the photodiode signal by a harmonic signal, from the same frequency generator which drives the EOM, oscillating at ω_{FM}: $\cos(\omega_{FM}t + \phi)$, where ϕ is a phase-shift which can be adjusted in the lab to either pick the in-phase ($\phi = n\pi$, $n = 0, 1, 2...$) signal, out-of-phase ($\phi = (n + 1/4)\pi$, $n = 0, 1, 2...$) signal or a superposition of both. This electronic multiplication will lead to a DC signal which is a function of the laser frequency i.e. the dispersion (error) signal as shown in Figure 4.3. A block diagram of the electronics is shown in Figure 4.7. There will also be terms oscillating at $2\omega_{FM}$ or higher frequencies, but these are easily omitted using a low-pass filter. Although it is originally based on [41], a similar detection unit has been built in the lab before [17]. As the existing detection unit has shown no problems so far, our electronics unit is an exact copy where the only difference is the oscillation frequency (ours runs at 6.8 MHz instead of 8.0 MHz).

[6] Toptica CE RB 50 Optical quality rubidium vapour cell.
[7] Thorlabs EO-PM-NR-C1 Broadband Electro-optic Phase Modulator, 600-900 nm.
[8] Hewlett-Packard 33120A 15 MHz Function/Arbitrary Waveform Generator.
[9] Thorlabs CFS18-850-APC Pigtailed aspheric collimator.
[10] Thorlabs DET10A/M High speed Si detector.

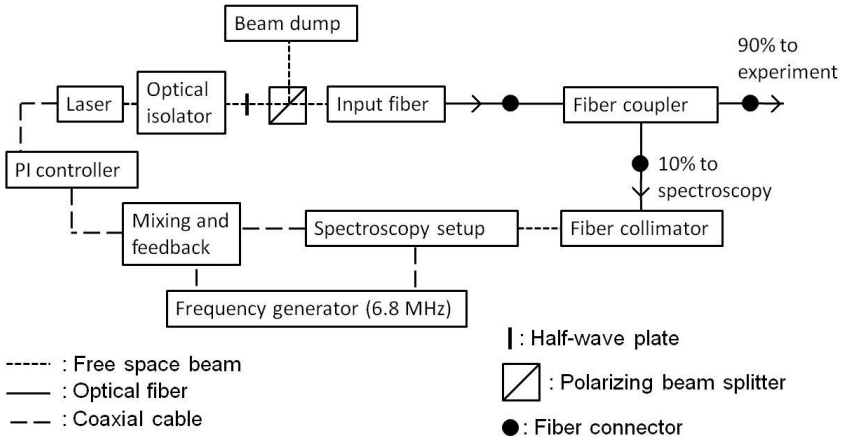

Figure 4.5: *Block diagram of our setup. We use an optical isolator to reduce reflected light going into the laser. A half-wave plate and polarizing beam splitter are used to control the input power into the fiber. The fiber input exists out of two mirrors, a microscope objective and a 3D translation stage. We use one input of a 2x2 fiber coupler to distribute the light;* 10% *to spectroscopy and* 90% *to (eventually) the experiment. From the spectroscopy we then obtain an electric signal which is demodulated by the feedback electronics and through a PI controller produces a feedback signal to the laser.*

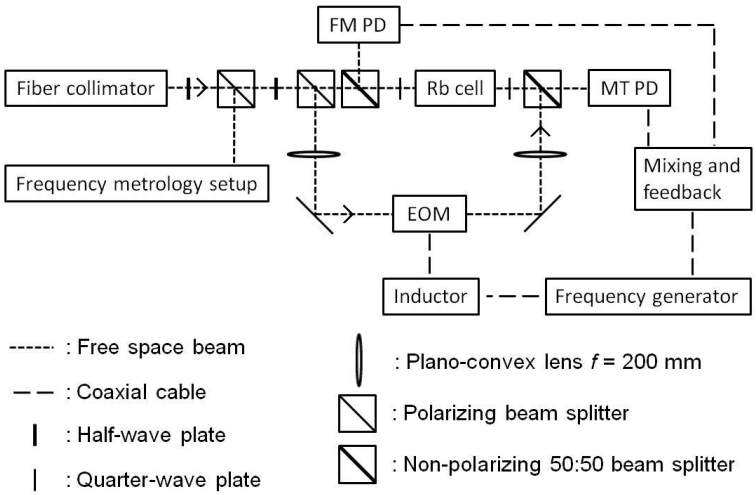

Figure 4.6: *Schematic diagram of our spectroscopy setup. The fiber collimator produces a laser beam with a* $1/e^2$ *diameter of* 4 mm*. We first use a half-wave plate - polarizing beam splitter pair to split off some light for future frequency metrology. Then we use another half-wave plate - polarizing beam splitter pair to control the ratio of the intensities over both paths in the saturated absorption ring. We slightly misalign the mirrors so the laser beam only propagates in the counterclockwise direction through the EOM. The rubidium vapour cell is placed inside a copper wire coil and the quarter-wave plates are only inserted when doing Zeeman-shift experiments. Photodetectors MT PD and FM PD are used for performing the MT spectroscopy or FM spectroscopy, respectively.*

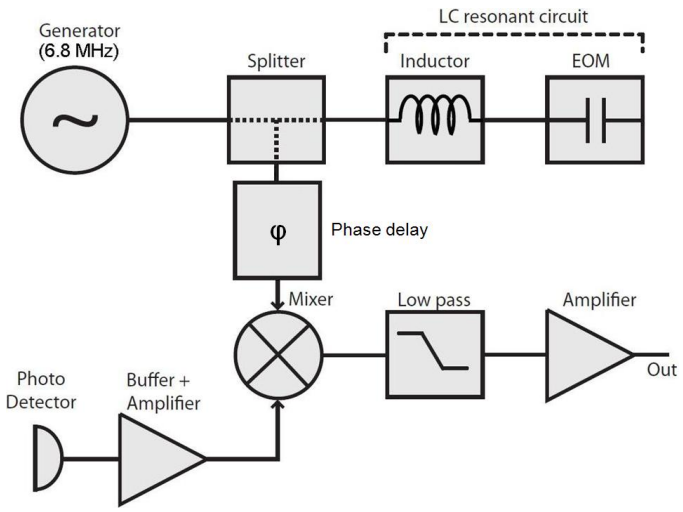

Figure 4.7: *Diagram of the electronics used for demodulating the FM spectroscopy and MT spectroscopy signals. Half of the power of a frequency generator drives the EOM through an LC resonance circuit and the other half is used for the demodulation of the photodetector signal. After mixing a low pass filter is used to only obtain the DC signal. The coaxial cable length between the splitter and the mixer can be varied to change the detection phase ϕ. This diagram is mainly based on [17].*

4.5 Electro-optical modulator

The essential component for either FM or MT spectroscopy is the generation of sidebands using an electro-optical modulator, or EOM. In order to operate the EOM, a voltage of approximately 100 Volts needs to be applied [40]. In order to obtain this voltage we use a resonant LC circuit to drive the EOM. As the EOM already has an input capacitance, we only need to place a coil with inductance L in series with the EOM as shown in Figure 4.7. The resonance frequency ν_{res} of a LC circuit is $\nu_{res} = 1/2\pi\sqrt{LC}$ [49], and the voltage at the EOM will be greatly enhanced near or at this resonance frequency. In order to create sidebands at the required frequency $\omega_{FM} = 2\pi\nu_{FM}$, the EOM should work optimal at the same frequency. This means that $\nu_{FM} = \nu_{res}$ for optimal performance of the EOM.

4.5.1 Resonance of the LC circuit

The MT spectroscopy setup in the lab as described in [17] performs well at a modulation frequency of 8 MHz and a frequency generator peak-to-peak voltage of 9 V. Therefore we would also like to work with those parameters. Using the aforementioned resonance frequency and the given input capacitance of the EOM $C = 11.8$ pF [50], we find a required inductance of $L = 33.5$ μH. The inductance is produced by a coil which is handmade in the electronics workshop, and due to imperfections we do not expect it to have the exact specified inductance. Therefore we connect the coil to the EOM and measure the voltage buildup between the coil and the EOM using an

oscilloscope[11]. This is schematically shown in Figure 4.8.

By scanning the frequency and measuring the voltage using the scope, we can find the resonance. However, we are only able to measure the voltage with a 100 : 1 reduction of the amplitude. This is because we have neglected several effects in our simplified electronical diagram. First, the electronic signals are carried by coaxial cables[12], which also have a capacitance. Second, our oscilloscope has an input resistance of 1 MΩ and a parallel capacitance of approximately 13 pF (as specified on the oscilloscope). The input resistance is of little importance but the input capacitance together with the 10 kΩ resistor forms a RC filter which attenuates signals for frequencies over $\nu_{RC} = 1/2\pi RC \approx 1.2$ MHz [49].

To calculate the effect of the attenuation due to this RC filter effect, we use an electronic circuit simulation software kit called PSpice [52]. The full electronic diagram is shown in Figure 4.9. Apart from the experimental error in the capacitances and resistors, our only degree of freedom is the inductance L of the coil. In an iterative method, we try different values of L and simulate the frequency response of this circuit using PSpice. We assume that the best agreement between the simulated and the measured response then also gives the best approximation for the inductance of the coil. The comparison between the simulated and measured resonance is shown in Figure 4.10, and gives an inductance of $L = (25.0 \pm 0.5)$ μH. Further, we note that the resonance frequency is $\nu_{res} \approx 6.8$ MHz. If we remove the scope and the connecting coaxial cable (C_2 in Figure 4.9) in our simulation model and repeat the simulation, we find the resonance still to be at the same frequency. This makes sense as the removal of the scope only removes the RC filter and does not affect the LC resonance.

Having measured the resonance frequency, we can now take a look at the sidebands generated by the EOM.

4.5.2 Measuring the sidebands created by the EOM

A common method to measure the spectrum of a laser beam is by generating a beatnote with a reference laser beam. The general idea is as follows: consider two oscillating electric fields which have equal polarization and spatially overlap. The sum of both electric fields $E_1(t)$ and $E_2(t)$ would be $E(t) = E_1(t) + E_2(t) = E_1 \sin(\omega_1 t) + E_2 \sin(\omega_2 t)$. If the combined fields are incident on a photodetector, the resulting intensity will oscillate and contain both the sum and difference frequencies of the two fields:

$$I(t) \propto E(t)E^{\star}(t) = \frac{1}{2}(E_1^2 + E_2^2) + E_1 E_2 \cos((\omega_1 - \omega_2)t) + \ (2\omega \ terms). \tag{4.10}$$

In this simple calculating we ignore any relative phase difference between the two electric fields, as this does not affect the resulting oscillation frequency. If $\omega_1 \approx \omega_2$, we see that the intensity has a slowly varying modulation whose amplitude is linear with the amplitudes of the electric fields and oscillates with the difference frequency of the two electric fields. We omit the sum terms as we are dealing with optical fields, and whereas $(\omega_1 - \omega_2)/2\pi \approx 100$'s of MHz, the intensity contributions oscillating at the sum frequencies are 100's of THz and will average to zero when looking at the

[11] Rigol DS 5062CA.

[12] Of which the capacitance is approximately 100 pF per meter cable [51].

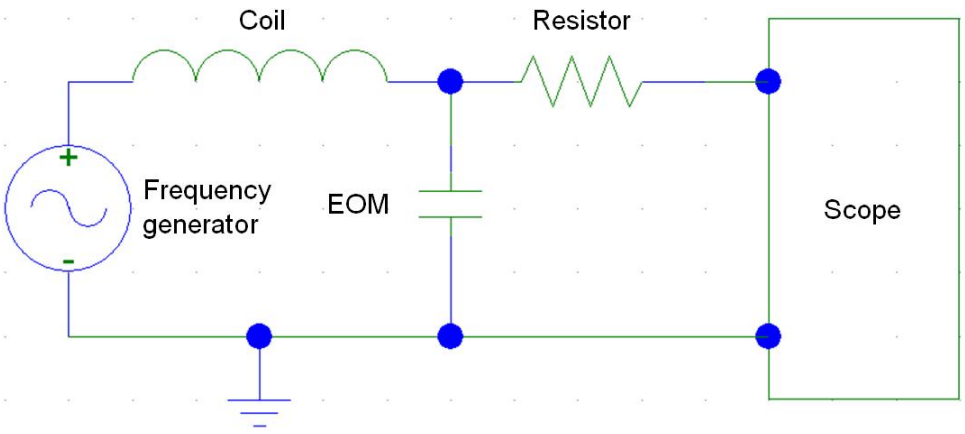

Figure 4.8: *Schematic diagram of our LC resonance measurement setup. The frequency generator drives the LC circuit, and we connect a scope (through a resistor of* 10 kΩ*) to measure the voltage across the EOM. This diagram is drawn using PSpice.*

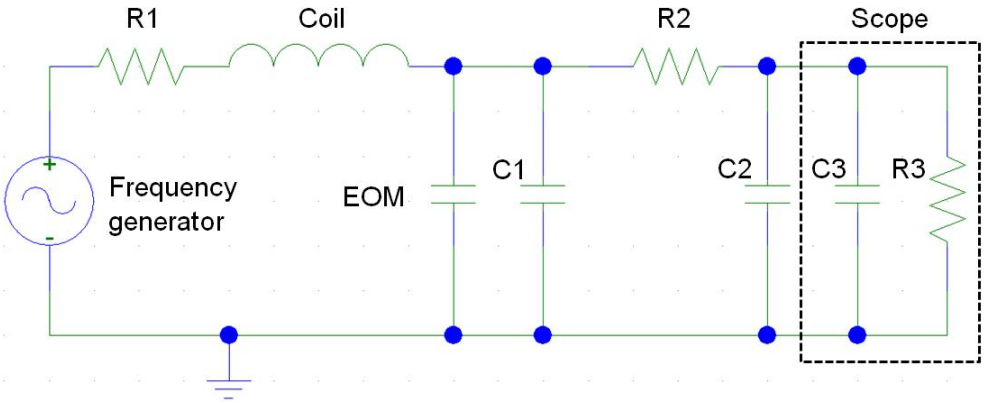

Figure 4.9: *Full electronic diagram of our LC resonance measurement setup. Capacitors $C1$ and $C2$ represent the coaxial cables and have approximate capacitances of 9.7 pF and 90 pF, based on their respective lengths. The resistance $R1 = 50\ \Omega$ is the output resistance of the frequency generator and $R2 = 10$ kΩ is a safety resistance between the LC circuit and the scope to prevent drawing large currents when accidently short-circuiting the system. The scope has input capacitance $C3 = 13$ pF and input resistance $R3 = 1$ MΩ. This diagram is drawn using PSpice.*

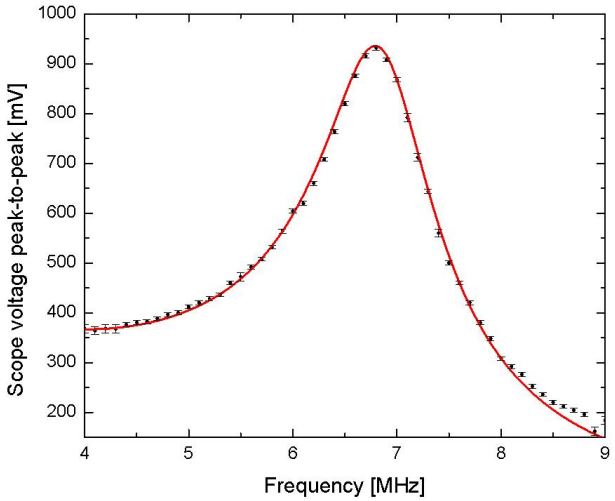

Figure 4.10: *Comparison between the resonance of the LC circuit as measured (dots) using the scope, and the PSpice simulation (line) based on the electrical diagram of Figure 4.9. The inductance of the coil used in this simulation is $L = 25.0\ \mu H$ but we add a $\pm 0.5\ \mu H$ error margin on this value, approximated from the sensitivity of the simulated curve to the value of L. The resonance frequency is $\nu_{res} \approx 6.8\ MHz$.*

intensity contribution oscillating at the difference frequency. Generating a beatnote thus enables one to observe the difference in frequencies of two oscillating electric fields.

To obtain useful information from the beatnote, we need a reference frequency. For this we could take the second output of the 2x2 fiber coupler, but generating a beatnote from this beam with the EOM beam will create a difference frequency of 0 Hz for the carrier frequency (i.e., the laser frequency itself). It is not possible to distinguish between the resulting negative and positive frequency components of the spectrum we are interested in, as the negative frequency components will add to the positive frequency components. Therefore we detune the frequency of the reference laser beam with an AOM[13] connected to an RF amplifier oscillating at 150 MHz and taking the first order diffracted beam. We spatially overlap this beam with the beam from the EOM and observe the intensity with a fast photodetector[14]. The photodetector is connected to a spectrum analyzer[15].

For our current operating settings of the frequency generator, 6.8 MHz and 9 V peak-to-peak, the resulting beatnote spectrum is shown in Figure 4.11. It clearly shows the carrier offset frequency at 150 MHz, and the equally spaced (up to third order!) sidebands. The peaks are extremely narrow as we are producing a beatnote using the same source for both components. Without making an effort to temporally delay either one of the beams, the fields are fully coherent and therefore the spectrum is extremely narrow. We also see some background noise on the spectrum in Figure 4.11. The noise source at 150 MHz is caused by the RF amplifier which drives the AOM. All other sources are unknown, but can be separated from the spectrum of the probe

[13]ISOMET Acousto-Optical Modulator 1212-2-949.
[14]Thorlabs DET210 High-Speed Silicon Detector.
[15]Rohde&Schwarz ZVH8 Cable and Antenna Analyzer.

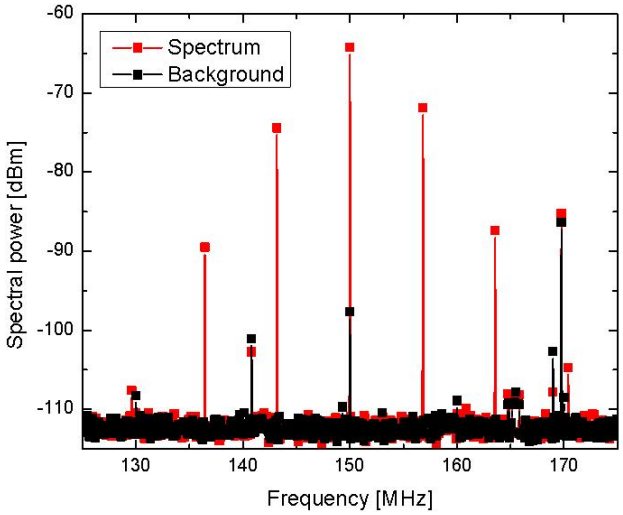

Figure 4.11: *Measured beatnote spectrum of the EOM modulated beam and the* 150 *MHz detuned beam. The frequency generator is set to* 6.8 *MHz and* 9 *V peak-to-peak. A background measurement (both beams blocked) is shown to indicate background noise sources. The low noise at* 150 *MHz, for instance, is due to the RF amplifier which drives the AOM and stands near the setup. However, we can see the carrier at* 150 *MHz, a sideband spacing of 6.8 MHz and up to third order sidebands at* 129.6 *MHz and* 170.4 *MHz.*

beam.

In Section 4.2.2 we discussed a method to determine the modulation index β from the spectrum: $\beta \approx 2\sqrt{I_1/I_0}$, where I_1 and I_0 are the intensities (or in this case, powers) of the first sideband and the carrier, respectively. By determining the modulation index for different settings of the frequency generator driving the EOM, we can determine the optimal frequency and voltage to drive the EOM. Essentially we try to answer the same question as posed in Section 4.5.1, but we now use a completely different method.

Figure 4.12 shows the modulation index β measured by scanning the frequency generator peak-to-peak voltage and keeping the frequency set to 6.8 MHz. We cannot exceed 9 V, as this would exceed the damage threshold of the feedback electronics. The modulation index increases linearly with the voltage; this shows that the modulation index increases linearly with the electric field applied inside the EOM. This validates the linear expansion of the electric fields in Section 4.2.2 used to calculate the EOM spectrum.

Figure 4.13 shows the modulation index determined for different frequencies, but at a frequency generator amplitude of 9 V peak-to-peak. Comparing this to the resonance as simulated using PSpice (also discussed in Section 4.5.1) we see that both resonances occur at the same frequency, which makes sense.

In our calculation of the sidebands in Section 4.2.2, we found that the intensities of the nth order sidebands should go as

$$\frac{I_n}{I_0} = \left[\frac{J_n(\beta)}{J_0(\beta)}\right]^2, \tag{4.11}$$

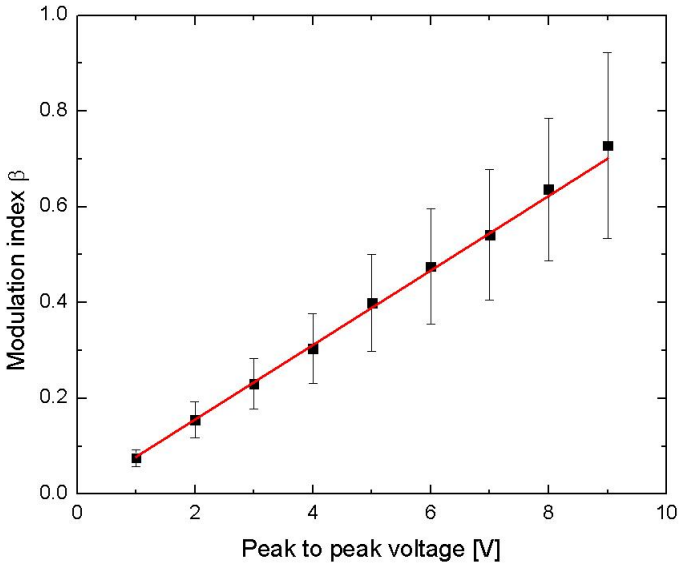

Figure 4.12: *Modulation index β measured for different frequency generator peak-to-peak voltages, but at a constant frequency of 6.8 MHz. The error bars are an estimate of the systematic error due to the difference in power in the $n = +1$ and $n = -1$ sidebands. The red line is a linear fit with slope $(7.79 \pm 0.06) \cdot 10^{-2}$ V^{-1}. The intercept is fixed at the origin.*

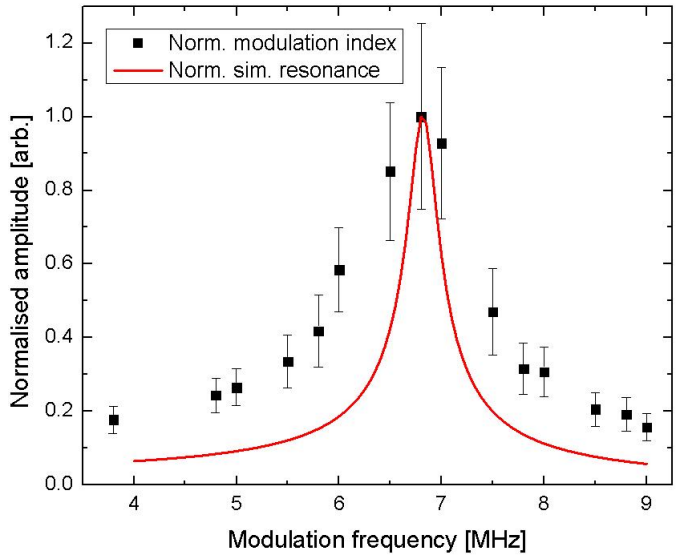

Figure 4.13: *Modulation index β (squares) measured for different frequencies, but at a constant peak-to-peak voltage of 9 V. The error bars are an estimate due to the difference in power in the $n = +1$ and $n = -1$ sidebands. Both the PSpice simulated resonance curve (full line) and the determined modulation index are shown (normalised to their respective maxima) to show that both from the optical and electronic model we obtain the same resonance at 6.8 MHz.*

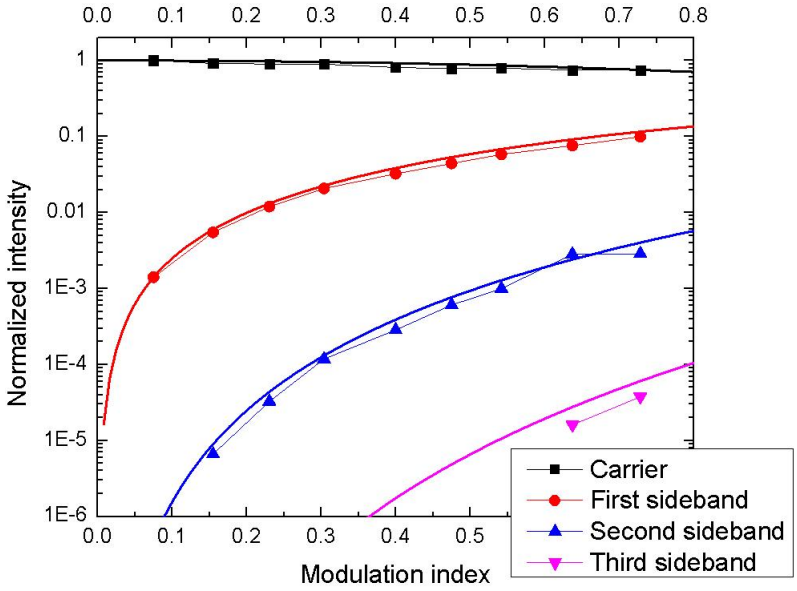

Figure 4.14: *Side- and carrierband intensities normalized to the carrier intensity for the smallest value of β. The error bars on the normalized intensities are smaller than the squares. The full lines are the nth order Bessel functions squared: $J_n^2(\beta)$. We find excellent agreement between the perturbation calculation of the sidebands and the actual performance of the EOM.*

where $J_n(\beta)$ is the nth order Bessel function as function of the modulation index β. As $J_0(\beta \to 0) = 1$ (see Table 4.1), normalizing each sideband intensity with the carrier intensity in the absence of modulation, should give us the square of the Bessel function for each sideband as function of the modulation index. This is shown in Figure 4.14. The full lines are the nth order Bessel functions squared for each nth sideband. The excellent agreement between the Bessel functions and the intensities shows that the linear expansino using the Bessel functions quite accurately models the EOM performance.

4.5.3 Conclusion on the performance of the EOM

In order to perform FM or MT spectroscopy, sideband generation is a basic necessity. Here we implement an EOM driven in a LC circuit by a frequency generator. We determine the resonance frequency of the LC circuit to be 6.8 MHz by measuring the resonance using a scope.

We also look at the spectrum of the laser beam after passing through the EOM. By varying the modulation frequency and looking at the intensities of the sidebands generated, we find the optimal sideband generation to be at a modulation frequency of 6.8 MHz, in agreement with the measurement of the LC resonance. Further, by determining the modulation index β for different frequency generator peak-to-peak voltages, we have found a linear relationship between the applied voltage and the modulation index. Further, we find excellent agreement between the normalized nth sideband and the exact nth order Bessel function, indicating that the modulation efficiency of the EOM agrees with the model.

4.6 Creating a magnetic field

In order to Zeeman-shift the energy states of the rubidium atoms, a copper wire coil is constructed to produce the required magnetic field. As discussed in Appendix B, the Zeeman-shift of the rubidium cooling transition is approximately 1.4 MHz/G. As the linewidth of the transition is approximately 6 MHz, we would need a maximum magnetic field of 10 G to have a sufficiently large tuning range of Zeeman-shifted frequencies (10 G $\sim$ 14 MHz $\sim$ two linewidths).

The constructed coil has 54 turns of copper wire over 60 mm, giving it an average number of $n = 900$ turns per meter. The coil is connected to a current source[16]. A magnetic field probe[17] is used to measure the axial magnetic field and the field perpendicular to the optical table on which the coil is mounted. The perpendicular field has a magnitude $B_{perp} = (1.2 \pm 0.3)$ G. The axial field is measured for different currents. The result is shown in Figure 4.15 and shows an excellent linear relationship between the magnetic field and the current: $B_{axial} = -(0.21 \pm 0.03) + (8.24 \pm 0.02)I$. The offset term indicates there will be some residual magnetic field along the axial direction. The second term is the slope $\partial B/\partial I$ and is lower than the expected slope $\partial B/\partial I = \mu_0 n = 11.3$ G/A from the ideal coil model, where the axial magnetic field B of an ideal coil is $B = \mu_0 nI$ and $\mu_0 = 4\pi \cdot 10^{-7}$ H m^{-1} is the magnetic permeability and I the applied current [53]. We will use the measured slope to convert the applied coil current to a magnetic field.

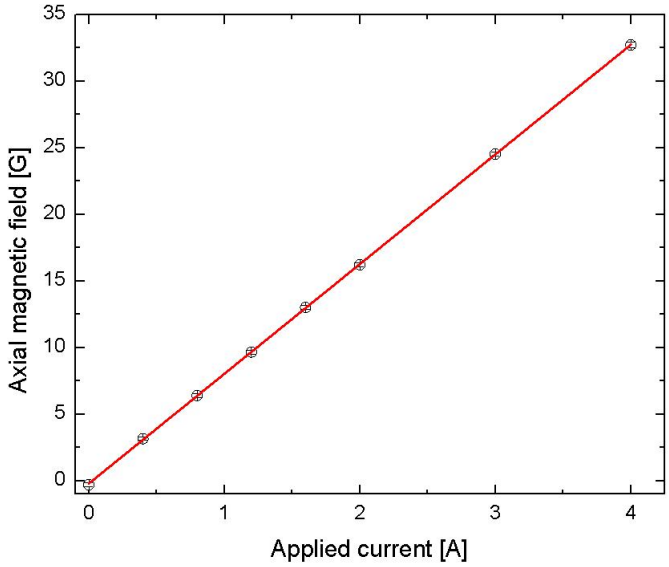

Figure 4.15: *Axial magnetic field of the coil for different applied currents. The straight line is a fit with zero crossing* $-(0.21 \pm 0.03)$ *G and a slope of* (8.24 ± 0.02) *G/A.*

[16] Delta Elektronika ES 030-5 Power Supply.
[17] Hirst Magnetic Instruments GM04 Gaussmeter.

Chapter 5

Spectroscopy and stability

Now we have the electronics and optics working, we can perform spectroscopy. First we want to perform spectroscopy on rubidium in order to obtain the dispersion signals to lock the laser frequency to. After that we use the Zeeman shift to detune the laser frequency. Finally we will also look at the frequency stability of the locked laser frequency.

Although we have shown in Chapter 3 that using an atomic beam of pure ^{87}Rb provides the highest brightness, our future experiments on the ABLIS will start by using a natural mixture of rubidium as a purified source is much more expensive. Using a natural mixture, it does not matter much which isotope one will cool and compress to obtain the highest brightness (as shown at the end of Chapter 3). Further, once we have shown that the locking and detuning works, it is a trivial matter to lock and detune the frequency to either of the transitions required to cool and compress either isotope. Therefore we currently choose the ^{85}Rb cooling transition, which is the $5^2S_{1/2}$ $(F = 3) \rightarrow 5^2P_{3/2}$ $(F = 4)$ transition to lock our laser frequency to. In the rest of this report we will refer to this transition as the (^{85}Rb) cooling transition.

As can be seen in the rubidium level schemes as introduced in Section 2.1.1, and shown in in Appendix B, there are several transitions which are close (that is, within a few GHz) to the cooling transition. The difference in transition frequencies with respect to the cooling transition are shown in Table 5.1. As shown in Section 4.2.2, the Doppler broadening of these transitions at room temperature is about 0.5 GHz. Including this broadening, we find that all 12 transitions in Table 5.1 will effectively be observed in four clusters if we only use absorption spectroscopy. The full absorption spectrum is shown in Figure 5.1. This spectrum is measured using the MT PD in the setup as shown in Figure 4.6, but blocking the counterpropagating beam which goes through the EOM. Four absorption dips are visible, each representing a cluster of the aforementioned transitions. The outermost left and right hand absorption dips are the ^{87}Rb transitions. They absorb less light as the rubidium vapour cell contains a natural mixture of both rubidium isotopes, which is about ^{87}Rb:^{85}Rb $\approx$ 1:3 [21]. This spectrum could contain more detail if we were to perform saturated absorption spectroscopy [25, 39], but we will skip this technique and continue to the more accurate FM and MT spectroscopy (as some characteristic properties of saturated absorption spectroscopy will also appear in either of these techniques).

Table 5.1: *Frequency differences of the $5^2S_{1/2}$ $F \rightarrow 5^2P_{3/2}$ F' transitions of ^{85}Rb and ^{87}Rb with respect to the ^{85}Rb $F = 3 \rightarrow F = 4$ cooling transition. Including a Doppler broadening of 0.5 GHz for each transition at room temperature, the 12 transitions can only be resolved into four clusters, shown by the divisions in the Table. The frequencies are calculated using the rubidium level data from [22, 23].*

Isotope	Transition	Frequency difference [GHz]
^{85}Rb	$F = 3 \rightarrow F = 4$	0
^{85}Rb	$F = 3 \rightarrow F = 3$	-0.121
^{85}Rb	$F = 3 \rightarrow F = 2$	-0.184
^{85}Rb	$F = 2 \rightarrow F = 3$	+2.92
^{85}Rb	$F = 2 \rightarrow F = 2$	+2.85
^{85}Rb	$F = 2 \rightarrow F = 1$	+2.82
^{87}Rb	$F = 2 \rightarrow F = 3$	-1.20
^{87}Rb	$F = 2 \rightarrow F = 2$	-1.47
^{87}Rb	$F = 2 \rightarrow F = 1$	-1.63
^{87}Rb	$F = 1 \rightarrow F = 2$	+5.36
^{87}Rb	$F = 1 \rightarrow F = 1$	+5.21
^{87}Rb	$F = 1 \rightarrow F = 0$	+5.13

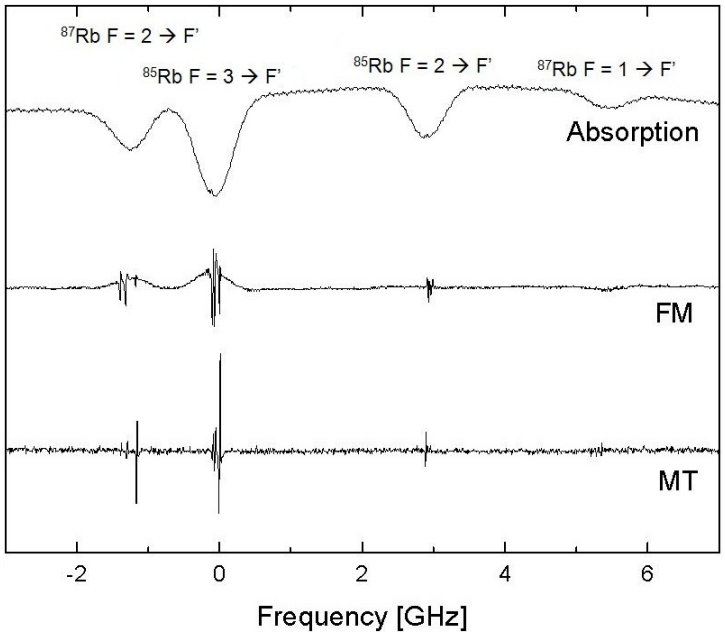

Figure 5.1: *Comparison of the signals of the three different spectroscopy methods by scanning the laser frequency over the $5^2S_{1/2}$ $F \rightarrow 5^2P_{3/2}$ F' transitions of rubidium. The frequency axis is calculated from the scope time axis using the laser scan rate of 43.21 GHz/s and the origin is chosen at the center of the ^{85}Rb cooling transition.*

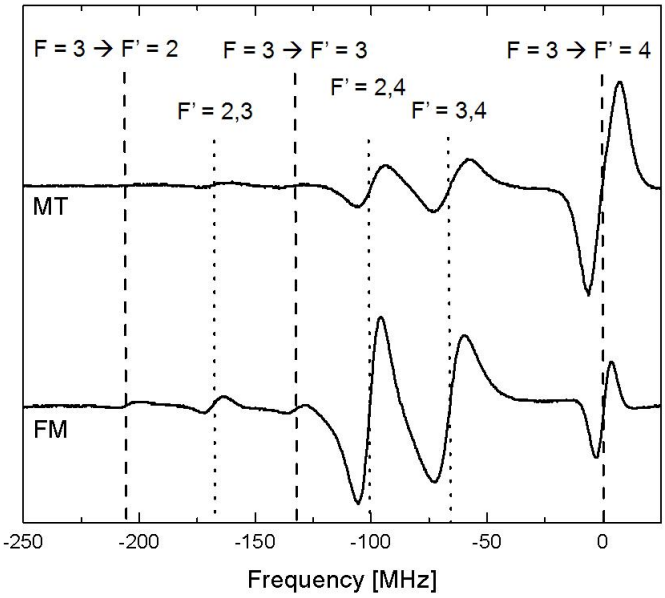

Figure 5.2: *Comparison of MT and FM dispersion signals by scanning the laser frequency over the* ^{85}Rb $5^2S_{1/2}$ $(F = 3) \rightarrow 5^2P_{3/2}$ F' *transitions. The transitions marked* $F' = i, j$ *are cross-over transitions, as discussed in the text. The frequency axis is calculated from the scope time axis using the laser scan rate of* 1.18 *GHz/s and its zero is defined at the cooling transition.*

5.1 MT spectroscopy

The MT spectroscopy signal is obtained using the MT PD in the full setup as shown in Figure 4.6. Figure 5.1 shows all $5^2S_{1/2} \rightarrow 5^2P_{3/2}$ transitions of both rubidium isotopes. There are two striking differences with the absorption spectrum as shown in the same Figure. First, there is no background signal; the only nonzero signals are the dispersion signals from the atomic transitions. Second, the closed transitions (discussed in Section 4.2.3) have the largest amplitude. This makes it easier to lock the laser frequency to the desired closed transition. This can also be seen in a close-up of the cooling transition in Figure 5.2. Further, if we count the number of dispersions, we find much more transitions than expected. We count 6 transitions (which is easier to see in the FM spectrum in the same Figure) instead of the expected three transitions. The three extra observed transitions are exactly halfway between the three atomic transitions and are the cross-over transitions, as discussed in Section 4.2.2 [25, 39]. In MT spectroscopy, the $F = 3 \rightarrow F = 4$ (cooling) transition has the largest dispersion signal and is easy to identify.

5.2 FM spectroscopy

To obtain the rubidium spectrum using FM spectroscopy, we use the FM PD in the full setup as shown in 4.6. A full spectrum of the $5^2S_{1/2} \rightarrow 5^2P_{3/2}$ transitions is shown in Figure 5.1. Although we still have a residual Doppler broadened background, we can resolve the transitions. FM spectroscopy also suffers from large cross-over transitions, and a big disadvantage is the

fact that cross-over transitions distort the local background in the spectrum. Therefore the zero crossing of the dispersion signal of the actual transition we are interested in might not be exactly on the resonance frequency of the atomic transition.

There are some differences between MT and FM spectroscopy. First, FM spectroscopy still suffers from a Doppler-broadened background which can shift the zero crossing of the actual transition frequency. Second, FM spectroscopy suffers from much larger signals from the cross-over transitions which can distort the signals from the actual transitions. In MT spectroscopy the cross-over transitions are suppressed and the cooling transition signal has the overall largest amplitude.

Now we have shown that we can perform basic spectroscopy and understand the obtained spectra, we need to optimize the signals for optimal feedback.

5.3 Optimizing the FM and MT spectroscopy signals

Although we have obtained the FM and MT spectroscopy signals, we would like to optimize their peak-to-peak amplitudes and peak-to-peak widths in order to obtain the best possible signals for locking the laser frequency. Apart from the alignment of the laser beams in the setup, there are also some other parameters which can be optimized.

5.3.1 Optimizing the phase in the feedback loop

When discussing the feedback electronics in Section 4.4, we briefly mentioned that there also is a possibility to adjust the phase (which essentially is the time delay) between the frequency generator and the signal obtained from the photodetector by adjusting the coaxial cable length between the splitter and the mixer. Generally, the phase between both signals will not be optimal and the dispersion signal obtained by the feedback electronics is a superposition of both the in-phase and out-of-phase components of the spectroscopy.

Typically, the propagation velocity v of an electrical signal through a coaxial cable of length L is approximately 70% of the speed of light. Calculating the cable length required to obtain a π rad phase shift, we have $\Delta\phi = 2\pi f \Delta t = 2\pi f L/v$. Using $v \approx 0.7 \cdot c$, $\Delta\phi = \pi$ rad and $f = 6.8$ MHz, we find $L \approx 15.4$ m. The MT feedback signal of the cooling transition is measured for coaxial cable lengths varying from 30 cm to 1550 cm. Figure 5.3 shows the dispersion signal for different cable lengths. We see that for a cable length of 15.5 m we have inverted the signal, i.e., induced a π phase shift, as expected from our calculation.

The best dispersion signal S as a function of the frequency ν has the highest gradient $\partial S/\partial\nu$ at the zero crossing in order to have the optimal signal-to-noise ratio to suppress fluctuations. Essentially this means that the peak-to-peak voltage of the dispersion signal should be maximized and the width of the minimum and maximum of the dispersion signal (also called the capture range) should also be minimized to have the largest gradient. However, the capture range should be wide enough to keep the laser frequency locked during large-amplitude fluctuations (e.g. incidental acoustic noise, such as voices or closing doors).

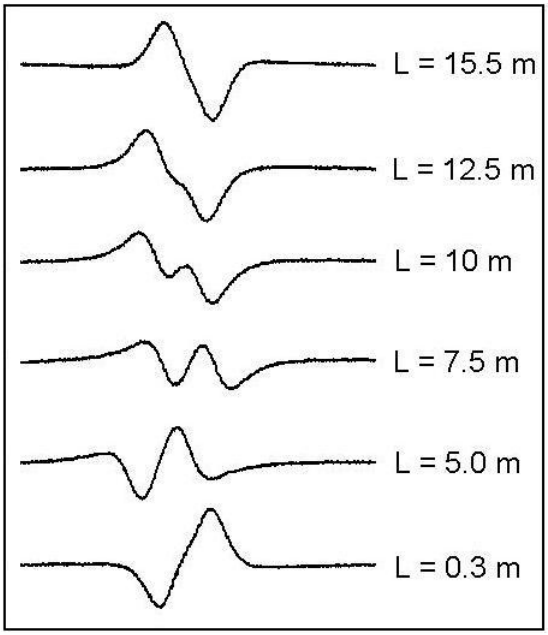

Figure 5.3: *MT dispersion signal of the cooling transition versus the laser frequency for different lengths L of coaxial cable between the splitter and the mixer. All scans are on the same scale, the maximum peak-to-peak voltage is approximately 200 mV. Notice that the central dispersion feature disappears going from $L = 10$ m to $L = 12.5$ m.*

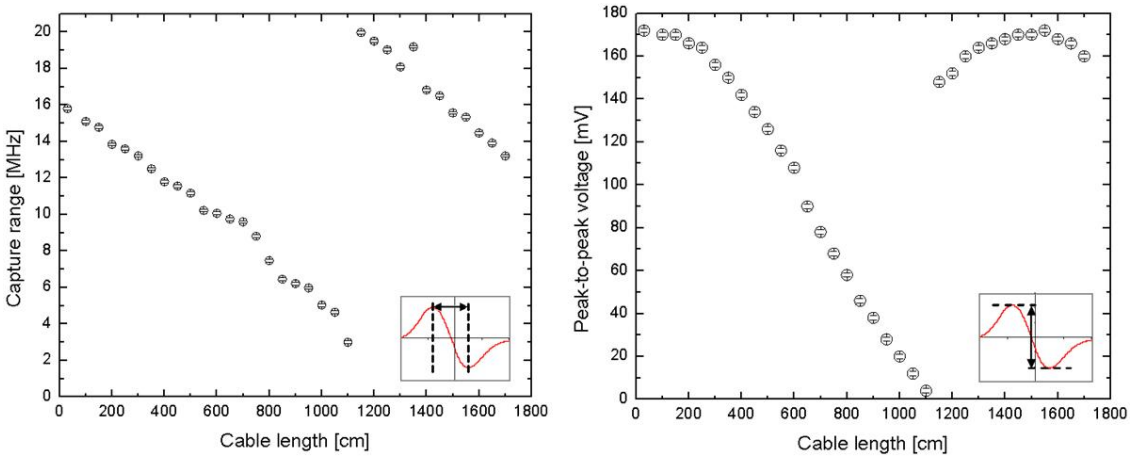

Figure 5.4: ***Left*** *Capture range (peak-to-peak width, see inset) of the cooling transition for different cable lengths. The capture range is estimated from the scope plots using the frequency scan rate of the laser, which is approximately 786.2 MHz/s.* ***Right*** *Peak-to-peak voltage (see inset) of the same transition for different cable lengths. The discontinuity at $L = 11$ m is due to the disappearance of the central dispersion, which can be seen in Figure 5.3.*

Figure 5.4 shows both the peak-to-peak amplitude and the capture range of the cooling transition dispersion as function of the coaxial cable length. The discontinuity at a cable length of 11 m is caused by the disappearance of the central dispersion signal and continuing in the larger dispersion signal (see Figure 5.3). From these graphs we conclude that a cable length of 30 cm is preferred for practical purposes and it already provides a large gradient.

5.3.2 Pump and probe beam intensities

In saturated absorption spectroscopy, the pump beam has a higher intensity than the probe beam [39]. But the optimal ratio of pump and probe beam intensity is not a priori clear, as it depends on the exact alignment and spatial overlap of the beams. It is easy to vary the ratio of intensities, as we have a half-wave plate in front of a polarizing beam splitter which creates the pump and probe beam. Figure 5.5 shows the peak-to-peak voltages of both MT and FM dispersion signals for different half-wave plate angles (relative to an arbitrary offset angle). Assuming a linear response of the MT and FM signals with respect to the intensity, the data is fitted with a $\sin^2$ curve, representing Malus' law [34]. The FM and MT peak-to-peak voltages have different amplitudes, but the maxima occur at the same half-wave plate angle, i.e., both signals are optimized for the same ratio of pump and probe beam intensities. In these measurements the total power in the setup, i.e. the pump and probe beam power combined, is approximately 4 mW.

We should mention here that, due to the layout of the setup, the definition of the pump and probe beams gets mixed up for both spectroscopy methods. In our discussion of the pump and probe beams throughout the whole report, they are named according to the MT spectroscopy scheme. This means that the pump beam acquires sidebands from the EOM (in the MT spectroscopy scheme) and it is this pump beam which is observed by the FM photodetector to create the FM spectroscopy dispersion signal.

By measuring the ratio of the pump and probe beam intensities as function of the half-wave plate angle, as shown in Figure 5.6, and comparing to the optimal angle from Figure 5.5, we find the optimal ratio to be $I_{pump}/I_{probe} = (2.5 \pm 0.3)$. This is within a factor of two of the optimal ratio as used by McCarron *et al* [41], and the difference is mainly caused by the difference in experimental parameters of our setup and theirs.

Having optimized the ratio of the intensities of the pump and probe beams, another interesting factor is the total power (the sum of the pump and probe beam intensities) in the spectroscopy setup. This can be controlled by the half-wave plate and polarizing beam splitter used before the free-space laser beam is coupled into the fiber (see Figure 4.5). Figure 5.7 shows the peak-to-peak voltages for both FM and MT spectroscopy at the optimal pump/probe intensity ratio, but for different total powers (which is the sum of the pump and probe beam powers). The FM signal seems to saturate at higher powers. Using the saturation intensity of the rubidium transition from Table 2.1, a power of 2 mW in a beam of 4 mm diameter results in a saturation parameter $s_0 = I/I_s \approx 9.7$, which is significantly larger than 1 and explains why the FM signal does not respond linearly any more. This simple analysis does not work for the MT signal, as this is already a nonlinear process.

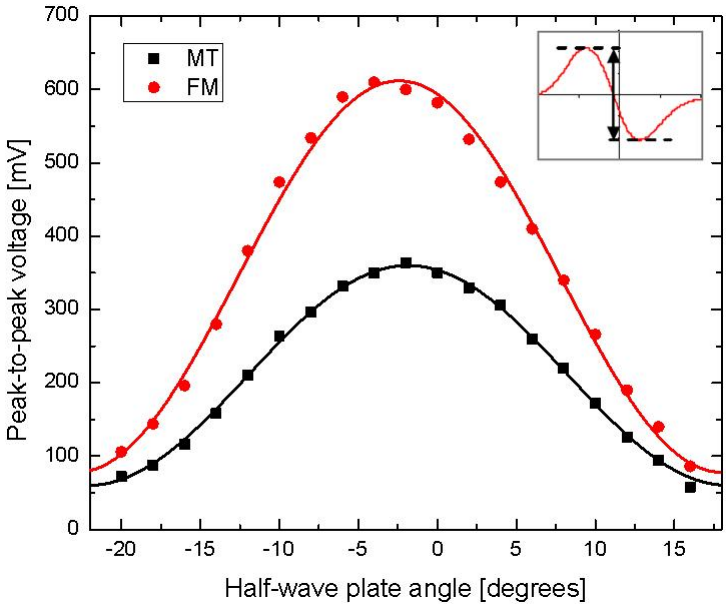

Figure 5.5: *Peak-to-peak voltage (see inset) of both the MT and FM dispersion signals of the cooling transition as function of the half-wave plate angle which distributes the intensities over the pump and probe beam. The full lines are fits of a simple sine function. The difference in angle of the two maxima is* (0.1 ± 0.2) *degrees, i.e., both maxima coincide.*

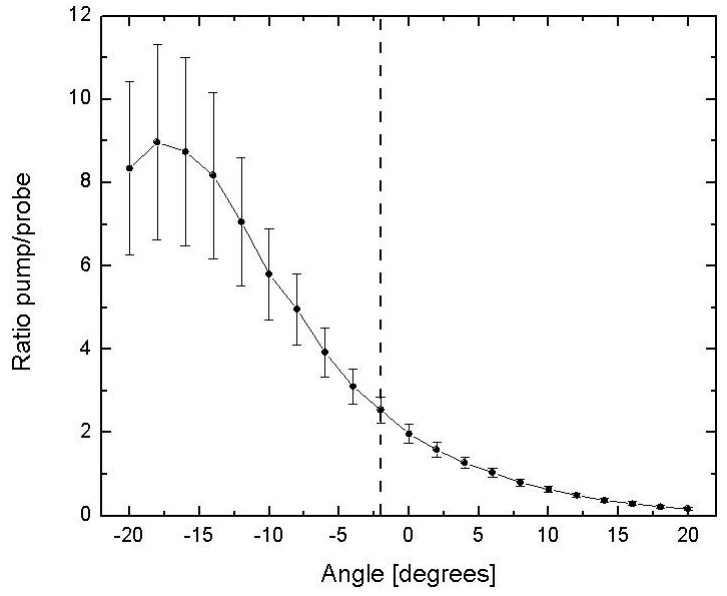

Figure 5.6: *Measured ratio of the pump and probe beam powers for different angles of the half-wave plate. The error bars represent systematic errors. The vertical dashed line represents the angle for which both signals are largest (see Figure 5.5). At this angle the optimal ratio is* (2.5 ± 0.3).

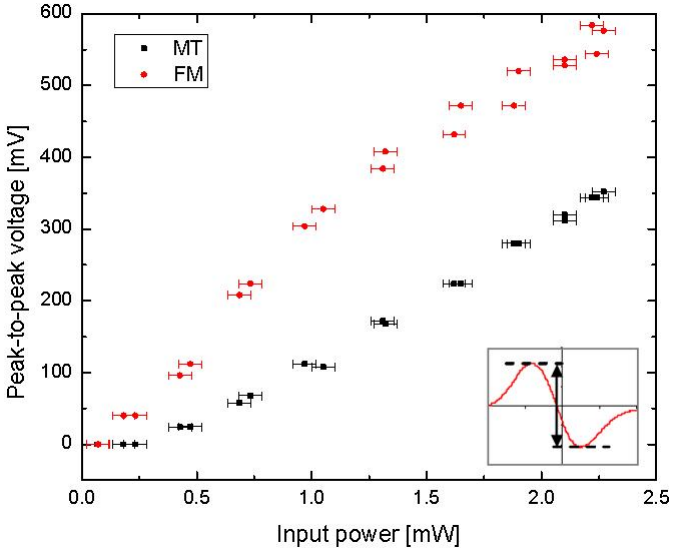

Figure 5.7: *Peak-to-peak voltage (see inset) of the MT and FM dispersion signals of the cooling transition as function of the total power in the spectroscopy setup (which is the sum of the probe and pump beam powers).*

5.4 Applying circular polarization and magnetic field

During this report we have continuously mentioned the ^{85}Rb cooling transition as the transition of interest. Further, we have mentioned a few times in this report that we would like to detune the laser frequency by locking it to a detuned atomic transition frequency using the Zeeman shift.

However, as we have also mentioned in Chapter 2, the transition from one hyperfine state F to another hyperfine state F' actually exists out of a manifold of transitions from magnetic substates M_F of hyperfine state F to magnetic substates $M_{F'}$ of hyperfine state F'. The rubidium level scheme including these magnetic substates for both rubidium isotopes is shown in Appendix B in Figures B.3 and B.4. We will present some calculations of the Zeeman shift as observed by FM spectroscopy in Section 5.4.2.

5.4.1 MT spectroscopy

We would like to observe the Zeeman-shift of the transitions in order to be able to lock the laser to a detuned frequency and we require the same circular polarization in both the pump and probe beams simultaneously. Using linear polarizations and Zeeman-shifting the energy levels would only lead to broadening of the transition width as the linear polarizations only allow $\Delta M_F = 0$ transitions, whereas $\sigma^{\pm}$ polarized light will pump the atomic states to either extreme $M_F = \pm F$ state, which allows for clear observation of the Zeeman shift [25, 39].

Figure 5.8 shows the peak-to-peak amplitude of the MT signal as function of the applied magnetic field and σ^+ or σ^- polarization of both pump and probe beam. The signal amplitude drops significantly, but at the same rate for either polarization. The shape of the dispersion signal for both polarizations in an applied magnetic field is shown in Figure 5.9. The optical pumping

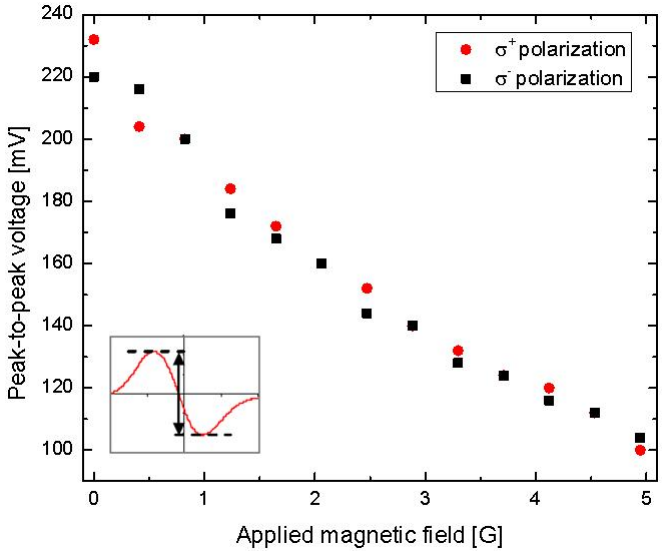

Figure 5.8: *Peak-to-peak amplitude (see inset) of the MT dispersion signal of the cooling transition for either σ^+ or σ^- polarised light as function of applied magnetic field. For magnetic fields exceeding 5 G, the dispersion signal is too distorted to obtain a well-defined peak-to-peak signal.*

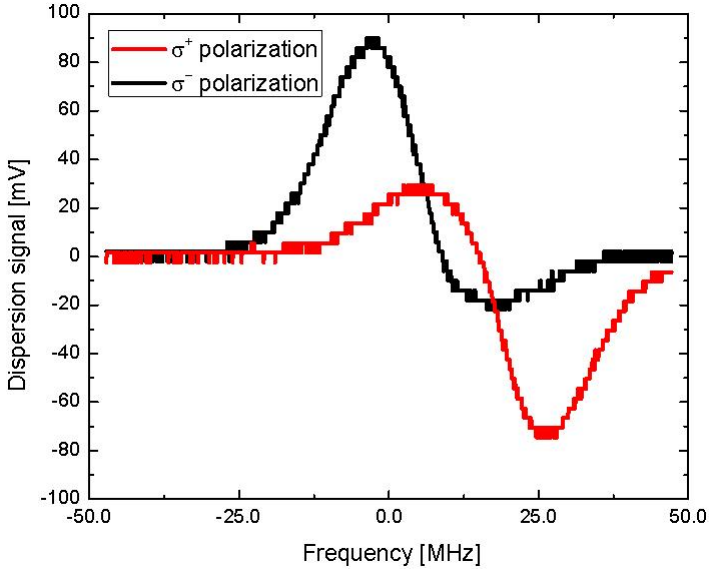

Figure 5.9: *MT dispersion signal of the cooling transition at an applied magnetic field of 4.9 G ($I = 0.6$ A) for either σ^+ or σ^- polarised light. The frequency axis is calculated from the scope time axis using the laser scan rate of 393.1 MHz/s. The steps on both curves is caused by the finite resolution of the scope. The scope vertical scale is set to 100 mV/div, and the scope resolution is 8 bits. As the full vertical scale is 10 divisions, the resolution is 1 V / $2^8 \approx 4$ mV, in agreement with the observed step sizes.*

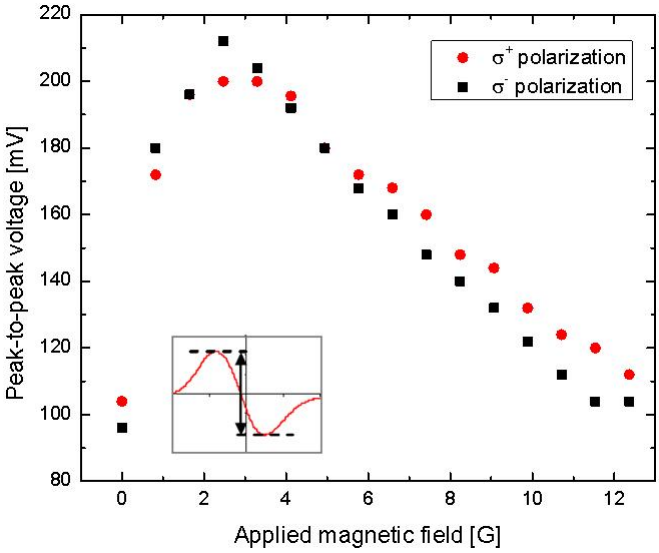

Figure 5.10: *Peak-to-peak amplitude (see inset) of the FM dispersion signal of the cooling transition for either σ^+ or σ^- polarized light as function of applied magnetic field.*

induced by the circular polarization creates an asymmetry in the dispersion signal. As the signal is no longer symmetrical, the zero crossing of the dispersion signal does not necessarily represent the actual Zeeman-shifted transition frequency. As mentioned before, McCarron *et al* claim that the MT signal is independent of the Zeeman shift [41]. As they do not present a clear reason why this should be, the MT signal cannot be interpreted in a clear way.

The MT spectroscopy signal is influenced by a magnetic field, but we cannot describe this merely as a frequency shift. There is currently no explanation available in the literature which discusses the MT spectroscopy signal for non-linear polarizations and magnetic fields. Therefore we conclude that for practical purposes the MT spectroscopy signal is an ideal candidate for locking at the transition frequency, but cannot be used to detune the laser frequency using the Zeeman shift.

5.4.2 FM spectroscopy

Similar as the measurement done for the MT signal, we measure the FM peak-to-peak voltage for different magnetic fields and either σ^+ or σ^- polarization. This is shown in Figure 5.10. For small magnetic fields (approximately 3 G), the FM peak-to-peak signal increases by more than a factor of two. This is probably due to the fact that there is a residual transverse magnetic field, as measured and discussed in Section 4.6, of approximately 1 G. Increasing the axial magnetic field to a few Gauss then produces a well-defined magnetic quantization axis collinear with the laser beams. This increases the optical pumping and thus the peak-to-peak signal. For larger magnetic fields the peak-to-peak signal decreases as the different transitions become more separated and do not add constructively to a single dispersion signal.

Calculating the Zeeman shift

A simple model has been developed to calculate the Zeeman shift of the separate transitions and to see what the overall dispersion signal will look like using FM spectroscopy. We assume that the Doppler width of the absorption is much larger than the linewidth of the transitions, which is justified as the Doppler width is approximately 500 MHz (calculated in Section 4.2.2), whereas the linewidth is approximately 6 MHz. We define the absorption $S(\nu)$ of all magnetic substate transitions ($M \rightarrow M',\ M' = M + 1$) of the ^{85}Rb cooling transition as

$$S(\nu) = \sum_{M=-3}^{3} C_M f(\nu, \nu'_M, \gamma'), \tag{5.1}$$

where $f(\nu, \nu'_M, \gamma')$ is defined as

$$f(\nu, \nu'_M, \gamma') = \frac{1}{\pi} \frac{(\gamma')^2}{(\nu - \nu'_M)^2 + (\gamma')^2}, \tag{5.2}$$

where C_M is proportional to the transition strength of the transition for σ^+ polarized light, obtained from [16] for all substate transitions. The power broadened linewidth γ' is defined as $\gamma' = \gamma\sqrt{1 + s_0}$, where $s_0 = I/I_s$ [25]. The Zeeman-shifted transition frequency ν'_i is calculated as

$$\nu'_M = \Big(g_{F'}(M + 1) - g_F M\Big)\frac{\mu_B}{h} B, \tag{5.3}$$

where $\mu_B/h \approx 1.4$ MHz/G is the Bohr magneton divided by Planck's constant, B the magnitude of the applied magnetic field and g_F the Landé factors of the lower or upper state (1/3 and 1/2, respectively). The Zeeman shift coefficients and the relative transition strengths for all transitions are listed in Table 5.2.

By calculating the Zeeman shift for each transition at a given magnetic field, we can calculate the absorption spectrum. Our model spectrum $f_{FM}(\nu_0)$ of the carrier frequency with the first order sidebands with which we probe the transitions is defined as

$$f_{FM}(\nu_0) = \delta_0(\nu_0) + \delta_{-1}(\nu_0 - \nu_{FM}) + \delta_{+1}(\nu_0 + \nu_{FM}), \tag{5.4}$$

Table 5.2: *Parameters used in the absorption model. The parameters are ordered by the integer i which is also used in the definition of the absorption. The calculation of the difference in Zeeman shift for the different magnetic substate transitions is also discussed in Appendix B.*

i	$M \rightarrow M + 1$	$g_{F'}(M + 1) - g_F M$	C_M [16]
3	$3 \rightarrow 4$	1	3780
2	$2 \rightarrow 3$	5/6	2835
1	$1 \rightarrow 2$	2/3	2025
0	$0 \rightarrow 1$	1/2	1350
-1	$-1 \rightarrow 0$	1/3	810
-2	$-2 \rightarrow -1$	1/6	405
-3	$-3 \rightarrow -2$	0	135

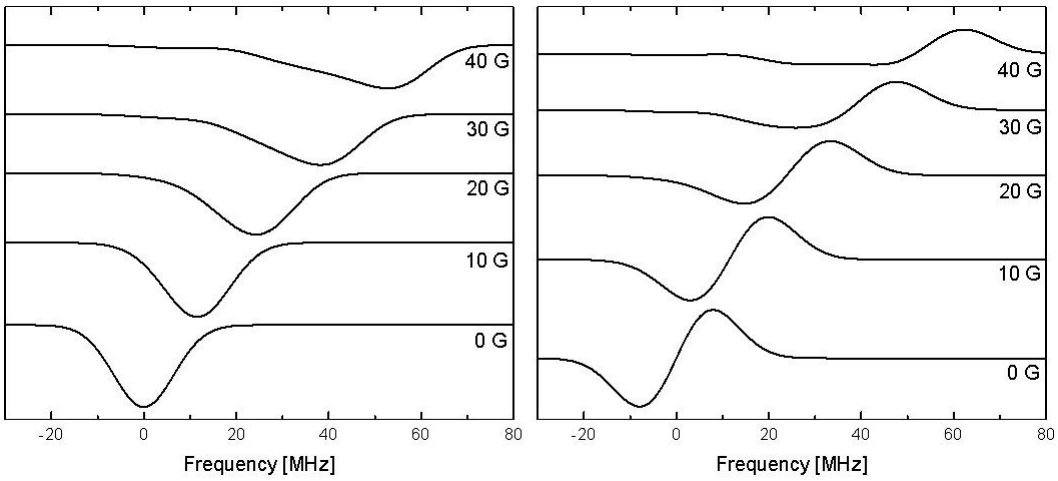

Figure 5.11: ***Left*** *Model absorption spectrum for different applied magnetic fields. The spectrum shifts and broadens when the magnetic field is increased. At large magnetic fields the spectrum becomes asymmetric due to the different Zeeman shifts of the different transitions.* ***Right*** *Calculated dispersion signals. The dispersion becomes asymmetric at high magnetic fields due to the broadening and asymmetry of the absorption dips.*

where ν_0 is the laser frequency, $\nu_{FM} = 6.8$ MHz the EOM modulation frequency, $\delta_{\pm 1} = 0.1\delta_0$ the relative amplitudes of the sidebands with respect to the laser amplitude[1]. The dispersion signal is calculated using the in-phase amplitude of Equation 4.9, where the amplitude of the in-phase component is proportional to the difference between the absorption of both sidebands.

The only parameter undefined yet is the power broadened linewidth γ'. We can calculate the power broadening as we know the total power in the vapour cell. We can also calculate the apparent peak-to-peak width of the dispersion signal as function of the power broadened linewidth. By comparing the apparent width with our observed width we find a power broadened linewidth of (13 ± 0.8) MHz. This is slightly over twice the natural linewidth $\gamma \approx 6$ MHz, and gives a saturation parameter of $s_0 \approx 3$ which is within a factor of two of the experimental conditions using this simple model.

Now that we have all parameters defined in our calculations, the absorption and resulting dispersion signals can be calculated and are shown in Figure 5.11. On the left hand side we see the absorption dips for different magnetic fields and on the right hand side we see the calculated FM spectroscopy signals. We see that the absorption signals (and, as a direct consequence, also the dispersion signals) shift as the magnetic field is increased. However, we also see that the signals become asymmetric. This is because the Zeeman splitting of the transitions becomes larger than the power broadened linewidth.

By determining the zero crossings of the dispersion signals, we can calculate the effective Zeeman shift for the different magnetic fields. This is shown in Figure 5.12. There are three lines shown. The full black line is the position of the zero crossing of the signals. The red dashed line is the frequency exactly halfway between the two dispersion peaks. We include this latter

[1]This ratio is based on our experimental results discussed in Section 4.5.2.

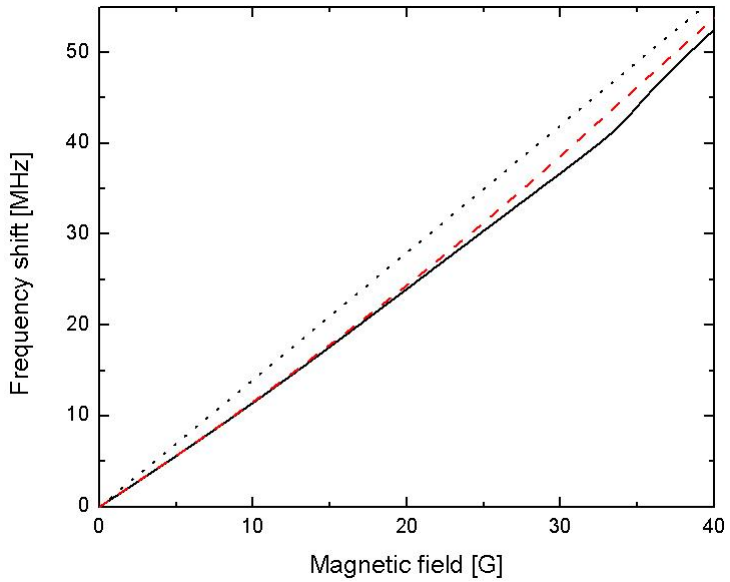

Figure 5.12: *Calculated frequency shift of the FM dispersion signal. The full black line represents the frequency of the zero crossing. The red dashed line is the frequency which is exactly in the middle of the two dispersion peaks. The dotted line represents the transition with the highest Zeeman shift of* 1.4 *MHz/G. For magnetic fields up to* 20 *G, our calculated Zeeman shift is approximately* 1.16 *MHz/G.*

calculation, as this method is often used in the laboratory. The dotted line is the Zeeman shift of the $M_F = 3 \rightarrow M_{F'} = 4$ transition, which has the highest Zeemans shift of 1.4 MHz/G. From these calculations we determine that the expected Zeeman shift for small fields (up to 13 G in our measurements) is 1.16 MHz/G. This is in agreement with a simple calculation which just takes the average over the Zeeman shifts of all transitions weighed by their respective absorption strengths C_i, which is also discussed in Section 3.6.1 and in Appendix B.

We learn two important things from these calculations. First, we observe a weighed average over all possible transitions. This decreases the Zeeman shift from the expected 1.4 MHz/G to 1.16 MHz/G. Second, for the magnetic fields in our experimental range (up to approximately 13 G), both methods to find the zero crossing give the same result.

Measuring the Zeeman shift

The Zeeman shift is induced using either σ^+ or σ^- polarized light using two quarter-wave plates in front and behind the vapor cell and applying a magnetic field using the copper wire coil.

To determine the frequency shift of the laser, we have to compare our laser frequency to a reference frequency. Contrary to the EOM spectrum measurements, where we use a second beam from our laser to create a beatnote, we now need an independent and uncorrelated frequency reference to measure the frequency fluctuations. The UCIS setup in our lab uses the same ^{85}Rb cooling transition for producing a MOT, and we transport a redundant beam from the UCIS laser

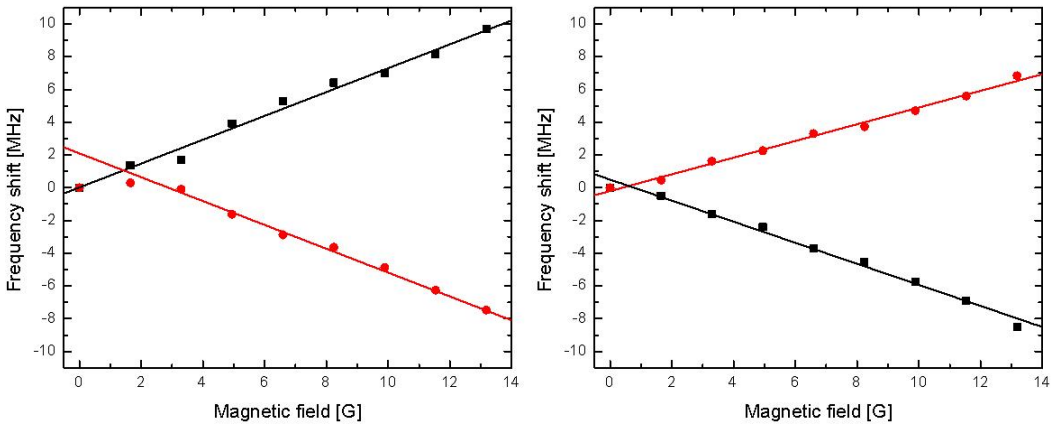

Figure 5.13: ***Left*** *Measured shift of the beatnote frequency for σ^+ polarized light. The red dots are obtained for a reversed magnetic field. From the linear fits we obtain a Zeeman shift of (0.73 ± 0.04) MHz/G and (-0.73 ± 0.02) MHz/G, respectively.* ***Right*** *Measured shift of the beatnote frequency for σ^- polarized light. Here, again, the red dots are obtained for a reversed magnetic field. From the linear fits we obtain a Zeeman shift of (-0.64 ± 0.04) MHz/G and (0.51 ± 0.02) MHz/G, respectively. In both graphs we define the beatnote frequency at $B = 0$ G as zero, in order to plot the frequency shift of the beatnote frequency.*

system[2] to our optical table using a fiber. Figure 4.6 shows a half-wave plate and a polarizing beam splitter that are used to continuously couple some of our laser light to the 'frequency metrology setup', which is where we produce a beatnote between our laser and the UCIS laser using a similar beatnote setup as explained in Section 4.5.2. For reasons of their own [17], the UCIS beam is detuned by a double-pass through an AOM resonating at 73.2 MHz. Hence if both lasers are locked exactly at the transition, the frequency difference between both lasers is 146.4 MHz and can be observed by our spectrum analyzer. For the data presented in this report, we use the digital Rohde&Schwarz spectrum analyzer. We also have an analog spectrum analyzer[3] which we use to optimize the beatnote signal and observe the beatnote during the day.

The Zeeman shift is measured by locking our laser frequency to the Zeeman-shifted dispersion signal and looking at the beatnote. A least-squares fit of the beatnote using a Lorentzian frequency distribution function gives the central frequency of the beatnote. Figure 5.13 shows the shift of the beatnote frequencies as function of the applied magnetic field for both polarizations. Further, we have also reversed the magnetic field (by reversing the current through the coil) and observed a reverse shift for both polarizations, as expected. The Zeeman shifts, however, are lower than expected. For σ^+ polarization we find shifts of (0.73 ± 0.04) MHz/G and (-0.73 ± 0.02) MHz/G, which are only 63% of the expected shift of 1.16 MHz/G. For the σ^- polarization we find even lower (and asymmetric) shifts of (-0.64 ± 0.04) MHz/G and (0.51 ± 0.02) MHz/G. This measurements are all performed on a single day, and the intensities of both beams have been kept constant. Further, the polarization of the beams is checked using the PBS in the spectroscopy setup, as the

[2]Toptica DLX 110 High Power Tunable Diode Laser.
[3]HAMEG Instruments HM5006 Spectrum Analyzer.

vertical polarized beam is rotated by 90 degrees after passing through two quarter-wave plates which are at the correct angles, the reflected intensity of the PBS goes to zero.

Figure 5.13 also shows that the negative frequency shift is only significant for applied magnetic field exceeding 2 G. This is because for a magnetic field magnitude exceeding 2 G, the applied magnetic field (which goes along the axial direction) dominates the measured transverse magnetic field of approximately 1 G (see Section 4.6). This residual magnetic field is also seen in the FM dispersion signal peak-to-peak amplitude measurement in Section 5.2.

5.4.3 Concluding remarks on tuning the transition frequency

We have looked at the effects of circularly polarized light and applied magnetic fields on the dispersion signal shape of both MT and FM spectroscopy. For MT spectroscopy, the dispersion signal does change in shape but no apparent shift is observed. For FM spectroscopy the dispersion shape does shift and can be used to detune the frequency of the transition.

Using circularly polarized light and applying a magnetic field, we are able to shift the transition frequency of the cooling transition using the Zeeman effect. We have developed a simple model which incorporates the Zeeman shift of all magnetic substate transitions which predicts a frequency shift of 1.16 MHz/G in our experimental range ($B < 20$ G). We determine a frequency shift of $(\pm 0.73 \pm 0.04)$ MHz/G for σ^+ polarized light for either axial direction of the magnetic field and (-0.64 ± 0.04) MHz/G or (0.51 ± 0.02) MHz/G for σ^- polarized light, depending on the axial direction of the applied magnetic field.

We conclude that FM spectroscopy cannot be used to accurately set the detuning, as the zero crossing of the dispersion signals is shifted by either residual magnetic fields or the Doppler broadened background. Further, we measure a different Zeeman shift than predicted, which makes this method unreliable to apply accurate frequency shifts. We see that MT spectroscopy is less sensitive to magnetic fields spectroscopy, although we do observe some change in the signal shape. By placing the vapor cell in a μ-metal box to minimize background magnetic fields, we propose to lock the laser frequency to the atomic transition frequency using MT spectroscopy, as it has the largest dispersion signal for the cooling transitions. The laser beam should then be detuned using two AOMs.

5.5 Frequency stability

We can the dispersion signal to stabilize our laser frequency using a PI controller[4] which drives the laser. Through this feedback system, the laser frequency is locked to the cooling transition frequency.

In order to observe the beatnote, we use the same beatnote setup with the UCIS laser as described in Section 5.4.2.

[4]Stanford Research Systems SIM960 Analog PID Controller.

5.5.1 Stability in terms of Allan variance

A common measure for frequency stability is the Allan variance [54]. The Allan variance σ_y^2 is defined as [54, 55]

$$\sigma_y^2(\tau) = \left\langle \frac{(\bar{y}_{k+1} - \bar{y}_k)}{2} \right\rangle, \tag{5.5}$$

where $\bar{y}_k$ is defined as

$$\bar{y}_k = \frac{1}{\tau} \int_{t_k}^{t_{k+\tau}} y(t) dt. \tag{5.6}$$

This average $\bar{y}_k$ represents the frequency averaged over a time τ for a specific interval k. The Allan variance can then be considered as the variance of the average frequency as function of the averaging time. Calculating the Allan variance of a dataset for different averaging times will yield information about the timescales of significant fluctuations in the frequency.

We obtain the Allan variance of the laser frequency by monitoring the beatnote using the Rohde&Schwarz digital spectrometer connected to a PC. Due to the low speed of the spectrometer and the connection to the PC, our sampling rate is limited to 1 Hz. This means that it is impossible to obtain information about higher frequency disturbances in the setup using this method, but we still obtain important information about the long-term stability of the laser.

The average frequency per spectrum scan is obtained by applying a least-squares fitting procedure of a Lorentzian frequency distribution $g(\nu)$ in Matlab

$$g(\nu) = A_0 + \frac{2A_1}{\pi} \frac{w^2}{w^2 + (\nu - \nu_0)^2}, \tag{5.7}$$

where A_0 and A_1 represent the background and the amplitude, w is the full-width at half the maximum amplitude and ν_0 is the central frequency. See Figure 5.14 for an example spectrum with its corresponding fit of the Lorentz distribution. Another Matlab script, based on the Allan variance calculations as described in [55] then calculates the Allan variance for different averaging times.

Figure 5.15 shows the beatnote frequency as monitored during an approximately two hour run. Ignoring the incidental spike, which is caused by acoustic disturbances (such as closing lab door, moving chairs and people talking with raised voices), we see that the lasers clearly drift but are stabilized near the central frequency which in the Figure, for convenience, is shifted to 0 Hz. Further, the frequency excursions do not exceed 100 kHz from the central frequency, which is well within our desired stability range of 300 kHz. Next to this graph, Figure 5.15 shows the corresponding Allan deviation of this dataset. The Allan deviation is the square root of the Allan variance. The shaded area on the Allan deviation in the Figure represents $\pm 1\sigma$ deviations of the average. The Allan deviation is a 10-20 kHz for averaging times of a few seconds, it quickly drops below 10 kHz for averaging times ranging from 10 to 100's of seconds. The increasing Allan deviation for longer timescales can be caused by small thermal fluctuations or fluctuations in the feedback system. But even for these longer timescales, the Allan deviation stays well below our required stability of 300 kHz.

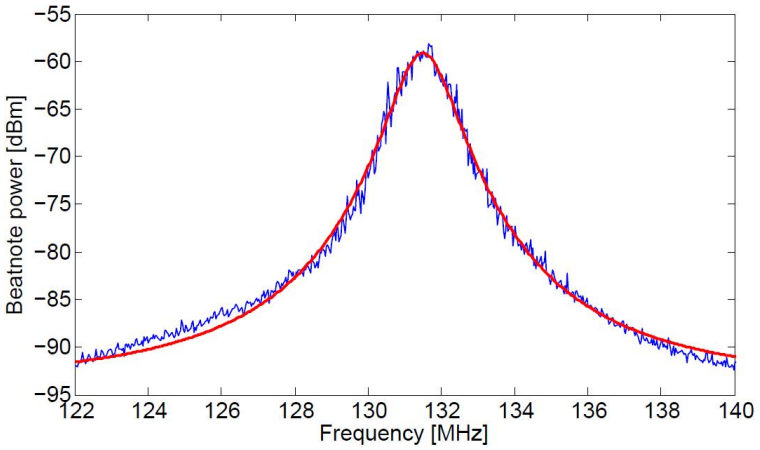

Figure 5.14: *Beatnote of our laser with the UCIS laser on a dBm scale (which is defined as a logarithmic scale with base* 10 *and* 0 $dBm = 1\ mW$*). This is a typical beatnote as measured during the Allan deviation measurements. The red line is a least-squares fit of a Lorentz distribution function. Near the maximum of the beatnote, the Lorentz distribution is a good approximation for the frequency distribution.*

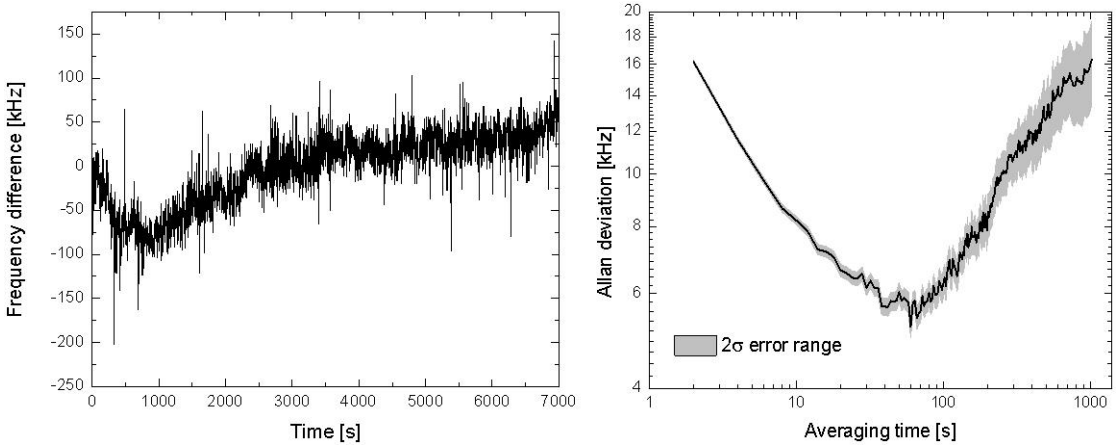

Figure 5.15: ***Left*** *Beatnote frequency monitored at a 1 Hz rate during approximately 2 hours. There are some spikes of* $\approx$ 100 *kHz, and there obviously is drift but the beatnote frequency does stabilize to its equilibrium frequency.* ***Right*** *Allan deviation for different averaging times of the left-hand monitored beatnote frequency. The shaded area represents the* $\pm 1\sigma$ *of the Allan deviation and increases for larger averaging times as the number of samples decreases. The typical dip with a minimum around* $\tau \approx 60$ *s is caused by two competing processes: the averaging out of all short-term fluctuations and the increasing long-term drift.*

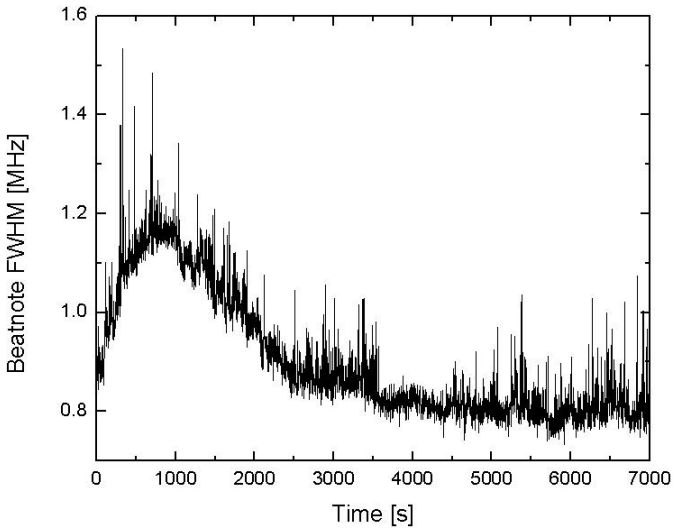

Figure 5.16: *Linewidth (FWHM) of the beatnote of our laser with the UCIS laser during the same two hour run from which the earlier Allan deviation is determined.*

5.5.2 Laser linewidth

The Allan deviation resulting from our measurements cannot reveal information about the frequency fluctuations of the beatnote at timescales shorter than 1 second. However, we can also look at the full-width at half maximum (FWHM) of the beatnote to estimate the maximum size of the frequency fluctuations within this 1 second. The FWHM of the beatnote as determined during the same measurement from which we calculate the Allan deviation is shown in Figure 5.16. The FWHM exceeds 1 MHz for the first 2000 seconds of the measurement, which coincides with the largest drift of the beatnote frequency as shown in Figure 5.15. For most of the time, the FWHM is below 900 kHz.

The frequency fluctuations of both lasers are distributed following a Lorentzian distribution and the FWHM of this distribution is called the linewidth of the laser [39]. The FWHM, or equivalently the linewidth, of the beatnote should be interpreted as a convolution of both linewidths of the two lasers used to create the beatnote. Also, the convolution of two Lorentzian distributions with linewidths w_1 and w_2 results in a Lorentzian distribution with linewidth $w = w_1 + w_2$ [25]. In order to approximate the linewidths of the laser, we have to recognize that both lasers are quite different in design: our Titanium:Sapphire ring laser has an extremely long cavity (approximately 2 meters), whereas the UCIS laser is a diode laser with a cavity of a few hundred microns. Further, different processes take place in a diode laser due to the dynamics in the charge carrier density. The minimal linewidth achievable by a laser, also known as the Schawlow-Townes limit [56], is increased in diode lasers because of these interactions [57]. Whereas the linewidth of a Titanium:Sapphire laser is below 500 kHz [33], the typical linewidth of the UCIS laser is specified as approximately 1 MHz [58]. We observe a beatnote of approximately 1 MHz, which is consistent with the linewidth of the diodelaser. This means that we cannot set a lower limit on our Titanium:Sapphire laser linewidth, and can only state as upper limit that it is much smaller than 1 MHz.

Chapter 6

Discussion and conclusion

This report consists out of two main subjects. In Chapters 2 and 3 we report on a new type of high brightness ion beam source, which we call the Atomic Beam Laser-cooled Ion Source or ABLIS. Using the well-known physics of laser cooling and compression, an analytical model is developed to predict the performance of the ABLIS.

As the analytical model is based on a few simplifications, such as an ideal 2-level atom structure and 100% efficient transverse cooling and compression of the atomic beam, we also perform simulations of the laser cooling and compression stage. In these simulations we look at both rubidium isotopes and take account of the different magnetic substate structure of the ground and excited levels. These simulations also have their limitations, as they ignore transitions to other hyperfine levels and ignore the optical thickness or collision rates of the atoms in the cooled and compressed beam. However, they are a good tool to investigate the effects of using different isotopes. Assuming a purified, single-isotope atomic beam, we find maximum achievable reduced brightnesses of $2 \cdot 10^7$ A / m^2 srad eV for ^{85}Rb and 10^8 A / m^2 srad eV for ^{87}Rb. These reduced brightnesses are achieved with laser intensities of 3.3 mW/cm^2 (twice the saturation parameter) and a laser frequency detuning of $\delta = -\gamma/2 \approx 3$ MHz with respect to the cooling transition. Typically a source temperature of 400 K and a magnetic field gradient of 3 T/m are required for optimal cooling and compression and achieving the highest flux. Of these parameters, the final achievable brightness is most sensitive to the detuning of the laser.

We have also investigated stochastic heating effects which limit the final attainable brightness of the ion beam. Stochastic heating is caused by disordered Coulomb interactions between the ions. These disordered interactions are a result of the ionization of the neutral cooled and compressed atomic beam. Using simulation results based on the cooling and compression of a pure ^{87}Rb beam, and including the Coulomb interaction between the ions, the maximum reduced brightness of $2{\cdot}10^7$ A / m^2 srad eV stays constant for currents up to 20 pA and at a longitudinal energy spread of 0.7 eV. Under these circumstances, the resulting ion beams are in the so-called pencil beam regime, where the number of transverse neighbouring ions is low enough for disordered transverse Coulomb forces to become neglible.

The calculated reduced brightnesses are much higher than can be achieved by the common Liquid Metal Ion Source (LMIS) or the Ultra Cold Ion Source (UCIS). The Gas Field Ionization

Source (GFIS) performs in the same order of magnitude, but the ABLIS is a much more likely method to be used for milling purposes as the penetration depth of rubidium atoms is much shorter than for the light noble gases like helium and neon that are currently used for GFIS.

In the second part of this report, Chapters 4 and 5, we investigate two possible methods to stabilize the laser frequency of a Titanium:Sapphire ring laser system to the required rubidium transition frequency with a detuning of approximately 3 MHz with an accuracy and stability of 10%. The detuning is achieved by Zeeman shifting the atomic transition frequency.

From our experiments we find that modulation transfer (MT) spectroscopy cannot be used to lock the laser frequency to a Zeeman-shifted atomic transition frequency, as the change in the MT dispersion signal due to an applied magnetic field cannot be accounted for by purely a frequency shift. As there currently is limited literature available to explain the effect of magnetic fields and circular polarization on four-wave mixing processes such as MT spectroscopy, we conclude that MT spectroscopy currently cannot be used for detuning the laser frequency.

Frequency modulation (FM) spectroscopy does show a clear Zeeman shift of the frequencies, but we do not observe the shift rate as predicted by a simple model taking all possible magnetic substate transitions into account. This could be caused by background magnetic fields. Further, the dispersion signal suffers from a Doppler broadened background. These factors make it more difficult to use the FM spectroscopy signal to find the exact transition frequency.

Based on this work on both MT and FM spectroscopy, we propose that locking and stabilizing the laser frequency on the atomic transition frequency as discussed in this report should be based on MT spectroscopy (additionally even placing the reference vapor cell in a μ-metal box to exclude any external magnetic fields) and detuning the laser frequency going to the cooling and compression stage using two acousto-optical modulators (AOMs).

Finally we have measured the frequency stability of the locked laser by determining the Allan variance of the beatnote frequency between our laser and the UCIS laser, which is locked to the same transition frequency. We find that the frequency fluctuations are below 20 kHz at averaging times between 1 to 1000 seconds, which is more than sufficient for future experiments. As the linewidth of the beatnote ($\approx$ 900 kHz) is fully dominated by the linewidth of the UCIS diode laser system (specified linewidth of $\approx$ 1 MHz), the linewidth of our laser should be much smaller, but it is not possible to make a more accurate upper limit.

Appendix A

Flux model

In the analytical model and the simulations as explained in Chapters 2 and 3, we refer to full analytical flux calculations. These are presented in this Appendix. We calculate the flux going through the first aperture for two geometries: circular and square orifice and aperture geometries. We will discuss the difference between both geometries and compare the full analytical expressions with the paraxial approximation.

Approach

The initial expansion stage of the atomic beam setup has couple of geometric variables which determine the flux through the aperture. These geometric variables are the source aperture size d_s, the first aperture size d_a and the distance between the source and the aperture l. The apertures are centered at the z-axis at positions $z = 0$ for the source and $z = l$ for the first aperture. In order to assess the configuration of the expansion stage of the setup, the flux emerging from the source aperture should be calculated at the first aperture. We use two different aperture geometries: squares with sides $2d_s$ (source) and $2d_a$ (aperture), and circular apertures with radii d_s (source) and d_a (aperture), respectively. We calculate the flux for both geometries, as the circular geometry is used in the analytical model in Section 2.2, whereas a square geometry is used in the simulations. In both the analytical model and the simulations we will use $d_s = d_a = d$. Further, the ratio of the aperture size d and distance l will be $\theta = d/l \ll 1$. Although a fully analytical result dependent on d_s, d_a and l will be presented first, the latter two assumptions will be incorporated to give approximate (and much simpler) solutions.

Effusive source

The number of particles, d^4N, leaving the source area element, $d\sigma$, during the time, dt, with a velocity between v and $v + dv$ into a solid angle element, $d\omega$, whose axis is at an angle, θ, with respect to the normal of $d\sigma$ is given by [24]

$$d^4N = n_0 f(v) \frac{d\omega}{4\pi} v \cos(\theta) d\sigma dt dv, \tag{A.1}$$

where n_0 is the number density of the source and $f(v)$ the Maxwell-Boltzmann speed distribution normalized to 1

$$f(v)dv = \frac{4}{\sqrt{\pi}} \frac{v^2}{v_{mp}^3} \exp[-(v/v_{mp})^2]dv, \tag{A.2}$$

where $v_{mp} = \sqrt{2k_B T_s/m}$ is the most probable velocity (k_B is Boltzmann's constant). The differential number density n at a distance R from the source is given as

$$n(R, \theta, v) = \frac{d^4N}{d^2V} = \frac{n_0}{\pi^{3/2}} \frac{v^2}{v_{mp}^3} \exp[-(v/v_{mp})^2]dv \frac{\cos(\theta)}{R^2} d\sigma, \tag{A.3}$$

where we have defined $d^2V = R^2 d\omega v dt$ as the solid angle volume differential element. In order to transform the differential number density to a flux density $d^3\Phi$, we have to multiply the differential number density by the effective velocity through the aperture surface

$$d^3\Phi = n(R, \theta, v) \times (\vec{v} \cdot d\vec{A}), \tag{A.4}$$

where $d\vec{A}$ is the unit vector normal to the aperture surface. In an axisymmetric system, such as ours, the source surface and aperture surface are parallel. Therefore the angle between the velocity and the unit normal vector of both surfaces is identical, θ. Therefore we have $\vec{v} \cdot d\vec{A} = v\cos(\theta)dA$ and we can write the flux density as

$$d^3\Phi = \frac{n_0}{\pi^{3/2}} \frac{v^3}{v_{mp}^3} \exp[-(v/v_{mp})^2]dv \frac{\cos^2(\theta)}{R^2} d\sigma dA. \tag{A.5}$$

Integrating over the speeds gives us the average speed:

$$\int_0^\infty \frac{v^3}{v_{mp}^3} \exp[-(v/v_{mp})^2]dv = \frac{\sqrt{\pi}}{4}\langle v \rangle, \tag{A.6}$$

which reduces our flux density to a geometric problem:

$$d^2\Phi = \frac{n_0}{4\pi}\langle v \rangle \frac{\cos^2(\theta)}{R^2} d\sigma dA, \tag{A.7}$$

as the integrals over $d\sigma$ and dA only involve the actual geometry of the source and the aperture. The calculation of these integrals for both square and circular apertures will be the subject in the next two sections.

The general recipe can be discussed here. First we solve the integral over $d\sigma$ by defining a position $\vec{r}_0$ in the aperture from which we 'look' at the source. This will give a nondimensional density distribution

$$g(d_s, l, \vec{r}_0) = \int \frac{\cos(\theta)^2}{R^2} d\sigma, \tag{A.8}$$

which is related to the flux density as

$$d\Phi = \frac{n_0}{4\pi}\langle v \rangle g(d_s, l, \vec{r}_0) dA. \tag{A.9}$$

Next we integrate over the aperture dA, which gives us the integrated density

$$G(d_s, d_a, l) = \int g(d_s, l, r_0) dA, \tag{A.10}$$

which is related to the flux going through the aperture as

$$\Phi(d_s, d_a, l) = \frac{n_0}{4\pi}\langle v\rangle G(d_s, d_a, l). \tag{A.11}$$

We can check this flux in the limit $d_a \gg l \gg d_s$ i.e. the aperture is much larger than the source. In that case the flux through the aperture should be equal to the total flux emitted by the source:

$$\lim_{d_a\to\infty} \Phi(d_s, d_a, l) = \frac{1}{4} n_0 \langle v\rangle S, \tag{A.12}$$

where S is the surface of the source.

Square apertures

In order to calculate the flux at the aperture, we first calculate the particle density at a point $\vec{r}_0 = (x_0, y_0)$ in the aperture, where $-d_a \leq (x_0, y_0) \leq d_a$. From each position at the aperture we have to consider the particles emerging from the whole source aperture.

We start with a differential element $d\sigma = dxdy$ at a position (x, y) at the source aperture, where $-d_s \leq (x, y) \leq d_s$. The angle between the differential element and a point at the aperture with respect to the z-axis is given by

$$\theta(x, x_0, y, y_0, l) = \arctan\left(\frac{\sqrt{(x-x_0)^2 + (y-y_0)^2}}{l^2}\right). \tag{A.13}$$

The distance R between the differential element and the point at the aperture is

$$R = \frac{l}{\cos(\theta(x, x_0, y, y_0, l))}. \tag{A.14}$$

Through the definition of the density distribution function as in Equation A.8, we have

$$g_s(d_s, x_0, y_0, l) = \frac{1}{l^2}\int_{-d_s}^{d_s}\int_{-d_s}^{d_s} dxdy \cos^4(\theta(x, x_0, y, y_0, l)). \tag{A.15}$$

Using the trigonometric property that $\cos(\arctan(z)) = (1+z^2)^{-1/2}$, we can write the integral as

$$g_s(d_s, x_0, y_0, l) = l^2\int_{-d_s}^{d_s}\int_{-d_s}^{d_s} \frac{dxdy}{(l^2 + (x-x_0)^2 + (y-y_0)^2)^2}. \tag{A.16}$$

Performing the integration gives

$$\begin{aligned}
g_s(d_s, x_0, y_0, l) = {} & \frac{d_s - y_0}{2\sqrt{l^2 + (d_s - y_0)^2}}\left[\arctan\left(\frac{d_s - x_0}{\sqrt{l^2 + (d_s - y_0)^2}}\right) - \arctan\left(\frac{-(d_s + x_0)}{\sqrt{l^2 + (d_s - y_0)^2}}\right)\right] \\
& + \frac{d_s - x_0}{2\sqrt{l^2 + (d_s - x_0)^2}}\left[\arctan\left(\frac{d_s - y_0}{\sqrt{l^2 + (d_s - x_0)^2}}\right) - \arctan\left(\frac{-(d_s + y_0)}{\sqrt{l^2 + (d_s - x_0)^2}}\right)\right] \\
& + \frac{d_s + x_0}{2\sqrt{l^2 + (d_s + x_0)^2}}\left[\arctan\left(\frac{d_s - y_0}{\sqrt{l^2 + (d_s + x_0)^2}}\right) - \arctan\left(\frac{-(d_s + y_0)}{\sqrt{l^2 + (d_s + x_0)^2}}\right)\right] \\
& + \frac{d_s + y_0}{2\sqrt{l^2 + (d_s + y_0)^2}}\left[\arctan\left(\frac{d_s - x_0}{\sqrt{l^2 + (d_s + y_0)^2}}\right) - \arctan\left(\frac{-(d_s + x_0)}{\sqrt{l^2 + (d_s + y_0)^2}}\right)\right].
\end{aligned} \tag{A.17}$$

This is the density distribution. In order to calculate the flux through the aperture, this density distribution should be integrated over the aperture plane. This gives the integrated density through the aperture G_s as

$$G_s(d_s, d_a, l) = \int_{-d_a}^{d_a} \int_{-d_a}^{d_a} dx_0 dy_0 \; g_s(d_s, x_0, y_0, l). \tag{A.18}$$

If $d_s = d_a = d$, this reduces to

$$G_s(d, l) = 8d\left[\sqrt{4d^2 + l^2}\arctan\left(\frac{2d}{\sqrt{4d^2 + l^2}}\right) - l\arctan\left(\frac{2d}{l}\right)\right] + 2l^2\ln\left(\frac{4d^2 + l^2}{\sqrt{8l^2d^2 + l^4}}\right). \tag{A.19}$$

The function G_s should have a well defined limit in the case $d_a \gg l \gg d_s$, as there is a finite amount of flux emitted by the source and all will move through the aperture in the aforementioned limit. The limiting value of G_s is

$$G_s(d_a \gg l \gg d_s) = 4\pi d_s^2, \tag{A.20}$$

which leads to the total flux

$$\Phi = \frac{n_0}{4\pi}\langle v\rangle G_s(d_a \gg l \gg d_s) = \frac{1}{4}n_0\langle v\rangle(2d_s)^2 = \frac{1}{4}n_0\langle v\rangle S, \tag{A.21}$$

where S is the surface of a square source with side $2d_s$. This is exactly the required limit as discussed in Section A.

The fraction of the total amount of flux which goes through the aperture can be defined as

$$\eta_s(d_s, d_a, l) = \frac{G_s(d_s, d_a, l)}{G_s(d_a \gg l \gg d_s)} = \frac{1}{4\pi d_s^2}G_s(d_s, d_a, l). \tag{A.22}$$

Further, we can also define an asymmetry parameter which is a measure of the uniformity of the density distribution at the aperture. The asymmetry parameter is defined as

$$\epsilon_s(d_s, d_a, l) = \frac{g_s(d_s, l, x_0 = y_0 = 0) - g_s(d_s, l, x_0 = y_0 = d_a)}{g_s(d_s, l, x_0 = y_0 = 0) + g_s(d_s, l, x_0 = y_0 = d_a)}. \tag{A.23}$$

Now we have an analytical model for a set of square apertures. In the real experiment the apertures will be circular, and we will discuss those now.

Circular apertures

In order to calculate the flux at the aperture, we first calculate the particle density at a point $\vec{r}_0 = (r_0, \phi_0)$ in the aperture, where $0 \leq r_0 \leq d_a$ and $0 \leq \phi_0 < 2\pi$. From each position at the aperture we have to consider the flux emerging from the whole source aperture.

In order to solve the integrals, we start with a differential surface element $d\sigma = rdrd\phi$ at a position (r, ϕ) at the source aperture, where $0 \leq r \leq d_s$ and $0 \leq \phi < 2\pi$. The angle between the differential element and a point at the aperture with respect to the z-axis is given by

$$\theta(r, r_0, \phi, \phi_0, l) = \arctan\left(\frac{\sqrt{r^2 + r_0^2 - 2rr_0\cos(\phi - \phi_0)}}{l^2}\right). \tag{A.24}$$

The distance R between the differential element and the point at the aperture is

$$R = \frac{l}{\cos(\theta(r, r_0, \phi, \phi_0, l))}. \tag{A.25}$$

The density distribution function of this circular source and circular aperture g_c as given by Equation A.8 is

$$g_c(r_0, \phi_0, d_s, l) = \frac{1}{l^2} \int_0^{2\pi} \int_0^{d_s} r dr d\phi \cos^4(\theta(r, r_0, \phi, \phi_0, l)). \tag{A.26}$$

Using the trigonometric property that $\cos(\arctan(z)) = (1+z^2)^{-1/2}$, we can write the integral as

$$g_c(r_0, d_s, l) = l^2 \int_0^{2\pi} \int_0^{d_s} \frac{r dr du}{(l^2 + r_0^2 + r^2 - 2rr_0\cos(u))^2}, \tag{A.27}$$

where we have used the transformation $\phi - \phi_0 = u$. The result of the angular integration is

$$g_c(r_0, d_s, l) = l^2 \int_0^{d_s} r dr \left[\frac{2(l^2 + r^2 + r_0^2)}{((l^2 + (r-r_0)^2)(l^2 + (r+r_0)^2))^{3/2}} \arctan\left(\sqrt{\frac{l^2 + (r-r_0)^2}{l^2 + (r+r_0)^2}} \tan\left(\frac{u}{2}\right) \right) + \frac{2rr_0}{(l^2 + (r-r_0)^2)(l^2 + (r+r_0)^2)} \frac{\sin(u)}{l^2 + r_0^2 + r^2 - 2rr_0\cos(u)} \right]_0^{2\pi}. \tag{A.28}$$

There is a π angle symmetry in this integral, and calculating the integral using the current boundaries gives an incorrect result (i.e. zero). The second term does (correctly) go to zero, but the first term displays discontinuities (due to the $\tan(u/2)$ term) and should be linearized in order to calculate the integral. By defining the factor β as

$$\beta = \sqrt{\frac{l^2 + (r-r_0)^2}{l^2 + (r+r_0)^2}} \tag{A.29}$$

which is $\beta \approx 1$ for our experimental parameters of $l \approx 10^{-2}$ m and $r \approx r_0 \approx 10^{-4}$ m, the angular part of the first term can be linearized as

$$\arctan\left(\beta \tan\left(\frac{u}{2}\right)\right) \approx \frac{1}{2}\beta u + \frac{1}{24}\beta(1-\beta^2)u^3 + O(u^5). \tag{A.30}$$

Using the integration limits $u = 0$ and $u = 2\pi$, we find

$$\left[\arctan\left(\beta \tan\left(\frac{u}{2}\right)\right) \right]_0^{2\pi} \approx \beta\pi. \tag{A.31}$$

We can thus write our integral as

$$g_c(r_0, d_s, l) = 2\pi l^2 \int_0^{d_s} dr \frac{r(l^2 + r^2 + r_0^2)}{(l^2 + (r-r_0)^2)(l^2 + (r+r_0)^2)^2}. \tag{A.32}$$

This integral can be solved and gives

$$g_c(r_0, d_s, l) = \frac{\pi}{2} - \frac{\pi}{2}\frac{l^2 + r_0(r_0 + d_s)}{l^2 + (r_0 + d_s)^2} + \frac{\pi}{4}\frac{l}{r_0}\left[\arctan\left(\frac{d_s - r_0}{l}\right) - \arctan\left(\frac{d_s + r_0}{l}\right) \right] + \frac{\pi}{2}\left[\frac{l}{r_0} + \frac{r_0}{l}\right] \arctan\left(\frac{r_0}{l}\right) - \frac{\pi}{2}\frac{r_0}{l} \arctan\left(\frac{d + r_0}{l}\right). \tag{A.33}$$

Similar to the solution of the square apertures, this result represents the local flux density. In order to calculate the flux going through the aperture, you have to integrate this result over the area of the aperture. This gives

$$G_c(d_s, d_a, l) = 2\pi \int_0^{d_a} r_0 g_c(r_0, d_s, l) dr_0. \tag{A.34}$$

Unfortunately this function has a discontinuity at $d_s = d_a$. Therefore we have to define a new function $\widetilde{G}_c(d_s, d_a, l)$, which is

$$\widetilde{G}_c(d_s, d_a, l) = \begin{cases} G_c(d_s, d_a, l) & d_a \leq d_s \\ G_c(d_s, d_a, l) + \Delta & d_a > d_s \end{cases} \tag{A.35}$$

where Δ is defined as

$$\Delta = \lim_{d_a \uparrow d_s} G_c(d_s, d_a, l) - \lim_{d_a \downarrow d_s} G_c(d_s, d_a, l) = \frac{\pi^3}{2} l d_s. \tag{A.36}$$

The function $\widetilde{G}_c$ should have a well defined limit in the case $d_a \gg l \gg d_s$, as there is a finite amount of flux emitted by the source and all will move through the aperture in the aforementioned limit. This limiting value is

$$\widetilde{G}_c(d_a \gg l \gg d_s) = \pi^2 d_s^2. \tag{A.37}$$

This leads to the total flux

$$\Phi = \frac{n_0}{4\pi} \langle v \rangle \widetilde{G}_c(d_a \gg l \gg d_s) = \frac{1}{4} n_0 \langle v \rangle \pi d_s^2 = \frac{1}{4} n_0 \langle v \rangle S. \tag{A.38}$$

This is exactly the required limit as discussed in Section A.

The above result shows that the total flux going through the aperture is limited by the source size. This limiting value is slightly different to the limiting value for a square aperture, but can be easily understood as the ratio of the limiting values

$$\frac{\widetilde{G}_c(d_a \gg l \gg d_s)}{G_s(d_a \gg l \gg d_s)} = \frac{\pi^2 d_s^2}{4\pi d_s^2} = \frac{\pi}{4} \tag{A.39}$$

is the ratio of the surfaces of a square and a circle with equal dimensions.

Taking the aformentioned discontinuity at $d_s = d_a$ into account, we can still calculate G_c for equal source and aperture sizes $d_s = d_a = d$:

$$\begin{aligned} G_c(d, l) = \frac{d^2\pi^2}{3} + \frac{ld\pi^3}{4} + ld\pi^2 \Bigg[\frac{3}{2} \arctan\left(\frac{d}{l}\right) - \arctan\left(\frac{2d}{l}\right) - \frac{1}{2} \arctan\left(\frac{l}{d}\right) \\ + \frac{2}{3}\left(\frac{d}{l}\right)^2 \left[\arctan\left(\frac{d}{l}\right) - \arctan\left(\frac{2d}{l}\right) \right] \Bigg] + \frac{l^2\pi^2}{12} \ln\left(\frac{l^{14}(4d^2 + l^2)}{(d^2 + l^2)^8}\right). \end{aligned} \tag{A.40}$$

Similar to the square aperture model, we can define two numbers which characterize the aperture. The first is the fraction of the total amount of flux which goes through the aperture. It is defined as

$$\eta_c(d_s, d_a, l) = \frac{\widetilde{G}_c(d_s, d_a, l)}{\widetilde{G}_c(d_a \gg l \gg d_s)} = \frac{1}{\pi^2 d_s^2} \widetilde{G}_c(d_s, d_a, l), \tag{A.41}$$

which, in the case of equal radii, reduces to

$$\eta_c(d,l) = \frac{1}{3} + \frac{l}{d}\left[\frac{\pi}{4} + \frac{3}{2}\arctan\left(\frac{d}{l}\right) - \arctan\left(\frac{2d}{l}\right) - \frac{1}{2}\arctan\left(\frac{l}{d}\right)\right] + \frac{2}{3}\frac{d}{l}\left[\arctan\left(\frac{d}{l}\right) - \arctan\left(\frac{2d}{l}\right)\right] + \frac{1}{12}\left(\frac{l}{d}\right)^2 \ln\left(\frac{l^{14}(4d^2+l^2)}{(d^2+l^2)^8}\right). \tag{A.42}$$

We can also define an asymmetry parameter which is a measure of the uniformity of the density distribution at the aperture. The asymmetry parameter is defined as

$$\epsilon_c(d_s, d_a, l) = \frac{g_c(d_s, l, r_0 = 0) - g_s(d_s, l, r_0 = d_a)}{g_s(d_s, l, r_0 = 0) + g_s(d_s, l, r_0 = d_a)}, \tag{A.43}$$

which is a long expression, even in the case $d_s = d_a = d$.

Comparing results

Now we have developed an analytical description of the source-aperture system in terms of aperture diameter d and source-aperture separation distance l for two different aperture shapes. In our experiment the typical aperture size will be around 100 μm ($\approx 10^{-4}$ m), governed by the mean free path of the atoms inside the Knudsen cell. The separation distance of the source and the aperture is limited by the capture velocity of the cooling and compression stage after the aperture. The typical separation distance is 1 cm (10^{-2} m). This means the ratio $d/l = \theta \approx 10^{-2} \ll 1$. In this limit the integrated density functions $G_s(d,l)$ and $G_c(d,l)$ become

$$G_s(d/l \ll 1) \approx 16\frac{d^4}{l^2} + O\left(\frac{d^6}{l^4}\right), \tag{A.44}$$

$$G_c(d/l \ll 1) \approx \pi^2\frac{d^4}{l^2} + O\left(\frac{d^6}{l^4}\right), \tag{A.45}$$

which can be generalized to

$$G(d/l \ll 1) \approx \chi S\theta^2, \tag{A.46}$$

where χ can be either 4 or π, depending on the chosen geometry of the apertures. Incidentally, this shows that the approximated flux given in Equation 2.18 is accurate within a factor χ/π which is either 1 or $4/\pi$ for circular and square apertures, respectively.

If we compare the two different shapes, we see that the general behaviour is very similar. Figures A.1 and A.2 show the fraction of flux, given by Equations A.22 and A.42, which goes through the aperture as function of aperture half-width or radius. Again we stress that the aperture and source sizes are equal in this model. By increasing the separation length by a factor of two (from $l = 0.010$ m to $l = 0.020$ m), the fraction of flux going through the aperture approximately decreases by an order of magnitude. This goes for both aperture shapes. Clearly the separation distance is a very sensitive parameter to control the total flux through the aperture.

The asymmetry parameter, given by Equations A.23 and A.43, does depend on the shape of the aperture, as can be seen in Figures A.3 and A.4. However, for all intents and purposes the asymmetry parameter is neglibly low and the flux density can be considered homogenous over the aperture surface.

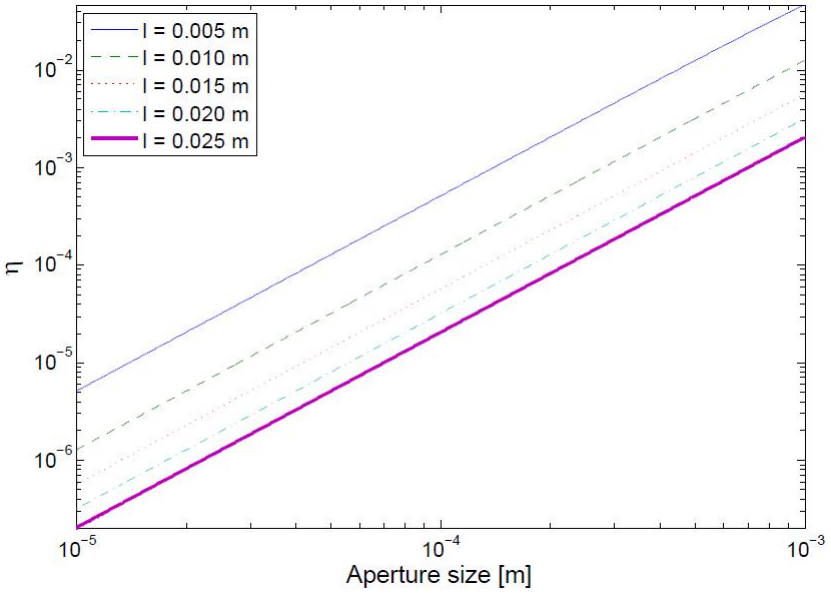

Figure A.1: *Fraction η of the total amount of flux emitted by the source which goes through the square aperture. The fraction as function of the source and aperture diameter has been plotted for different separation distances.*

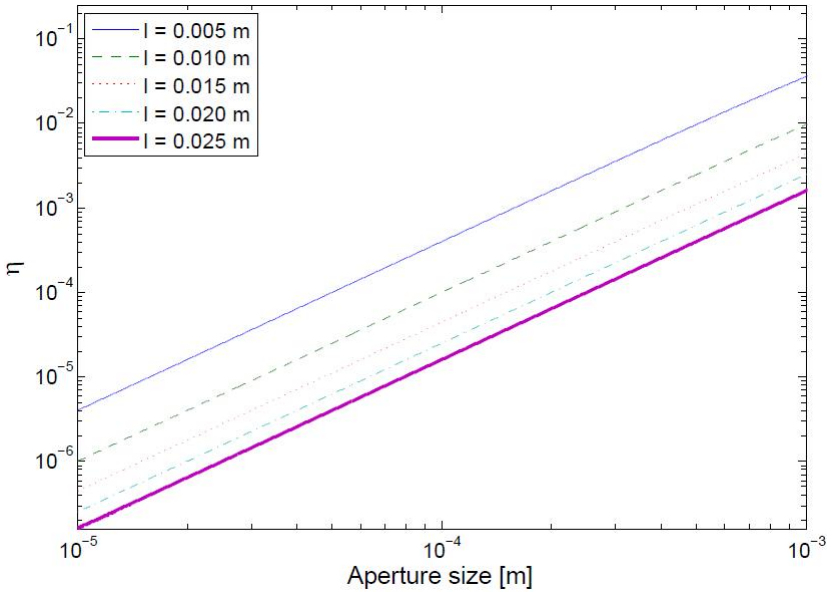

Figure A.2: *Fraction η of the total amount of flux emitted by the source which goes through the circular aperture. The fraction as function of the source and aperture diameter has been plotted for different separation distances.*

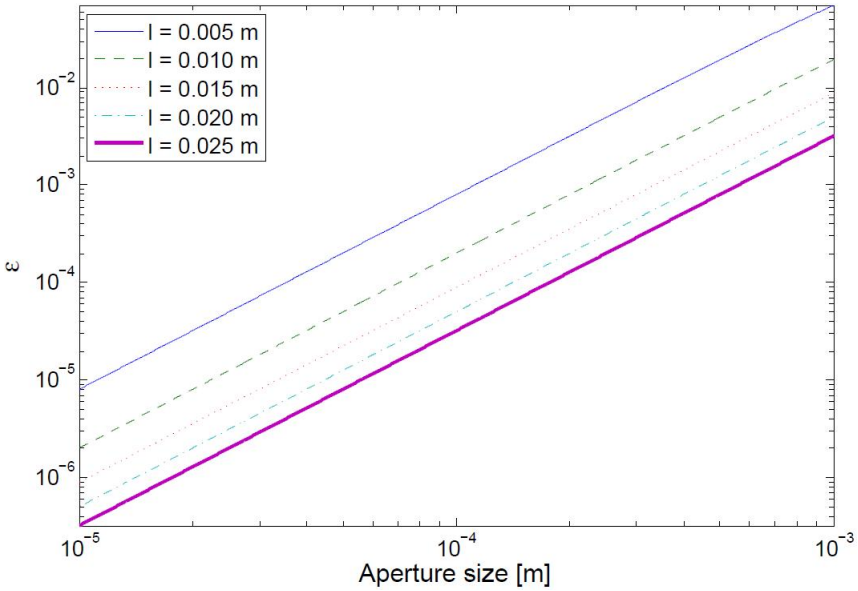

Figure A.3: *Asymmetry parameter ϵ of the density distribution at the square aperture. The parameter as function of the source and aperture diameter has been plotted for different separation distances.*

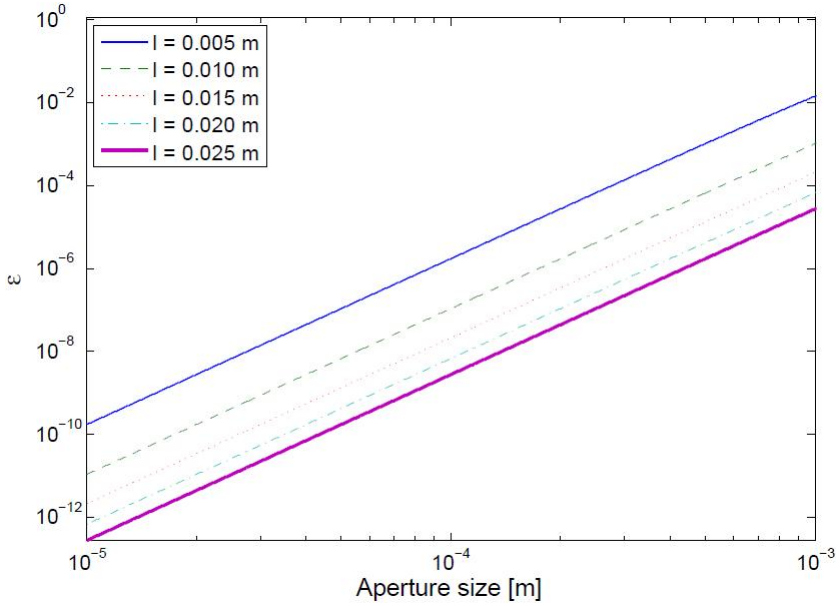

Figure A.4: *Asymmetry parameter ϵ of the density distribution at the circular aperture. The parameter as function of the source and aperture diameter has been plotted for different separation distances.*

Appendix B

Rubidium hyperfine structure

Rubidium has two isotopes: ^{85}Rb and ^{87}Rb. As shown in Table 2.1, both isotopes have different nuclear spin quantum numbers I and therefore also different hyperfine structure quantum numbers F. We discuss the origin of the hyperfine structure in Section 2.1.1. In this Appendix we present some additional level schemes and Zeeman shift calculations which are relevant to the work discussed in this report, but which are too long to be included in the main text.

The Zeeman shift for small magnetic fields (i.e. the energy shift due to the magnetic field is much smaller than the hyperfine splitting of the states) can be linearized to [16, 25, 26]

$$\Delta E = \mu_B g_F B M_F, \tag{B.1}$$

where μ_B is the Bohr magneton, B the applied magnetic field, M_F the quantum number of the hyperfine magnetic sub-state. The Landé factor g_F is defined as [16, 25, 26]

$$g_F = g_J \frac{F(F+1) + J(J+1) - I(I+1)}{2F(F+1)}, \tag{B.2}$$

$$g_J = \frac{J(J+1) + S(S+1) - L(L+1)}{2J(J+1)}. \tag{B.3}$$

As we know the quantum numbers of each state, we can calculate the appropriate Landé factors. The Landé factors of the hyperfine states relevant for the cooling transitions $5^2S_{1/2} \rightarrow 5^2P_{3/2}$ for both isotopes are given in Table B.1. In order to calculate the Zeeman shift of a transition, we have to take the difference in the Zeeman shift of both the ground and excited states into account

$$\Delta E = \mu_B B(M_{F,e} g_{F,e} - M_{F,g} g_{F,g}). \tag{B.4}$$

Further, when applying a magnetic field gradient ∇B transverse to the axis of propagation, we can linearize the magnetic field for small transverse positions x as $B(x) \approx x\nabla B$, which gives

$$\Delta E(x) = \mu_B(M_{F,e} g_{F,e} - M_{F,g} g_{F,g})\nabla B x. \tag{B.5}$$

The frequency shift due to the Zeeman shift can be calculated as $\Delta\nu = \Delta E/h$, where h is Planck's constant.

In Section 3.6.1 we discuss the different performances of both isotopes in the cooling and compression stage. The difference can be explained when considering the different transition strengths of the magnetic substate transitions of the isotopes combined with the Zeeman shift of each magnetic substate transition. Here we calculate the Zeeman shift of both isotopes weighted with the transitions strengths obtained from B.3 and B.4. We assume the light has σ^+ polarization, but the calculates are identical for σ^- polarized light. The calculations are shown in Tables B.2 and B.3 and give $8505/11340 \approx 75\%$ of the $M_F = 3 \rightarrow M_{F'} = 4$ transition for ^{85}Rb and $116.6/140 \approx 83\%$ of the $M_F = 2 \rightarrow M_{F'} = 3$ transition for ^{87}Rb. Averaged over all transition strenghts, ^{87}Rb experiences a larger Zeeman shift than ^{85}Rb. This explains why the former isotope is compressed more efficiently than the latter.

Table B.1: *Calculated Landé factors of the cooling transitions based on Equations B.2 and B.3.*

Property	^{85}Rb	^{87}Rb
F_{ground}	3	2
$F_{excited}$	4	3
$g_{F,ground}$	1/3	1/2
$g_{F,excited}$	1/2	2/3

Table B.2: *Calculated Zeeman shifts of ^{85}Rb $M_F \rightarrow M_{F'}$ transitions weighted by the relative transition strengths using σ^+ polarized light. The Landé factors are from Table B.1 and the relative transition strengths are from Figure B.3.*

$M_F \rightarrow M_{F'}$	$M_{F,e}g_{F,e} - M_{F,g}g_{F,g}$	Transition strength	Weighted shift (= shift × strenght)
$3 \rightarrow 4$	1	3780	3780
$2 \rightarrow 3$	5/6	2835	2362.5
$1 \rightarrow 2$	2/3	2025	1350
$0 \rightarrow 1$	1/2	1350	675
$-1 \rightarrow 0$	1/3	810	270
$-2 \rightarrow -1$	1/6	405	67.5
$-3 \rightarrow -2$	0	135	0
	Sum	11340	8505

Table B.3: *Calculated Zeeman shifts of ^{87}Rb $M_F \rightarrow M_{F'}$ transitions weighted by the relative transition strengths using σ^+ polarized light. The Landé factors are from Table B.1 and the relative transition strengths are from Figure B.4.*

$M_F \rightarrow M_{F'}$	$M_{F,e}g_{F,e} - M_{F,g}g_{F,g}$	Transition strength	Weighted shift (= shift × strenght)
$2 \rightarrow 3$	1	60	60
$1 \rightarrow 2$	5/6	40	33.3
$0 \rightarrow 1$	2/3	24	16
$-1 \rightarrow 0$	1/2	12	6
$-2 \rightarrow -1$	1/3	4	1.3
	Sum	140	116.6

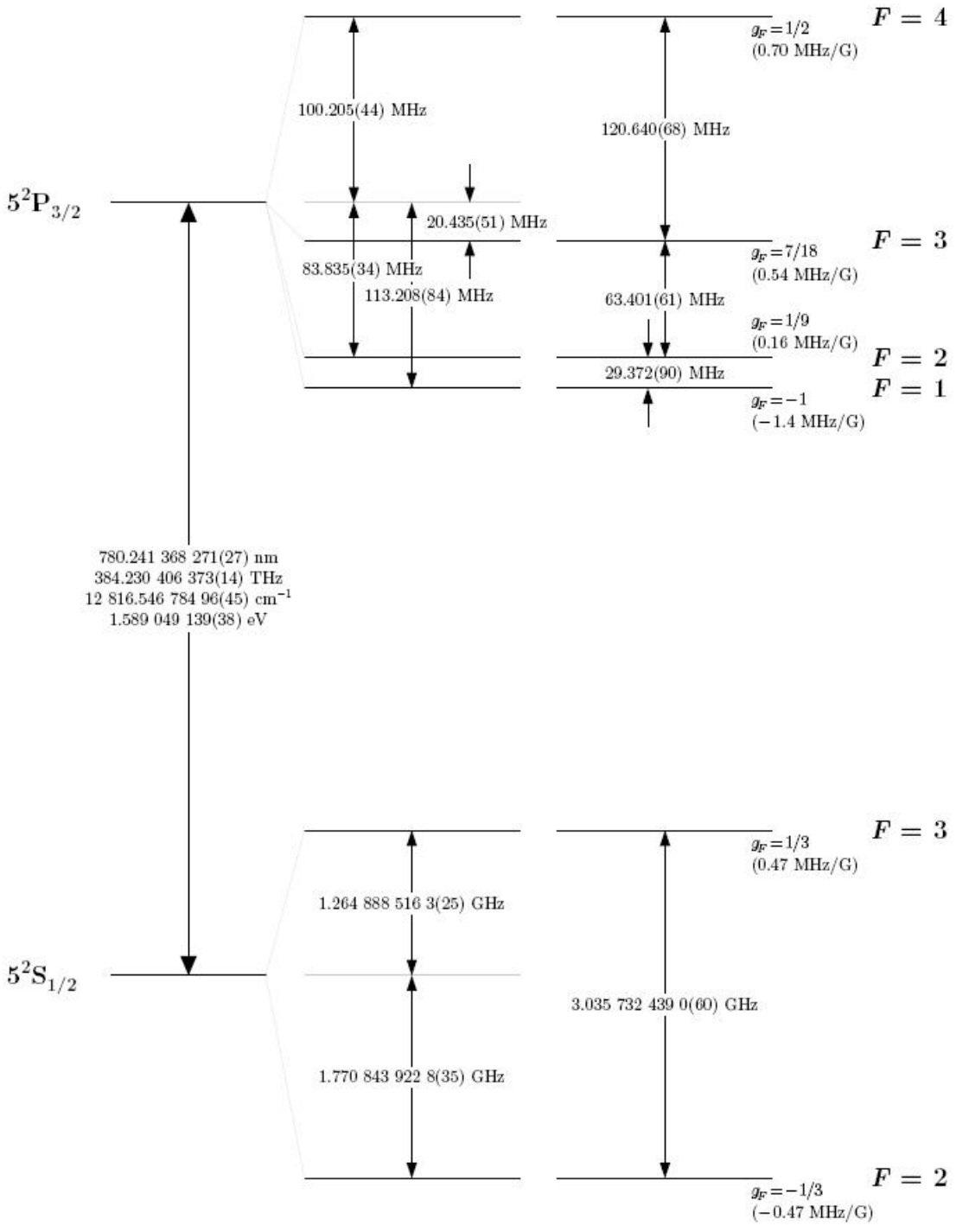

Figure B.1: *Hyperfine structure of ^{85}Rb including the transition frequencies and wavelengths. g_F is the Landé g-factor of the state and the gradients given in MHz/G are the small magnetic field Zeeman shifts of the energy levels [22, 25]. This Figure is taken from [22].*

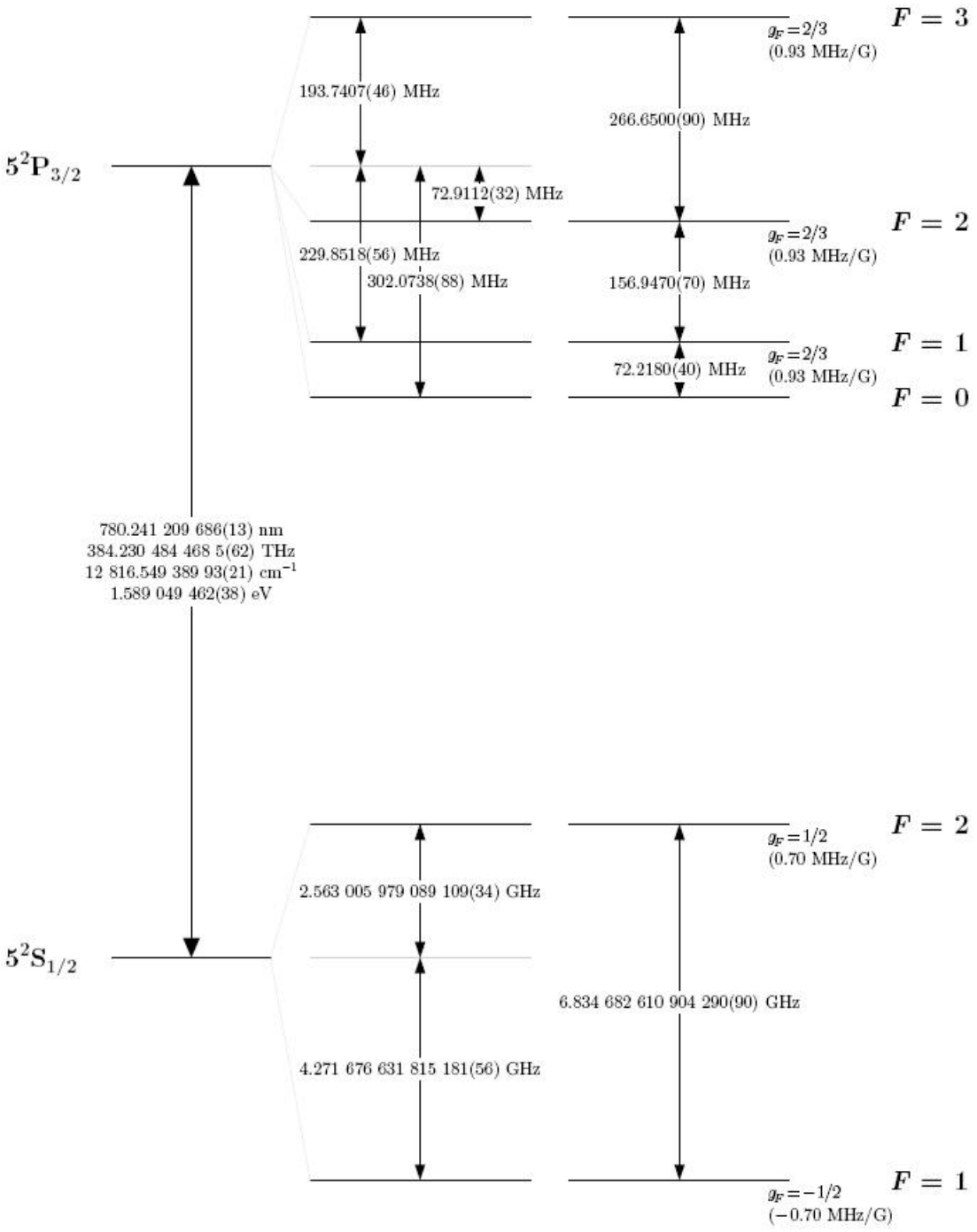

Figure B.2: *Hyperfine structure of ^{87}Rb including the transition frequencies and wavelengths. g_F is the Landé g-factor of the state and the gradients given in MHz/G are the small magnetic field Zeeman shifts of the energy levels [23, 25]. This Figure is taken from [23].*

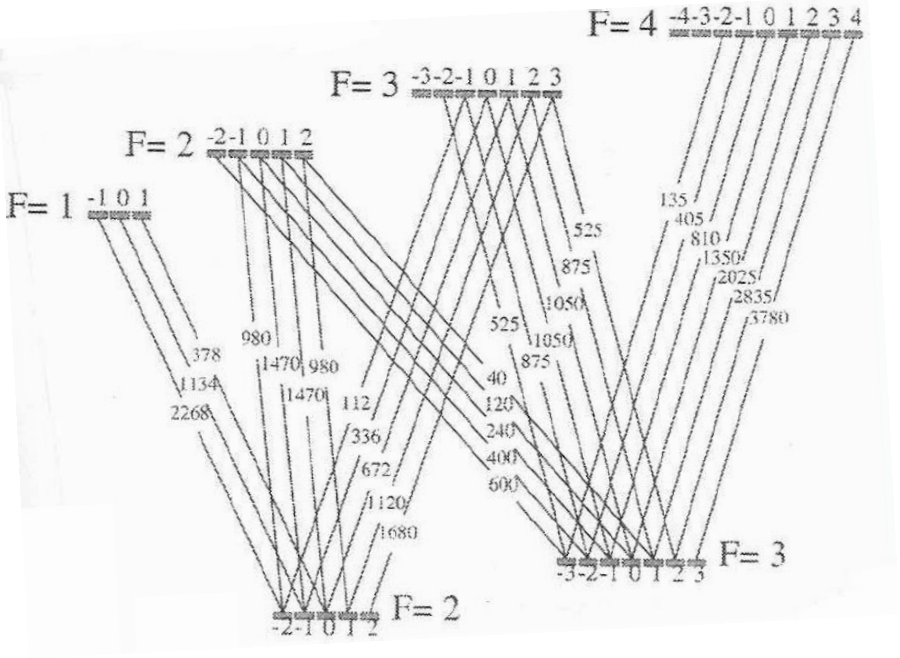

Figure B.3: *Relative transition strengths of the $5S_{1/2} \rightarrow 5P_{3/2}$ transitions of ^{85}Rb with σ^+ polarized light. The transition strengths are mirrored for the $M_F \rightarrow M_{F'}$ to the $M_{-F} \rightarrow M_{-F'}$ transitions in the case of σ^- polarized light. This Figure is taken from [16].*

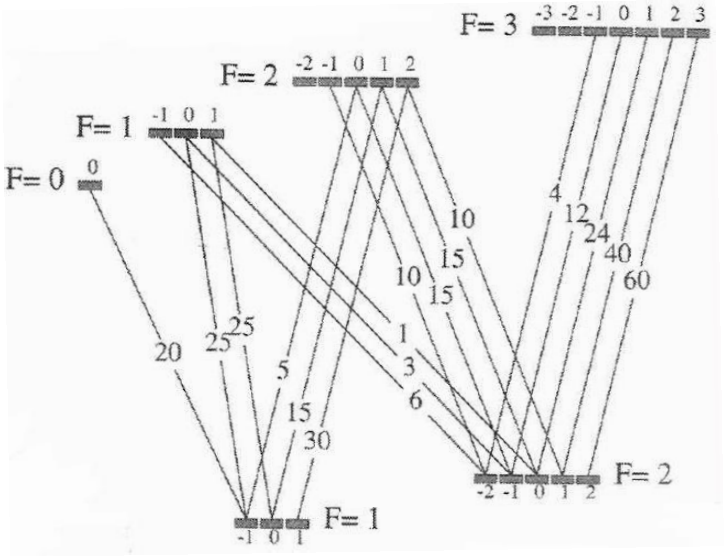

Figure B.4: *Relative transition strengths of the $5S_{1/2} \rightarrow 5P_{3/2}$ transitions of ^{87}Rb with σ^+ polarized light. The transition strengths are mirrored for the $M_F \rightarrow M_{F'}$ to the $M_{-F} \rightarrow M_{-F'}$ transitions in the case of σ^- polarized light. This Figure is taken from [16].*

Bibliography

[1] S. Borkar and A.A. Chien, "The future of microprocessors," *Comm. of the ACM*, vol. 54, pp. 67–77, (2011).

[2] Y. Xie, *Three dimensional system integration - IC stacking process and design*, ch. 9 - Microprocessor design using 3D integration technology. Springer, (2011).

[3] M.J. Bass and C.M. Christensen, "The future of the microprocessor business," *IEEE Spectrum*, vol. April, pp. 34–39, (2002).

[4] P. Kruit and H. Jansen, *Handbook of charged particle optics*, ch. Space charge and statistical Coulomb effects. CRC Press, New York, (1997).

[5] A.V. Krasheninnikov and F. Banhart, "Engineering of nanostructured carbon materials with electron or ion beams," *Nature Materials*, vol. 6, pp. 723–733, (2007).

[6] A.A. Tseng, "Recent developments in nanofabrication using focused ion beams," *Small*, vol. 10, pp. 924–939, (2005).

[7] S. Reyntjens and R. Puers, "A review of focused ion beam applications in microsystem technology," *J. Micromech. Microeng.*, vol. 11, pp. 287–300, (2001).

[8] O.J. Luiten, B.J. Claessens, S.B. van der Geer, M.P. Reijnders, G. Taban, and E.J.D. Vredenbregt, *Proceedings of the 46th workshop of the INFN ELOISATRON project - The physics and applications of high brightness electron beams*, ch. Ultracold electron sources. World Scientific Publishing Co. Pte. Ltd., (2007).

[9] P. Kruit, L.J. Vijgen, and J. Xinrong, "Coulomb interactions in microfocused electron and ion beams," *Nucl. Inst. Meth. Phys. Res. A*, vol. 363, pp. 220–224, (1995).

[10] S.B. van der Geer, M.P. Reijnders, M.J. de Loos, E.J.D. Vredenbregt, P.H.A. Mutsaers, and O.J. Luiten, "Simulated performance of an ultracold ion source," *J. Appl. Phys.*, vol. 102, pp. 094312 1–7, (2007).

[11] A.E. Bell, K. Rao, G.A. Schwind, and L.W. Swanson, "A low current liquid metal ion source," *J. Vac. Sci. Technol. B.*, vol. 6, pp. 927–930, (1988).

[12] C.W. Hagen, E. Fokkema, and P. Kruit, "Brightness measurements of a gallium liquid metal ion source," *J. Vac. Sci. Technol. B.*, vol. 26, pp. 2091–2096, (2008).

[13] V.N. Tondare, "Quest for high brightness, monochromatic noble gas ion sources," *J. Vac. Sci. Technol. A.*, vol. 23, pp. 1498–1508, (2005).

[14] B.W. Ward, J.A. Notte, and N.P. Economou, "Helium ion microscope: a new tool for nanoscale microscopy and metrology," *J. Vac. Sci. Technol. B.*, vol. 24, pp. 2871–2874, (2006).

[15] N.S. Smith, W.P. Skoczylas, S.M. Kellogg, D.E. Kinion, P.P. Tesch, O. Sutherland, A. Aanesland, and R.W. Boswell, "High brightness inductively coupled plasma source for high current focused ion beam applications," *J. Vac. Sci. Technol. B.*, vol. 24, pp. 2902–2906, (2006).

[16] H.J. Metcalf and P. v.d. Straten, *Laser cooling and trapping.* Springer, (1999).

[17] M.P. Reijnders, *Ion beams from laser-cooled gases.* PhD thesis, Eindhoven University of Technology, 2010.

[18] N. Debernardi, *UltraCold Ion Beam Source.* PhD thesis, Eindhoven University of Technology, 2012.

[19] P.H.A. Mutsaers, E.J.D. Vredenbregt, and O.J. Luiten, "Open Technologieprogramma - Ultracold FIB," (2011). Approved by STW in December 2011.

[20] B.G. Freinkman, A.V. Eletskii, and S.I. Zaitsev, "A proposed laser source of ions for nanotechnology," *Microelectronic Engineering*, vol. 73-74(0), pp. 139–143, (2004).

[21] *CRC Handbook of Chemistry and Physics.* CRC Press, 92 ed., (2011-2012).

[22] D.A. Steck, "Rubidium 85 D Line Data." available online at `http://steck.us/alkalidata` (revision 2.1.2., 12 August 2009).

[23] D.A. Steck, "Rubidium 87 D Line Data." available online at `http://steck.us/alkalidata` (revision 2.1.4., 23 December 2010).

[24] G. Scoles, ed., *Atomic and molecular beam methods*, vol. 1. Oxford University Press, 1 ed., (1988).

[25] C.J. Foot, *Atomic physics.* Oxford University Press, (2006).

[26] D. Griffiths, *Introduction to Quantum Mechanics.* Pearson Education International, 2nd ed., (2005).

[27] S.J. Blundell and K.M. Blundell, *Concepts in thermal physics.* Oxford University Press, 1 ed., (2006).

[28] M. Mantina, A.C. Chamberlin, R. Valero, R.J. Cramer, and D.G. Truhlar, "Consistent van der waals radii for the whole main group," *J. Phys. Chem. A*, vol. 113, pp. 5806–5812, (2009).

[29] E.J.D. Vredenbregt and K.A.H. van Leeuwen, "Laser cooling and trapping visualized," *Am. J. Phys.*, vol. 71, pp. 760–765, (2003).

[30] `http://www.pulsar.nl/gpt`.

[31] P.C. Tiemeijer, "Measurement of Coulomb interactions in an electron beam monochromator," *Ultramicroscopy*, vol. 78, pp. 53–62, (1999).

[32] P.F. Moulton, "Spectroscopic and laser characteristics Ti:Al_2O_3," *J. Opt. Soc. Am. B*, vol. 3, pp. 125–133, (1986).

[33] Coherent, Inc., *Operator's Manual - The Coherent 899-21 Titanium:Sapphire Ring Laser - Section I.*

[34] F.L. Pedrotti, L.M. Pedrotti, and L.S. Pedrotti, *Introduction to optics.* Pearson International Edition, 3rd ed., (2007).

[35] G. Kirchmair, *Frequency stabilization of a Titanium-Sapphire laser for precision spectroscopy on Calcium ions.* PhD thesis, Leopold Franzens University of Innsbruck, 2006.

[36] P.A. Schulz, "Single-frequency Ti:Al_2O_3 ring laser," *IEEE J. Quant. Elec.*, vol. 24, pp. 1039–1044, (1988).

[37] E. D. Black, "An introduction to Pound-Drever-Hall laser frequency stabilization," *Am. J. Phys.*, vol. 69, pp. 79–87, (2001).

[38] B. Kristiansson and B. Lennartson, "Robust and optimal tuning of PI and PID controllers," *IEE Proc.-Control Theory Appl.*, vol. 149, pp. 17–25, (2002).

[39] W. Demtröder, *Laser spectroscopy: basic concepts and instrumentation.* Springer, 3rd ed., (2003).

[40] Thorlabs, *EO-PM-NR-Cx Electro-Optic Phase Modulators Operating Manual.*

[41] D.J. McCarron, S.A. King, and S.L. Cornish, "Modulation transfer spectroscopy in atomic rubidium," *Meas. Sci. Technol.*, vol. 19, (2008). 105601.

[42] J.L. Hall, L. Hollberg, T. Baer, and H.G. Robinson, "Optical heterodyne saturation spectroscopy," *Appl. Phys. Lett.*, vol. 39, pp. 680–682, (1981).

[43] G.C. Bjorklund, "Frequency-modulation spectroscopy: a new method for measuring weak absorptions and dispersions," *Optics Lett.*, vol. 5, pp. 15–17, (1980).

[44] G.C. Bjorklund, M.D. Levenson, W. Lenth, and C. Ortiz, "Frequency modulation (FM) spectroscopy - Theory of lineshapes and signal-to-noise analysis," *Appl. Phys. B*, vol. 32, pp. 145–152, (1983).

[45] J.H. Shirley, "Modulation transfer processes in optical heterodyne saturation spectroscopy," *Optics Letters*, vol. 7, pp. 537–539, (1982).

[46] J.-L. Oudar and Y.R. Shen, "Nonlinear spectroscopy by multiresonant four-wave mixing," *Phys. Rev. A*, vol. 22, pp. 1141–1158, (1980).

[47] R.K. Raj, D. Bloch, J.J. Snyder, G. Camy, and M. Ducloy, "High-frequency optically heterodyned saturation spectroscopy via resonant degenerate four-wave mixing," *Phys. Rev. Lett.*, vol. 44, pp. 1251–1254, (1980).

[48] D. Bloch, R.K. Raj, K.S. Peng, and M. Ducloy, "Dispersive character and directional anisotropy of saturated susceptibilities in resonant backward four-wave mixing," *Phys. Rev. Lett.*, vol. 49, pp. 719–722, (1982).

[49] N. Storey, *Electronics - a systems approach*. Pearson Prentice Hall, 3rd ed., (2006).

[50] *EO-PM Series Phase Modulator Test Data*. Serial number PN1133903.

[51] I. Koole, "Capacitance per unit length of coaxial cable." private communication.

[52] `http://www.cadence.com/products/orcad/pspice_simulation/pages/default.aspx`.

[53] D. Griffiths, *Introduction to Electrodynamics*. Pearson Education International, 3rd ed., (2008).

[54] D.W. Allan, "Statistics of atomic frequency standards," *Proc. IEEE*, vol. 54, pp. 221–230, (1966).

[55] J.A. Barnes, A.R. Chi, L.S. Cutler, D.J. Healey, D.B. Leeson, T.E. McGunigal, J.A. Mullen jr., W. L. Smith, R.L. Snydor, R.F.C. Vessot, and G.M.R. Winkler, "Characterization of frequency stability," *IEEE Trans. Instr. Meas.*, vol. Im-20, pp. 105–120, (1971).

[56] A.L. Schawlow and C.H. Townes, "Infrared and optical masers," *Physical Review*, vol. 112, pp. 1940–1949, (1958).

[57] C.H. Henry, "Theory of the linewidth of semiconductor lasers," *IEEE J. Quantum Elec.*, vol. QE-18, pp. 259–264, (1982).

[58] Toptica Photonics, *DLX 110 High Power Tunable Single-Mode Diode Laser Manual*.